SENSITIVITY OF SURFACE OZONE SIMULATION IN HOUSTON, TX: OZONE EXCEEDANCE FORMATION, FINE GRID RESOLUTION, AND FUTURE MOBILE EMISSIONS PROJECTION

A Dissertation Presented to

the Faculty of the Department of Earth and Atmospheric Sciences

University of Houston

In Partial Fulfillment

of the Requirements for the Degree

Doctor of Philosophy

By

Shuai Pan

August 2017

SENSITIVITY OF SURFACE OZONE SIMULATION IN HOUSTON, TX: OZONE EXCEEDANCE FORMATION, FINE GRID RESOLUTION, AND FUTURE MOBILE EMISSIONS PROJECTION

_____

Shuai Pan

APPROVED:

_____

Dr. Yunsoo Choi, Advisor

_____

Dr. Bernhard Rappenglück

_____

Dr. Xun Jiang

_____

Dr. Hyun Cheol Kim
NOAA Air Resources Laboratory

_____

Dean, College of Natural Sciences and Mathematics

ACKNOWLEDGEMENTS

I express my deepest gratitude to my advisor, Dr. Yunsoo Choi, for his generous guidance and support. I thank him for sharing his experience, providing valuable resources, and giving me enough freedom to explore my own ideas. I would like to thank my committee members: Dr. Bernhard Rappenglück for his constructive suggestions, Dr. Xun Jiang for her thoughtful guidance, and Dr. Hyun Cheol Kim for his incisive scientific and technical advice.

I would like to thank Dr. Beata Czader for helping me to learn the ropes of the SMOKE/CMAQ models, Dr. Xiangshang Li for teaching me the basics of IDL plotting, and Dr. Wonbae Jeon for very helpful scientific comments. Special thanks to Dr. Anirban Roy for thorough scientific inputs on each of my research topics and teaching me technical writing. Additionally, I would like to thank Dr. Lijun Diao, Joey Rodriguez, Amir Souri, Alex Kotsakis, Ebrahim Eslami, and Jia Jung for working together. I express my thanks to the other EAS faculty members and graduate students for discussions on different interesting research topics.

I would also like to thank Dr. BH Baek for his helpful instructions on the SMOKE model setup. I acknowledge the help receiving through the CMAS Center Help Desk. I would like to thank David Westenbarger for detailed proofreading of my ozone exceedance formation study. I acknowledge the free use of the measurement data from the Texas Commission on Environmental Quality (TCEQ), NASA, and NOAA, and all the modeling platforms. Sincere thanks to the scientists and engineers involved in this initiative for their selfless efforts to make these data available. I appreciate the anonymous reviewers who helped improve the quality of the research papers greatly.

I would like to appreciate the financial support from UH EAS Teaching Assistantship, the TCEQ's Air Quality Research Program, and Healthy Port Communities Coalition.

I would like to thank my students from TA Labs in the past four years, for their patience, smartness, and hard work.

Last, but not the least, I would like to express my heartfelt gratitude to my parents for their constant encouragement and support in my attainment of this goal. Special thanks go to my girlfriend, Tiantian, for her understanding and love.

SENSITIVITY OF SURFACE OZONE SIMULATION IN HOUSTON, TX: OZONE EXCEEDANCE FORMATION, FINE GRID RESOLUTION, AND FUTURE MOBILE EMISSIONS PROJECTION

An Abstract of a Dissertation

Presented to

the Faculty of the Department of Earth and Atmospheric Sciences

University of Houston

In Partial Fulfillment

of the Requirements for the Degree

Doctor of Philosophy

By

Shuai Pan

August 2017

ABSTRACT

The Houston metropolitan area is classified as a nonattainment area for ozone (O_3) by the United States Environmental Protection Agency. In order to obtain a better understanding of the O_3 budget in Houston, a WRF-SMOKE-CMAQ air quality modeling system was used to investigate the sensitivity of surface O_3 simulation due to precursor emissions, meteorology, and grid resolution. The simulation period was September 2013, coincident with NASA's DISCOVER-AQ campaign. A WRF run initialized with high-resolution NOAA GOES satellite sea surface temperature data reduced the model wind speed and slowed the dilution rate. However, it still failed to reproduce the exceptionally high surface O_3 on 25th September 2013, possibly attributed to episodic flare emissions, dry sunny postfrontal stagnated conditions, and land-bay/sea breeze transitions. Adjusting wind fields to represent the morning weak westerly and afternoon converging zone significantly improved the predictions of magnitude, timing, and location of the O_3 hotspots. We compared two simulations with meteorology and emissions prepared for grid spacing of 1 km and 4 km, respectively. The peak NO_x emissions at an industrial and urban site differed by a factor of 20 for the 1 km and 8 for the 4 km grid, but simulated NO_x concentrations changed only by a factor of 1.2 in both cases. Hence, due to the interplay of the atmospheric processes, we cannot expect a similar level of reduction of gas-phase air pollutants as the reduction of emissions. Future projections of trucking emissions and evaluation of various scenarios with varying levels of emission control suggested that to maintain the current air quality conditions, applying highest emission reductions to at least 50% of the freight traffic is needed.

Table of Contents

Chapter 1. Introduction

Air pollution has significant health, ecological, and economic consequences. Elevated concentrations of criteria pollutants ground-level ozone (O_3) and fine particulate matter ($PM_{2.5}$) cause respiratory and cardiovascular problems and lead to tens of thousands of premature deaths each year, with costs in the US of more than $100 billion (CATF, 2010). The Houston metropolitan area is historically known for air quality problems and is classified as a nonattainment area for O_3 (U.S. EPA's Green Book, 2016). Motor vehicle exhaust, power plant and industrial effluents, gasoline vapors, and chemical solvents, as well as natural sources, produce emissions of nitrogen oxides (NO_x = NO + NO_2) and volatile organic compounds (VOCs) that form O_3 in the presence of sunlight. The Houston metropolitan area is characterized by high population density, and it is the fourth-largest metropolitan area in the United States (US Census Bureau 2012). Presence of significant anthropogenic emission sources such as large clusters of petrochemical and chemical manufacturing facilities, motor vehicles and marine vessels (Daum et al., 2003; Czader et al., 2008; Olaguer et al., 2009), and biogenic sources such as vegetation (Byun et al., 2005) make the pollutant mix in this area unique in the region. Therefore it is important to understand and quantify the O_3 precursors' emissions in this region so as to develop appropriate control policies for better air quality and correspondingly attainment status and human health.

Urban and regional air quality models can predict concentrations of pollutants where measurements are not available, describe the impact of chemical and physical processes on concentrations of simulated compounds, and predict probable response to

emission control strategies. These models are widely used for policy purposes due to these benefits. However, it necessitates accurate predictions of in-situ data by these models to make sure they capture the physics properly. There are many previous studies focusing on air quality research by improving model performance using different techniques. Choi et al. (2012) and Choi (2014) applied Global Ozone Monitoring Experiments (GOME)-2 NO_2 retrievals to constrain CMAQ-simulated NO_x emissions over the U.S. for August 2009 and found that reduction in NO_x emissions led to large reduced concentrations of simulated NO_x. However, the reduced emissions exacerbated pre-existing high surface O_3 over-predictions over the Houston area, while reducing daytime O_3 concentrations over the outflow regions. These findings suggested that high O_3 biases in the Houston area cannot be explained by simulated high NO_x bias and urban and outflow regions could be treated as NO_x-saturated and NO_x-sensitive regimes respectively. Czader et al. (2015) adjusted the National Emission Inventory of 2008 by reducing NO_x emissions from mobile sources and point sources based on the long-term trends of anthropogenic NO_x emission reported by U.S. EPA. The authors used these modified emissions simulate HONO concentrations for an urban site in Houston for September 2013, and found that reducing NO_x emissions improved NO_x and HONO predictions, but the impact on O_3 was marginal.

Volatile Organic Compounds can be a significant contributor to the ground-level O_3 in urban areas, where O_3 concentrations are typically VOC-sensitive (e.g., Choi et al. 2012; Choi 2014). Examples of VOCs include aromatics such as toluene and unsaturated hydrocarbons such as ethylene which have high O_3 forming potential (Carter, 1994). Additionally, VOCs in urban regions often comprise of several air toxic species such as

benzene and toluene which have a high potential to cause cancer. Ryerson et al. (2003) mentioned that the emissions of light molecular weight alkenes such as ethylene, propylene, 1,3-butadiene, and butenes are important to explain rapid O_3 formation in the Houston area through the Texas Air Quality Study (TexAQS) 2000 aircraft campaign measurements. Vizuete et al. (2008) simulated a series of high industrial point source emissions for the VOC species, n-pentane, ethylene, propene and o-xylene by using the CAMx model and concluded that O_3 concentrations showed the highest sensitivity to o-xylene. VOC species concentrations typically show significant temporal and spatial variations; hence the uncertainty of VOC emissions is one of the major contributions to simulated O_3 bias in chemical transport models. Byun et al. (2007) showed ethylene concentrations exhibited significant variability over high O_3 episode days as well as pronounced diurnal cycles. Nam et al. (2006) simulated a series of short-term (1-2-hour) release of Highly Reactive Volatile Organic Compounds (HRVOCs) from industrial point sources and indicated that 11 out of 793 emission events produced more than 10 ppb of additional O_3 and that 4 out of 793 events produced more than 70 ppb of additional O_3 in the industrial area. Model simulations by Webster et al. (2007) using CAMx indicated that the changes in the industrial point source emissions had the potential to cause changes of 10-52 ppb (13-316%) or more in simulated O_3 concentrations. Couzo et al. (2012) and Couzo et al.(2013) analyzed the long term (2000-2009 and 2000-2011, respectively) ground-level O_3 measurements and found that in Houston, most non-typical ozone changes were measured at monitors near the ship channel, especially when monitors were downwind of petrochemical facilities.

In addition to significant emissions, nonattainment episodes in Houston are also known to be caused by complex meteorological conditions such as land-sea/bay breezes (Banta et al., 2005; Darby, 2005), post-frontal conditions (Rappenglück et al., 2008; Ngan and Byun, 2011), boundary layer depth (Banta et al., 2011; Haman et al., 2014), and convective venting (Langford et al., 2010). The interplay among emissions, meteorology, and chemistry have been addressed in comprehensive measurement campaigns including the Texas Air Quality Study 2000 (TexAQS-2000) (Ryerson et al., 2003) in the summer of 2000, the Second Texas Air Quality Study (TexAQS-II or TexAQS-2006) (Parrish et al., 2009) in the summer of 2006, and more recently the National Aeronautics and Space Administration's (NASA) Deriving Information on Surface Conditions from COlumn and VERtically Resolved Observations Relevant to Air Quality (DISCOVER-AQ) Texas campaign (NASA, 2013; Crawford et al., 2014) in September of 2013. Cluster analysis of hourly averaged wind measurements of TexAQS-2000 data shows wind transition from offshore to onshore flow, with at least 1 hour of stagnant wind in between. These routinely preceded hourly averaged O_3 measurements in excess of 120 ppb. On non-transition days high O_3 often occurred after a wind direction shift of greater than 45 degrees (Darby 2005). Dry and sunny post-frontal days with weak northerly or easterly winds are often associated with O_3 exceedances in the Houston-Galveston-Brazoria (HGB) area during TexAQS-2006 (Ngan and Byun 2011). Wind pattern is one of the major drivers behind pollutant transport and distribution, influencing chemistry and O_3 exceedance in the greater Houston area.

The highest maximum daily surface eight-hour O_3 concentration (MDA8) of 124 ppb and the highest 1-hour value of 151 ppb during the DISCOVER-AQ Texas campaign in 2013 were observed on 25th September. Under-estimation of this high O_3 episode by air quality models has been reported consistently by several studies (Loughner et al., 2015; Nopmongcol et al., 2015; Pan et al., 2015; Li et al., 2016). Loughner et al. (2015) showed that sea and bay breezes occurred during the afternoon (15 CST) of 25th September and suggested that sea and bay breeze circulations caused pollutants to recirculate leading to the enhanced O_3 formation. The authors also examined daytime aircraft measurements and indicated that elevated formaldehyde (HCHO), carbon monoxide (CO) and nitric oxide (NO) concentrations in the Ship Channel industrial region, possibly from flaring events from petrochemical facilities, resulted in model under-estimation of surface O_3. A modeling study by Li et al. (2016) suggested that the high O_3 episode was a post-front O_3 event in Houston; indicating that small-scale morning wind shifts near the Ship Channel combined with higher early morning aloft O_3 likely contributed to the day's O_3 exceedance. To date, the cause of the high O_3 and the source of model under-estimation have not been thoroughly understood.

Several studies have simulated ground-level O_3 in the area and attributed model-measurement bias to uncertainties in precursor emissions (Choi, 2014; Czader et al., 2015; Pan et al., 2015; Diao et al., 2016a; Souri et al., 2016) and meteorological fields (Ngan et al., 2012; Li et al., 2016; Diao et al., 2016b; Pan et al., 2017a). However, the bias still cannot be fully resolved after improving these parameters. Grid resolution is one of the factors that influence the formation and loss of ground-level O_3 in chemical transport

models, as indicated by previous studies (Jang et al., 1995a, 1995b; Cohan et al., 2006; Arunachalam et al., 2006; Valari and Menut, 2008). Jang et al. (1995a) simulated O_3 formation at horizontal resolutions of 80, 40, and 20 km using the High Resolution Regional Acid Deposition Model (HR-RADM). Their results showed that the 80 km grid model tended to under-predict O_3 maxima in regions downwind of city areas and over-predict O_3 minima over major source regions because the spatial distribution of emissions was not accurately characterized. They also suggested that an averaged treatment of sub-grid processes in a grid with 80 km resolution may not accurately represent the important production, loss and transport processes for O_3 and NO_x. Cohan et al. (2006) examined the sensitivity of ground-level O_3 to NO_x emissions with different grid resolutions in Georgia using the Community Multiscale Air Quality (CMAQ) model. They found that a 12 km resolution is sufficient to predict O_3 production efficiency, but a higher resolution of 4 km is required to identify localized pockets of NO_x inhibition. Arunachalam et al. (2006) utilized the MM5-SMOKE-MAQSIP modeling system to evaluate the influence of grid resolution on O_3 concentrations using grids of 36, 12 and 4 km. Their study of four 8-h O_3 episodes in the summer of 1995, 1996 and 1997 in North Carolina showed no significant differences between the 4 km and 12 km results, with larger differences of 1-3 ppb between the 4 and 36 km grids. They recommended that the 1-3 ppb variability due to grid resolution to be incorporated into policy-relevant decision-making to help nonattainment regions achieve attainment status.

Since emissions are the starting point for an air quality model, calculating high-resolution emissions is critical to obtain accurate model predictions of observational data.

A study by Valari and Menut (2008) over the Paris area indicated that the CHIMERE chemical transport model is more sensitive to changes in the spatial resolution of emissions than in meteorological inputs. Emissions exhibit very strong spatial gradients as the landscape changes from a highly urbanized city to rural areas over a very short distance (20-30 km), while meteorological fields are relatively homogeneous. Roy et al. (2011) used the PMCAMx model to simulate concentrations of norhopane, a $PM_{2.5}$ tracer for motor vehicles using a 36 km grid. They performed model-measurement comparisons over several urban and rural sites in the eastern US and suggested grid cell resolution to be one of the causes for model-measurement error since the coarse 36 km grid was unable to capture sub-grid features such as highways. Fountoukis et al. (2013) performed two simulation cases each over the U.S. and Europe to study the effect of grid cell size on model predictions. The U.S. study was conducted over the northeastern region with grid resolutions of 36 and 12 km, where the 12 km resolution emissions were simply interpolated from 36 km. The study over Western Europe involved grid resolutions of 36 and 4 km, where the 4 km case used finer resolution emissions. They reported that the use of 4 km emissions in Paris produced much larger spatial concentration gradients in the domain as compared to interpolated emissions. They also suggested that use of high-resolution simulations combined with high-resolution emissions improved model predictions. For example, the fractional bias for organic aerosol predictions changed from 80% to 60% for the city center of Paris. The authors concluded that merely interpolating emissions from a coarse resolution to a finer resolution could potentially introduce errors especially in heavily polluted regions, and the benefits of using high resolution would not be fully achieved. While there have been several studies using resolutions of 4 km over the

U.S. and Europe, none of these have focused on using a finer 1 km resolution. A fine resolution of 1 km will help more clearly delineate the emissions features in an urban region and also help quantify urban-suburban transport and identify the causes of pollution in heavily populated areas.

Emissions from gasoline and diesel vehicular traffic are the major sources of NO_x, VOC, and important components of particulate matter such as organic and elemental carbon in urban areas. Estimating the trends of transportation emissions in the future and its impact on air quality can provide useful information for requisite control policy. Li et al. (2016) reported that fully electrifying all light-duty vehicles would reduce the mean peak-time surface O_3 concentrations by up to 7 ppb across Taiwan except the center of metropolitan Taipei (an increase of <2 ppb). Their findings also indicated it would also reduce the annual number of days of O_3 pollution episodes by 40% and $PM_{2.5}$ pollution episodes by 6-10%. Nopmongcol et al. (2017) assumed that 17% of light duty and 8% of heavy duty vehicle miles traveled and 17-79% of various off-road equipment types are considered for electrification in the U. S. in the year 2030. They reported that the electrification would reduce less than 1 ppb for O_3 and 0.5 μg m^{-3} for $PM_{2.5}$. However, no study has been conducted so far for the Houston Metropolitan Area. As indicated by the 2013 Houston-Galveston Area Council (H-GAC) Regional Goods Movement Plan, the population of the Houston Area is projected to grow by 50% in 2040, which could potentially result in increased trucking and other freight activity to meet the needs of the growing population. It is, therefore, imperative to carry out an impact analysis study going

into the future by evaluating the air quality impacts of the increased transportation activity, the effects of control technologies and strategies.

In order to obtain a better understanding of regional O_3 condition in Houston, a WRF-SMOKE-CMAQ air quality modeling system was used to investigate the sensitivity of surface O_3 concentrations due to precursor emissions, meteorology, and grid spatial resolution during the September 2013 episode. In this space, Chapter 2 describes the model configurations used in this study. Chapter 3 examines the impact of high-resolution sea surface temperature, emission spikes and wind on simulated surface O_3 during an exceptionally high O_3 episode on 25th September 2013. Chapter 4 discusses the impact of horizontal grid resolution on simulated NO_x and O_3 by comparing two simulations with meteorology and emissions with a grid spacing of 1 km and 4 km. Chapter 5 evaluates the air quality impacts of increased freight traffic in the Great Houston Area in a future year, taking into account varying levels of emissions controls. Chapter 6 concludes the findings in this study.

Chapter 2. Data and Model

2.1. Model set-up

This study used a WRF-SMOKE-CMAQ modeling system which included meteorological, emissions, and chemical transport modeling. The United States Environmental Protection Agency (USEPA)'s Community Multi-scale Air Quality (CMAQ) model (Byun and Schere, 2006) was employed for chemical transport modeling. Here, chemistry was modeled using the Carbon Bond 5 mechanism (CB05) (Yarwood et al., 2005). Meteorology was simulated using the Weather Research and Forecasting (WRF) model (Skamarock and Klemp, 2008). The National Centers for Environmental Prediction (NCEP) North American Regional Reanalysis (NARR) data (Mesinger et al., 2004) were used as input for WRF. The model output was converted to CMAQ-ready format by the Meteorology-Chemistry Interface Processor (MCIP), version 4.1 (Byun and Schere, 2006). The details of WRF physics options and CMAQ configurations are listed in Tables 2.1 and 2.2. The same configurations have been used in previous air quality modeling studies (Pan et al., 2015, 2017a, 2017b; Li et al., 2016; Diao et al., 2016a, 2016b).

Table 2.1. The WRF physics options.

WRF version	v3.5 in Chapter 3.3, and v3.7 in Chapter 3.4, 3.5, and 3.6
Microphysics	Lin et al. scheme
Long-wave radiation	RRTMg
Short-wave radiation	New Goddard scheme
Surface layer option	Monin-Obukhov with Carlson-Boland viscous sublayer scheme
Land-surface option	NOAH Land-Surface Model
Urban physics	None
Boundary layer	YSU
Cumulus parameterization	Kain-Fritsch (new Eta)
FDDA	Grid analysis nudging

Table 2.2. Major CMAQ options.

CMAQ version	v5.0.1 in Chapter 3.3, and v5.0.2 in Chapter 3.4, 3.5, and 3.6
Chemical mechanism	cb05tucl_ae6_aq: CB05 gas-phase mechanism with active chlorine chemistry, updated toluene mechanism, sixth-generation CMAQ aerosol mechanism with sea salt, aqueous/cloud chemistry
Horizontal advection	YAMO
Vertical advection	WRF omega formula
Horizontal diffusion	Multiscale
Vertical diffusion	Asymmetric Convective Model (ACM) version 2
Deposition	M3dry
Chemistry solver	SMVGEAR
Aerosol	AERO5 in Chapter 3.3 and 3.4; AERO6 in Chapter 3.5 and 3.6
Lightning NO_x emission	Included inline
Cloud option	ACM cloud processor for aerosol module

Emission inputs were prepared using the Sparse Matrix Operator Kernel Emissions (SMOKE) model (Houyoux et al., 2000) using the U.S. EPA's National Emission Inventory (NEI). The SMOKE model performs spatial and temporal allocation, chemical speciation, plume rise of elevated sources and other processes to create gridded hourly CMAQ model-ready input emission files. Anthropogenic emissions include point, area, and mobile sources. Point sources include Electricity Generating Units (EGUs, both peaking and non-peaking units), oil and gas production processes, category 3 marine vessels, and non-EGU stationary sources. Area sources include agricultural activities, fugitive dust, locomotives, category 1 and 2 commercial marine vessels, oil and gas production processes, non-road vehicles, residential wood combustion, and remaining non-point sources. Onroad mobile source emission factors from cars, trucks, and motorcycles were estimated by the Motor Vehicle Emission Simulator (MOVES). Biogenic emissions were estimated using the Biogenic Emission Inventory System, version 3.14 (BEIS3).

The standard 4 km HGB simulation domains covered southeast Texas (the smaller domains in Fig. 2.1). The CMAQ domain had 84 grid cells in the east-west direction, 66 in the north-south direction, and 27 vertical layers from the surface to 100 hPa. Initial and boundary conditions were obtained from the Air Quality Forecasting system at the University of Houston (AQF-UH) (http://spock.geosc.uh.edu/), employing a larger domain with 12 km grid covering the coterminous United States, southern Canada, and northern Mexico (CONUS, the larger domains in Fig. 2.1). The detailed modeling domain information is displayed in Table 2.3 while the vertical layer structure is described in Table 2.4.

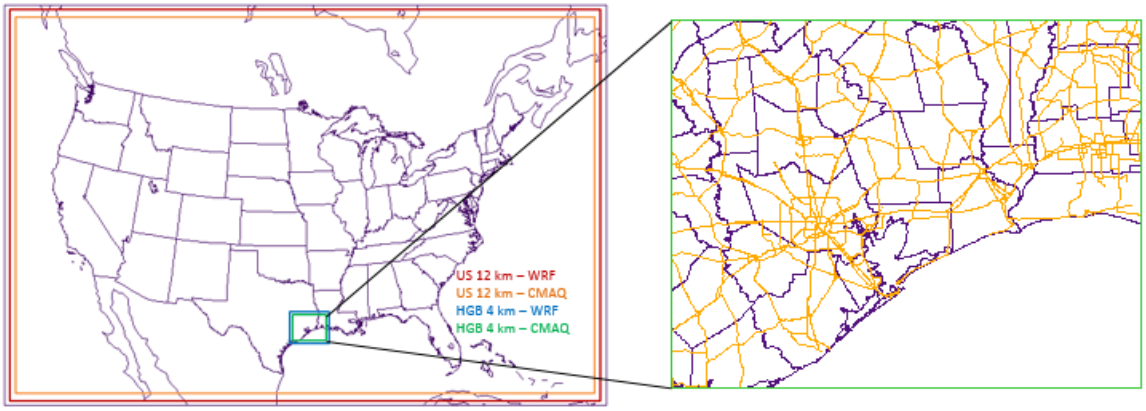

Fig. 2.1. Horizontal domains of WRF and CMAQ at different grid resolution; the HGB 4 km are used in this study while the US 12 km is used to provide boundary conditions. For the zoomed-in plot on the right, roadways are represented in orange and county boundaries in purple.

Table 2.3. The CMAQ domain information for HGB and CONUS domains.

Domain	Horizontal resolution	East-west direction	North-south direction	Vertical layers
HGB	4 km	84 grids	66 grids	27 layers
CONUS	12 km	459 grids	299 grids	27 layers

Table 2.4. The structure of vertical model layers. Height values in the 3rd and 4th columns are averaged above ground level (AGL) heights in each layer.

Layer	Eta-level	Mid-layer height [m]	Full-layer height [m]	Layer thickness [m]
1 (surface)	0.996	16	32	32
2	0.990	57	82	50
3	0.980	124	165	83
4	0.970	206	248	83
5	0.960	290	332	84
6	0.950	374	417	85
7	0.940	459	502	85
8	0.930	544	587	85
9	0.920	630	673	86
10	0.910	716	760	87
11	0.895	826	891	131
12	0.880	958	1024	133
13	0.865	1091	1158	134
14	0.850	1226	1294	136
15	0.825	1409	1524	230
16	0.800	1641	1758	234
17	0.775	1878	1997	239
18	0.750	2119	2240	243
19	0.720	2391	2540	300
20	0.660	2846	3164	624
21	0.570	3651	4178	1014
22	0.475	4757	5387	1209
23	0.370	6116	6927	1540
24	0.250	7904	9042	2115
25	0.145	10143	11394	2352
26	0.045	12807	14484	3090
27	0.000	15680	16493	2009

2.2. Observational data

The Texas Commission on Environmental Quality (TCEQ)'s Continuous Ambient Monitoring Stations (CAMS) network (http://www.tceq.texas.gov/cgi-bin/compliance/monops/daily_average.pl) provides in-situ ground-level measurements for meteorological parameters and several chemical species such as NO_x, O_3 and a large suite of Volatile Organic Compounds. These data were used to evaluate model performance.

The NASA's P-3B aircraft collected O_3 HCHO, NO_y, and isoprene measurements during the NASA's Deriving Information on Surface Conditions from Column and Vertically Resolved Observations Relevant to Air Quality (DISCOVER-AQ) campaign in Houston; these were used to evaluate simulated pollutants concentrations aloft.

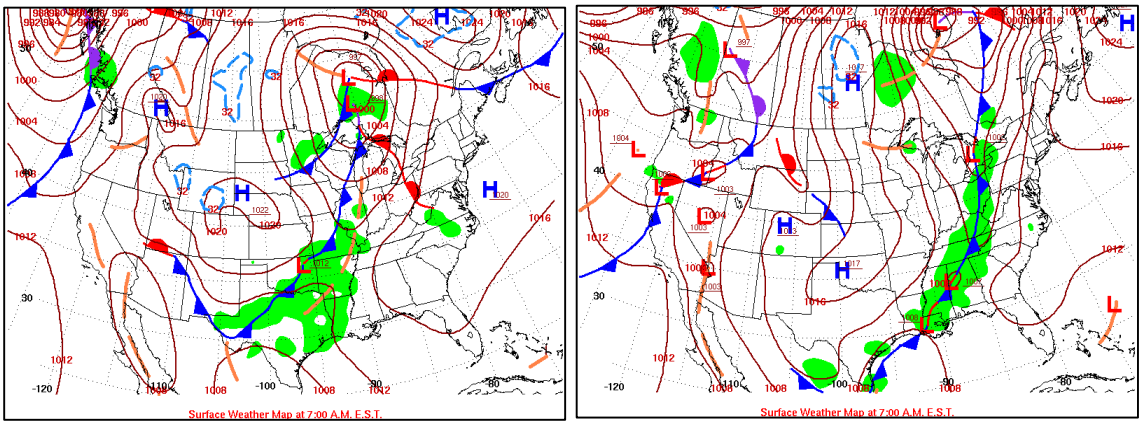

Fig. 2.2. Surface weather map at 7:00 EST on 20th September 2013 (left) and 21st September 2013 (right) (http://www.wpc.ncep.noaa.gov/dailywxmap/index.html, NCEP, Weather Prediction Center). The green shadings represent occurrences of precipitation. A cold front passed through the southeastern Texas region during the time.

2.3. Weather conditions in September 2013

Simulations were performed for the month of September 2013, coincident with the DISCOVER-AQ campaign. The weather during the month was relatively dry with mostly southerly, easterly or southeasterly winds. The period of September 5th to 19th was marked by the absence of a strong synoptic weather pattern. The wind pattern was light northeasterly in the early morning, gradually turning clockwise to southeasterly in the afternoon and evening hours. A cold front passing on 20th and 21st September (Fig. 2.2) resulted in a sudden drop in surface temperatures and light to medium showers in the area. Light rain events occurred on 2nd, 10th, 16th, 19th to 21st, and 28th to 30th September. Events

on 20th and 21st September consisted of widespread light to medium showers (Li et al., 2016).

Chapter 3. Impact of high-resolution sea surface temperature, emission spikes and wind on simulated surface ozone during a high ozone episode

3.1. Introduction

Sea Surface Temperature (SST) plays an important role in regional circulation in coastal urban regions where intensity and direction of air flow can be influenced by variation in SST distribution and land-sea thermal contrast. Temporally varying SST fields were used to improve the simulation of meteorological conditions in the Greater Houston area (Byun et al., 2007; Kim et al., 2013). Byun et al. (2007) developed a method to estimate missing values of satellite SST measurements using monthly-averaged SST diurnal variations and adopted high-resolution hourly SST obtained from NOAA/NESDIS Geostationary Operational Environmental Satellites (GOES) in the Fifth-Generation NCAR/Penn State Mesoscale Model (MM5) meteorological model. Their model simulations for $26^{th} – 27^{th}$ September 2006 showed that the simulated ground temperatures of lakes and along the coast of the Gulf of Mexico were higher in the afternoon and the wind pattern was also modified because of changes in temperature differences between land and water bodies. However, none of these studies evaluated the effects of updated meteorological fields using temporally varied SST on air quality modeling. In this study, a

[1] This chapter is for "Impact of high-resolution sea surface temperature, emission spikes and wind on simulated surface ozone in Houston, Texas during a high ozone episode", published at *Atmospheric Environment* in December 2016 (doi:10.1016/j.atmosenv.2016.12.030). Authors are S. Pan, Y. Choi, W. Jeon, A. Roy, D. A. Westenbarger, and H. C. Kim.

WRF-SMOKE-CMAQ air quality modeling system was employed for two model simulations: one with standard WRF meteorological fields (BASE) and the other updated with hourly derived NOAA/NESDIS GOES satellite SST (SENS), to investigate the impact of high-resolution SST on simulated meteorological fields and O_3 and its precursors during the high O_3 episode in Houston on 25th September 2013. Hence, this study extends the use of temporally varied SST in meteorological models (Byun et al., 2007; Kim et al., 2013) to the air quality modeling system in the Houston area.

In addition to the uncertainty in SST, other possible causes of high O_3 and model prediction error include uncertainties in the emissions and wind fields. These will be investigated using the same modeling setup of WRF-SMOKE-CMAQ; the perturbations will be superimposed on the SENS case. The previous studies performed by Souri et al. (2016) and Li et al. (2016) addressed the limitation in the model simulations to properly simulate unexpected local emissions and wind fields respectively, during the high O_3 peak days. Souri et al. (2016) adjusted NO_x emissions using a Bayesian inverse modeling approach using OMI NO_2 column data. The modeling mitigated high NO_x biases from the standard CMAQ modeling but did not reduce the simulated short-term low biases in NO_x and O_3 concentrations during the high O_3 period of 25th September, 2013. Li et al. (2016) showed the limitation in simulating meteorological variables (e.g., wind fields) during high O_3 days; since the peak concentrations resulted due to meteorological stagnation episodes which are challenging to simulate.

It is known that stagnation events can be tricky to simulate using the WRF model. However, it is relatively easy to generate model wind fields that are similar to the

observations. The technical approach in this study is not to develop the better model, but to simulate wind fields similar to the observations and check how much these "improved" winds fields mitigate the simulated biases of O_3 and its precursors. Hence for the sensitivity cases, emissions of O_3 precursors and wind fields in the model were adjusted to investigate the impact of these changes on the timing and locations of the peak O_3 and their magnitudes. An extensive in situ measurement network of surface meteorological parameter, O_3 and its precursors from Texas Commission on Environmental Quality's Continuous Ambient Monitoring Stations (CAMS) and NASA's P-3B aircraft measurements collected during the DISCOVER-AQ campaign was used to investigate sources of model-measurement error. In addition to the SST sensitivity simulations, three separate simulations (with adjusted local emissions, with adjusted wind fields, and with adjusted local emissions and wind fields) were performed to help illustrate the contributions of emission uncertainty and wind patterns to daily peak O_3.

3.2. Methodology

3.2.1. Model set-up and observational data

The CMAQ model version 5.0.1 with CB05 chemical mechanism and AERO5 module, WRF model version 3.7, and SMOKE version 3.6 with NEI-2011 were used. The 4 km southeast Texas domain (84 columns × 66 rows) were used.

The NOAA/NESDIS Geostationary Operational Environmental Satellites (GOES) provide near real-time Level 3 SST measurements with a spatial resolution of approximately 6 km (0.05˚ × 0.05˚, latitude by longitude). Gridded datasets are available

with 1-, 3-, and 24-hour temporal resolutions. This study used the 1-hr resolution dataset (http://podaac.jpl.nasa.gov/dataset/GOES_L3_SST_6km_NRT_SST_24HOUR). The grid covers much of the Western Hemisphere bounded by 180°W, 30°W, 60°N and 45°S, from May 12, 2003 to present. The buoy observed water and air temperatures from the NOAA's National Data Buoy Center (NDBC) (http://www.ndbc.noaa.gov/) were used to evaluate the satellite SST.

The TCEQ's CAMS network meteorological factors (temperature, wind speed/direction, relative humidity) and chemical species (O_3, NO_x, NO, NO_2, ethylene, isoprene, toluene, and xylenes) were used. The NASA P-3B aircraft O_3, NO_y and HCHO measurements collected during DISCOVER-AQ Texas campaign were also used to evaluate simulated concentrations. The NOAA MADIS ACARS wind profiles were used to evaluate the wind aloft.

3.2.2. Simulation with SST update

Byun et al. (2007) assumed that SST is a function of surface location (x, y) and time that shows seasonal and diurnal variation. This can be constructed as

$$SST(x, y, t_s, t_d) = a \cdot sin\left(\frac{2\pi}{24}(t_d - d)\right) + m \quad (4.1)$$

$$a = a_{monthly\_mean}(x, y) \quad (4.2)$$

$$d = d_{monthly\_mean}(x, y) \quad (4.3)$$

$$m = m_{monthly\_mean}(x, y) + m_{daily}(t_s) \quad (4.4)$$

where a is the amplitude of SST variation (in Kelvins), d the phase shift, m the mean SST, t_d the hour of the day, and t_s the day of the month.

The approch of Byun et al. (2007) was used as a first estimate to fit diurnal variation sine curves for every water cell in the domain. Next, GOES SST input was constructed using satellite measurements and fitted sine curves for locations where observations were missing, and implemented in the WRF model. Two simulated cases were considered: (1) BASE – baseline WRF simulation, lower boundary for water bodies using skin temperature at initial simulation time; (2) SENS – update of the lower boundary for water bodies using hourly GOES SST during the run. Next, emission and air quality model simulations using the two meteorological inputs were performed. Fig. 3.1 shows the locations of the key areas.

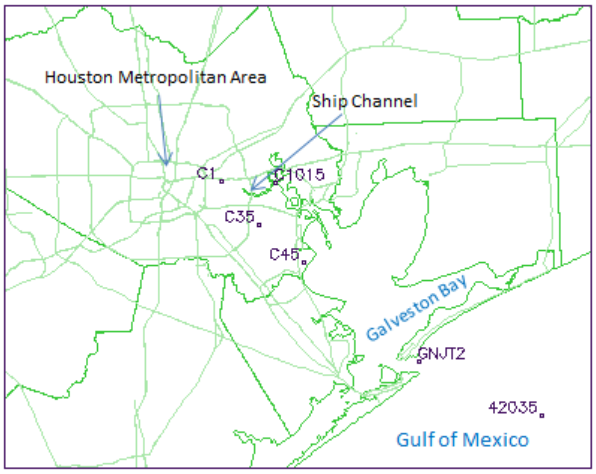

Fig. 3.1. Locations of the key areas in this study: Houston Metropolitan Area, Houston Ship Channel, Galveston Bay, Gulf of Mexico, several CAMS monitoring sites (C1, C35, C45 and C1015) at the industrial region, and two buoy sites (GNJT2 and 42035). Note this map is the only portion of the 4 km resolution horizontal modeling domain cover. The actual map is in 144 km × 112 km.

3.3. Results

3.3.1. Temporal variation of Sea Surface Temperature

The distribution of the constructed GOES SST amplitude and examples of the curve fitting results for September 2013 are shown in Fig. 3.2. Relatively high amplitudes along

the coast and at some reservoir and inland water bodies indicate that hourly GOES water temperature showed strong diurnal variations (typically >2˚C) at these regions, which were quite different from diurnal temperature variations (typically <1˚C) at outer ocean grid cells.

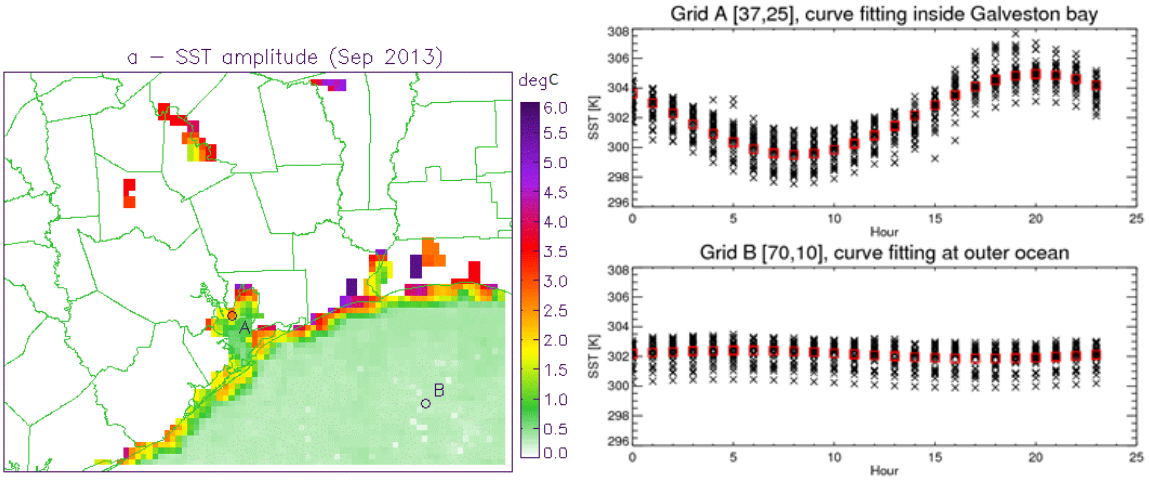

Fig. 3.2. Amplitudes of GOES SST diurnal variations (left) and examples of curve fitting inside Galveston Bay and at the outer ocean (right). Amplitude in equation (4.1) and (4.2) is the midpoint between the maximum and minimum values of a sine curve. The actual map (left) is in 336 km × 264 km. In the time series plots (right), the black symbols represent satellite observations and the red symbols represent fitted values.

Fig. 3.3 depicts a comparison of buoy temperature measurements and model-ready SST inputs of WRF model. The SST values in the BASE case remained constant throughout the simulation period because static SST fields were used in standard WRF run. The SENS case exhibited clearly diurnal variations, and the variability also generally corresponded to that of buoy measured temperatures, especially at the GNJT2 site. It should be noted that the temperature values were acquired from different altitudes. The buoy water temperatures were measured at about one meter below the water surface and buoy air temperatures were measured several meters above the water surface. The satellite acquired water temperatures right on or above the water surface. In this sense, satellite SST might

occasionally be closer to buoy air temperatures. The diurnal variations of satellite SST were relatively bigger at the near land site.

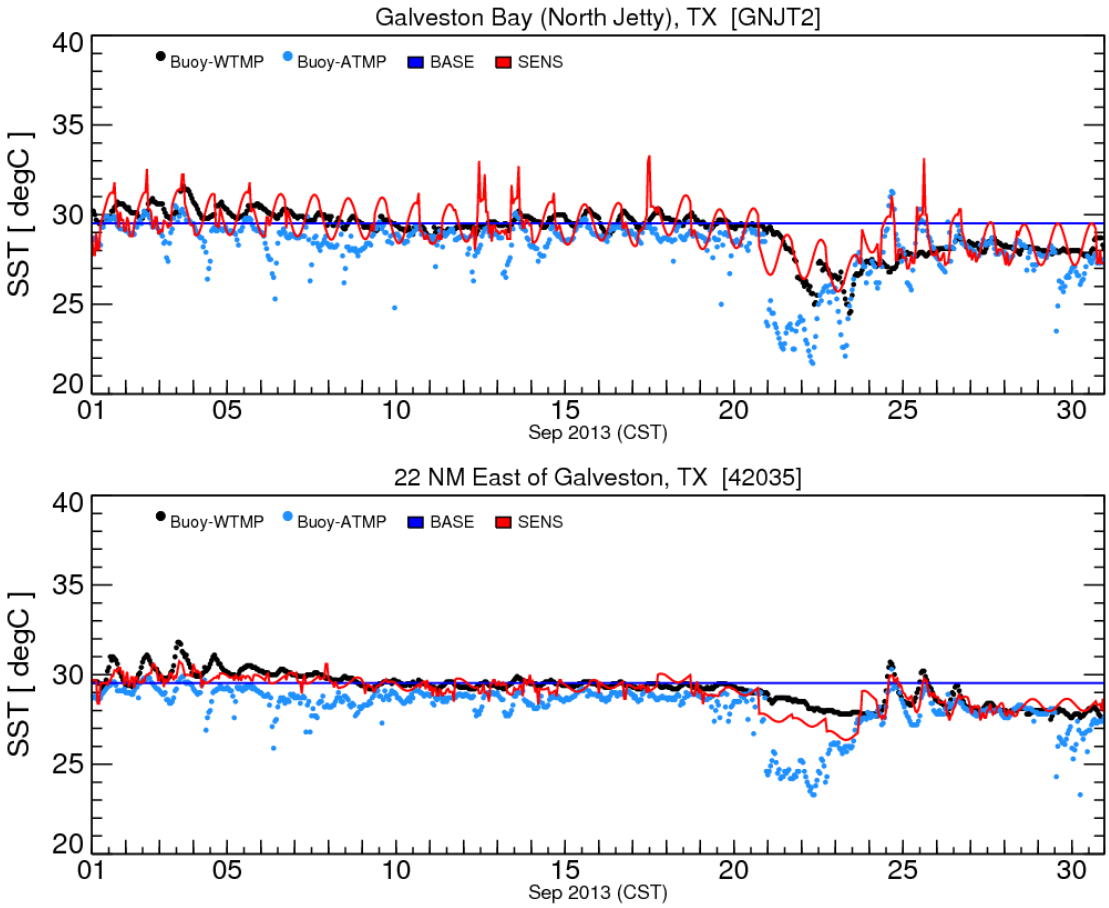

Fig. 3.3. Time series of sea surface temperature (SST) between buoy measured water temperature (WTMP) and air temperature (ATMP), and different SST inputs of WRF model. The locations of the two buoy sites are marked in Fig. 3.1. Buoy site GNJT2 is near land.

3.3.2. Basic meteorological model performance evaluation

Domain-wide time series comparisons of hourly 2-m temperature, relative humidity, and 10-m wind speed between CAMS observations and simulation results for the month of September 2013 are plotted in Fig. 3.4. Model simulated values captured observation trends well. The model over-predicted surface temperatures substantially between 20th and 22nd

September (by around 5-6 ^{o}C) likely due to low values caused by the cold front passage. Additionally, the simulated surface wind speed was routinely over-predicted by ~1 m s^{-1} during the daytime. Li et al. (2016) applied an observation nudging technique in a WRF meteorological simulation by assimilating in situ surface temperature and wind observations. Their results showed a notable improvement in surface temperature and wind simulations at monitoring stations. However, the observation nudging scheme sometimes introduced erroneous low-pressure systems in the domain (Li et al., 2016). It was not implemented in this study so as to distinctively see the influence of updated SST on simulated meteorological fields.

The correlation, index of agreement (IOA), and mean bias (MB) between CAMS observations and the BASE simulation for temperature (0.89, 0.93, and 1.0) and relative humidity (0.88, 0.93, and -1.9) during 24th – 25th September (Table 3.2) were better than for temperature (0.85. 0.89, and 1.2) and relative humidity (0.81, 0.89, and -2.5) during all of September (Table 3.1). Both observed and simulated wind speed during 24th – 25th September were lower than other days in September due to the passage of the cold front. Mean bias for wind speed during September 24th – 25th (0.5 m s^{-1}) was also smaller than that of September (0.9 m s^{-1}). Sea/land breezes are mostly common under quiescent synoptic conditions and may not be observed when the synoptic flow is strong. Thus it is appropriate to perform an analysis of SST impact on meteorological and air quality model predictions during the period of 24th to 25th September 2013 (the weak wind days).

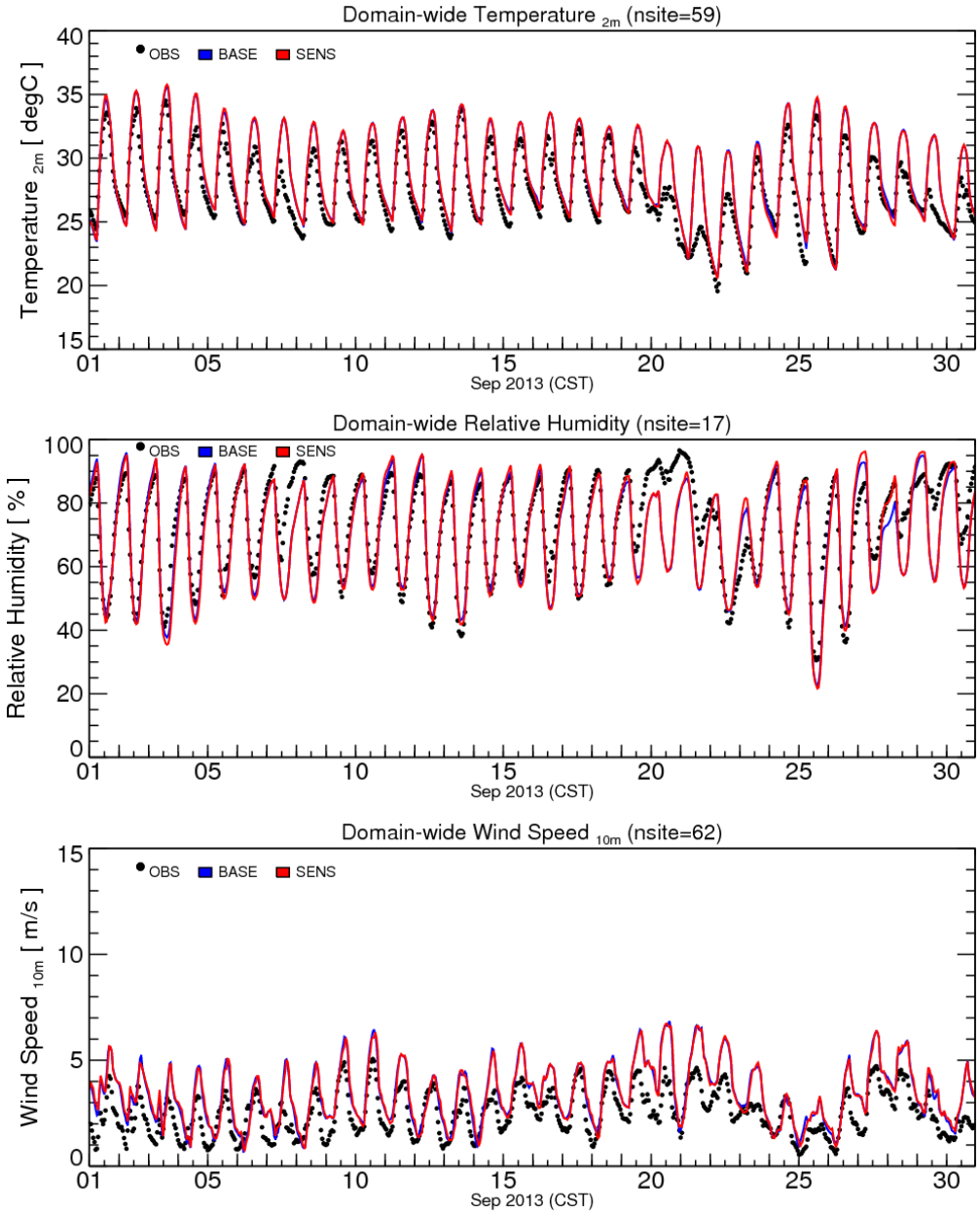

Fig. 3.4. Time series of domain-wide 2-m height temperature, relative humidity and 10-m height wind speed between TCEQ CAMS surface observations (OBS) and two model simulations (BASE and SENS).

3.3.3. Impact of high-resolution SST on simulated meteorological fields and O_3

Comparing with the BASE case, simulated SST was lower along coastal regions during the early morning in the SENS case (Fig. 3.5-b), due to the application of diurnal

SST variations obtained from the GOES satellite. BASE simulated 2-m temperatures over land were lower than over the Gulf and bay areas (Fig. 3.5-c). At the same time, the SENS case showed higher temperatures over land than BASE case and lower temperatures over water bodies (Fig. 3.5-d), indicating less land-sea thermal contrast than in the BASE case. The magnitudes of differences of 2-m temperature between simulations over water bodies bore resemblance to Byun et al. (2007). The reduced land-sea thermal contrast in the SENS case led to reduced wind speeds especially over the ocean in the morning (Fig. 3.5-f). This change of wind pattern could have a large impact on transport and distribution of air pollutants.

Table 3.1. Evaluation of meteorological factors for September 2013.

Variable	Case	N	R	IOA	MAE	MB	OM	MM	MM/OM
Temperature	BASE	41058	0.85	0.89	1.6	1.2	27.4	28.5	1.04
	SENS	41058	0.85	0.89	1.6	1.2	27.4	28.6	1.04
Relative Humidity	BASE	11754	0.81	0.89	8.1	-2.5	72.8	70.2	0.97
	SENS	11754	0.81	0.89	8.4	-2.4	72.8	70.4	0.97
Wind Speed	BASE	43246	0.68	0.75	1.3	0.9	2.5	3.4	1.38
	SENS	43246	0.65	0.74	1.3	1.0	2.5	3.4	1.39

Notation: N – Number of data points; R– Correlation; IOA – Index of Agreement; MAE – Mean Absolute Error; MB – Mean Bias; OM – Observed Mean; MM – Model Mean; MM/OM – Model Mean divided by Observed Mean. Units of MAE/MB/OM/MM for Temperature: ˚C, Relative Humidity: %, Wind Speed: m/s.

Table 3.2. Evaluation of meteorological factors for 24th – 25th September 2013

Variable	Case	N	R	IOA	MAE	MB	OM	MM	MM/OM
Temperature	BASE	2696	0.89	0.93	1.7	1.0	27.6	28.5	1.03
	SENS	2696	0.89	0.92	1.8	1.0	27.6	28.6	1.04
Relative Humidity	BASE	768	0.88	0.93	8.9	-1.9	64.4	62.5	0.97
	SENS	768	0.88	0.93	9.1	-1.6	64.4	62.7	0.97
Wind Speed	BASE	2866	0.47	0.66	0.9	0.5	1.7	2.1	1.27
	SENS	2866	0.49	0.67	0.9	0.5	1.7	2.1	1.27

Notation: Same as Table 3.1.

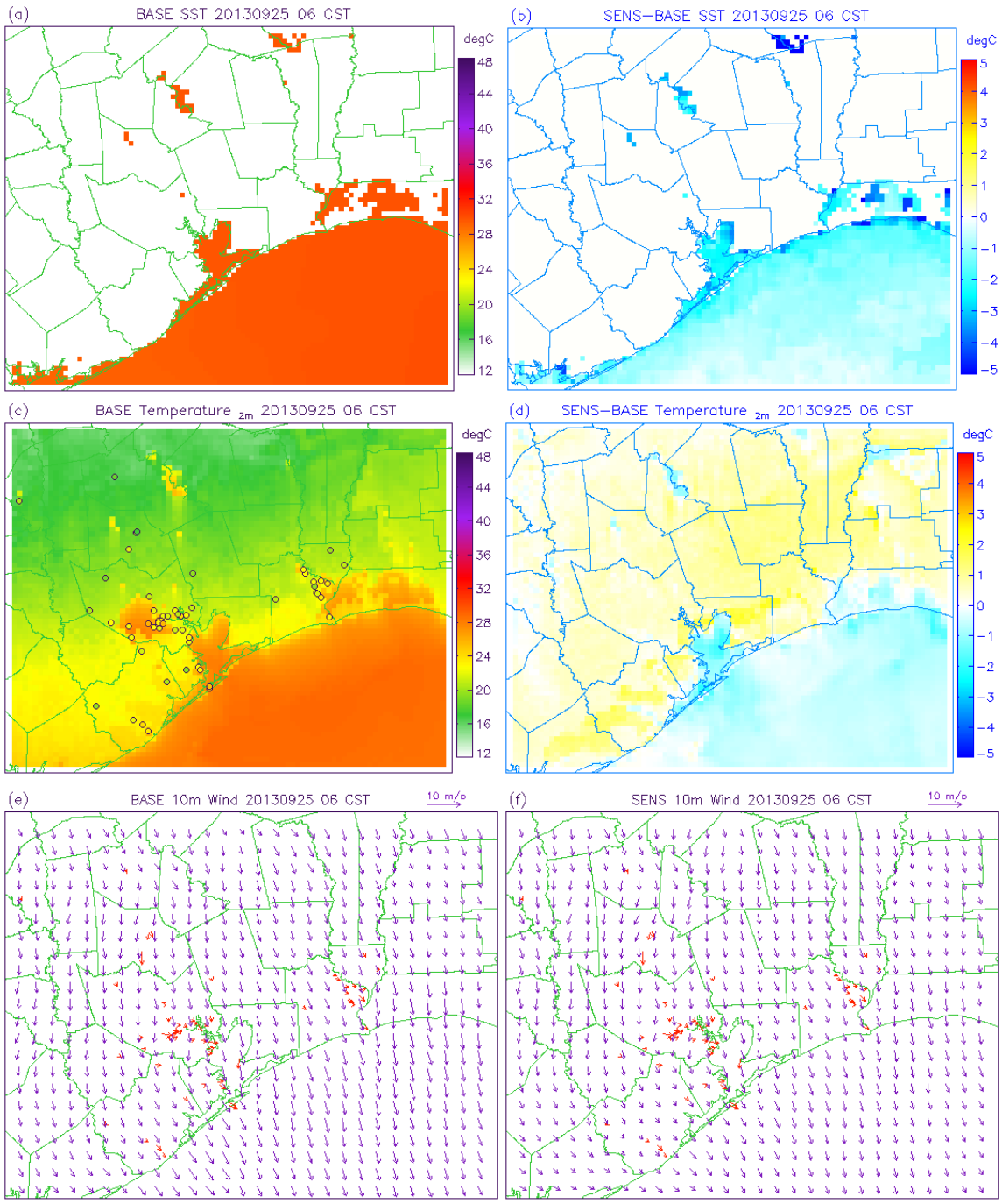

Fig. 3.5. Spatial distributions of meteorological fields at 06 CST on 25th September 2013: (a) BASE simulated SST; (b) SENS – BASE SST; (c) BASE 2-m temperature, with CAMS observed temperature (circle); (d) SENS – BASE 2-m temperature; (e) BASE 10-m wind (purple arrow), with CAMS observed wind (red arrow); (f) SENS 10-m wind with CAMS observed wind. The actual maps are in 376 km × 304 km for SST, and in 336 km × 264 km for 2-m temperature and 10-m wind.

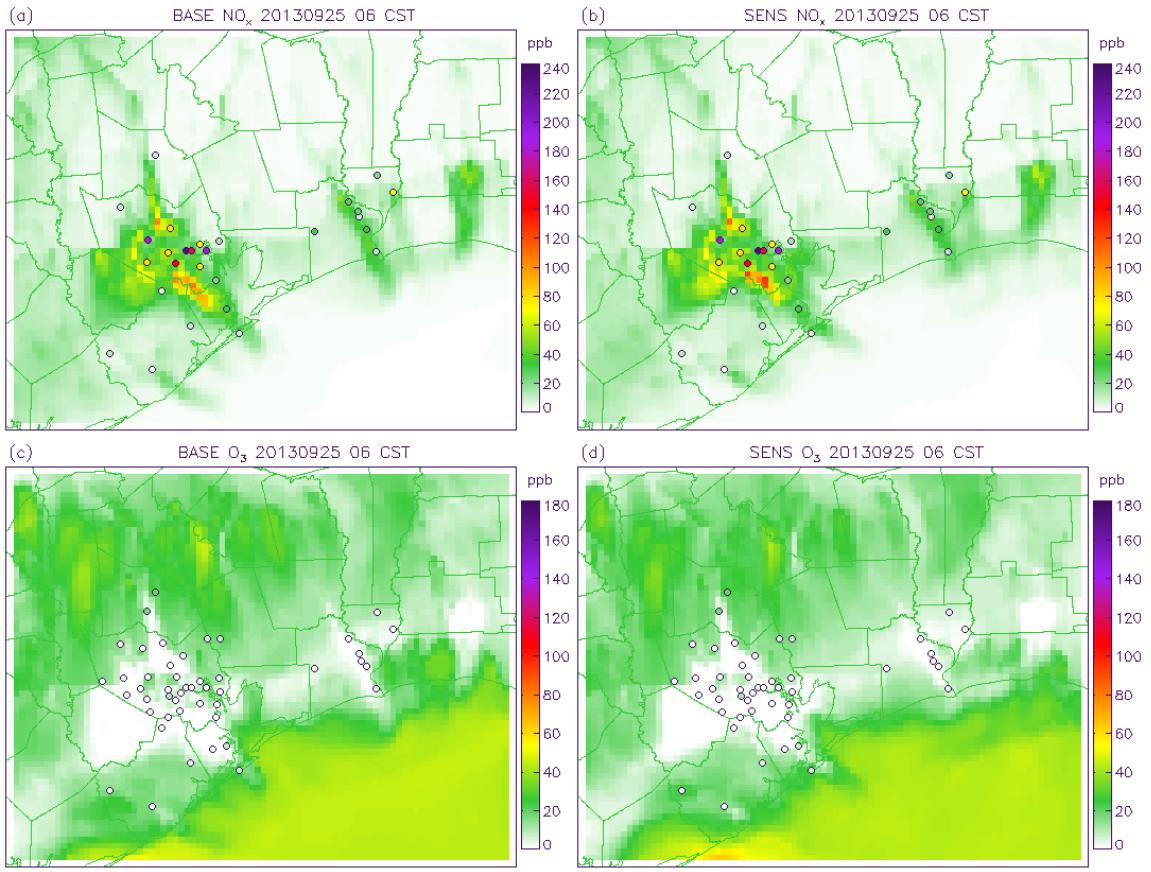

Fig. 3.6. Spatial comparisons of surface NO_x and O_3 at 06 CST on 25th September 2013: (a) BASE with CAMS NO_x; (b) SENS with CAMS NO_x; (c) BASE with CAMS O_3; (d) SENS with CAMS O_3. The actual maps are in 336 km × 264 km.

The spatial distributions for surface-level NO_x and O_3 at 06 CST on 25th September 2013 are plotted in Fig. 3.6. Pollutants accumulated at the surface during the night and early morning as the planetary boundary layer (PBL) height was low due to nighttime surface cooling (Rappenglück et al. 2008). High NO_x concentrations were predicted in urban and industrial areas such as those around the Ship Channel. Slightly higher values at areas exhibiting peak values for NO_x in the SENS case (Fig. 3.6-b) vis-a-vis the BASE case (Fig. 3.6-a) could be explained by the wind speed difference; the SENS case had slower wind speed than the BASE case at morning time (Fig. 3.5-e and 4.5-f), so transport of pollutants was also slower in the SENS case. Both observed and simulated surface O_3

concentrations at urban and industrial areas were reduced and lower than 10 ppb (Fig. 3.6-c and 4.6-d) due to nocturnal NO titration of O_3.

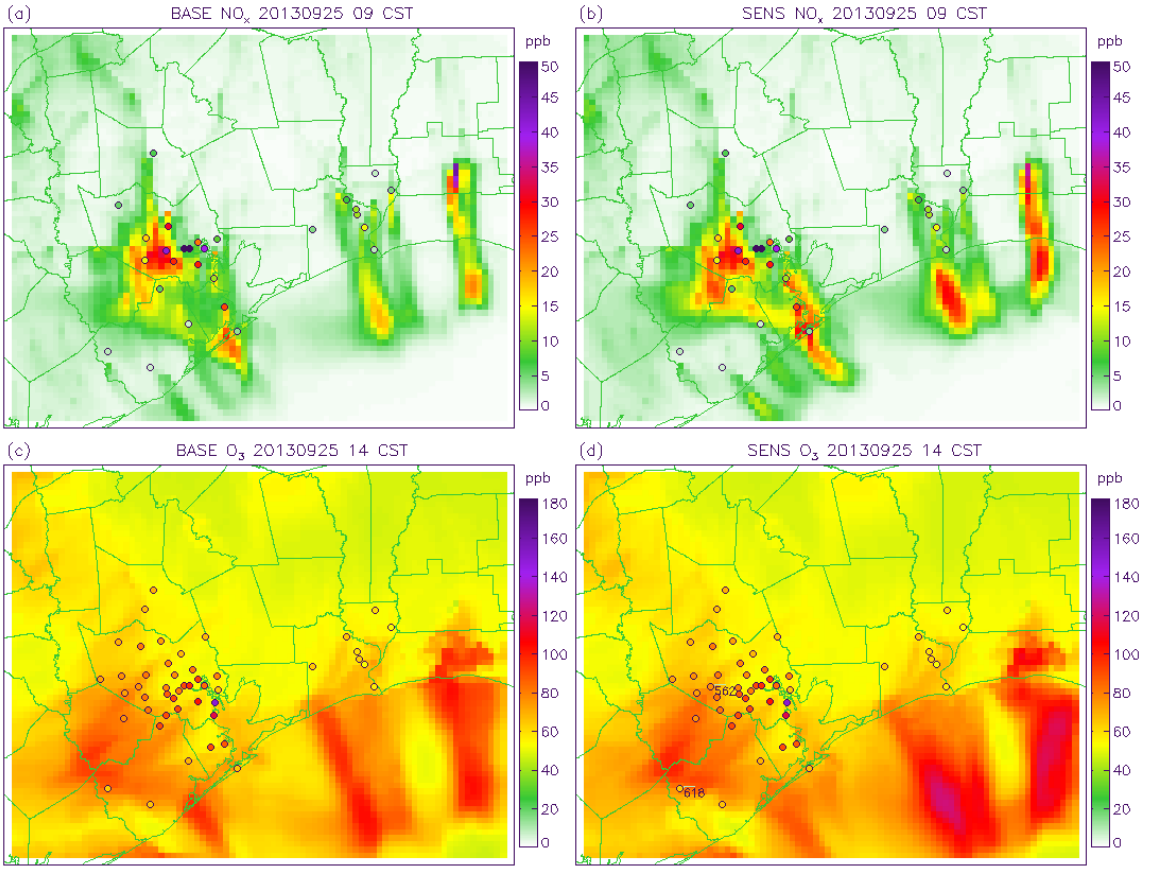

Fig. 3.7. Spatial comparisons of surface NO_x at 09 CST and O_3 at 14 CST on 25th September 2013. The actual maps are in 336 km × 264 km.

At 09 CST on 25th September 2013, due to the prevailing simulated northerly or northwesterly wind at early morning time, simulated NO_x that had accumulated around the urban areas moved slowly towards the south and formed several NO_x hotspots outside the coastline and over the Gulf (Fig. 3.7-a and 4.7-b). Maximum values at the center of these hotspots in the SENS case were significantly larger as the pollutants were less diluted by the relatively slower domain-wide wind. A formation of high O_3 downwind of these areas occurred a few hours later as the surface warmed. Maximum O_3 values in the SENS case

(Fig. 3.7-d) were also significantly larger than the BASE case (Fig. 3.7-c). While high O_3 episodes often occur as a result of active daytime photochemistry, near-surface meteorological conditions and transport processes during the night and early morning can impact morning O_3 precursor concentrations that initiate photochemistry. This influences both the location and magnitude of high pollutant concentrations (e.g., Banta et al. 2005; Jeon et al., 2012, 2014; Ngan et al. 2012, 2013).

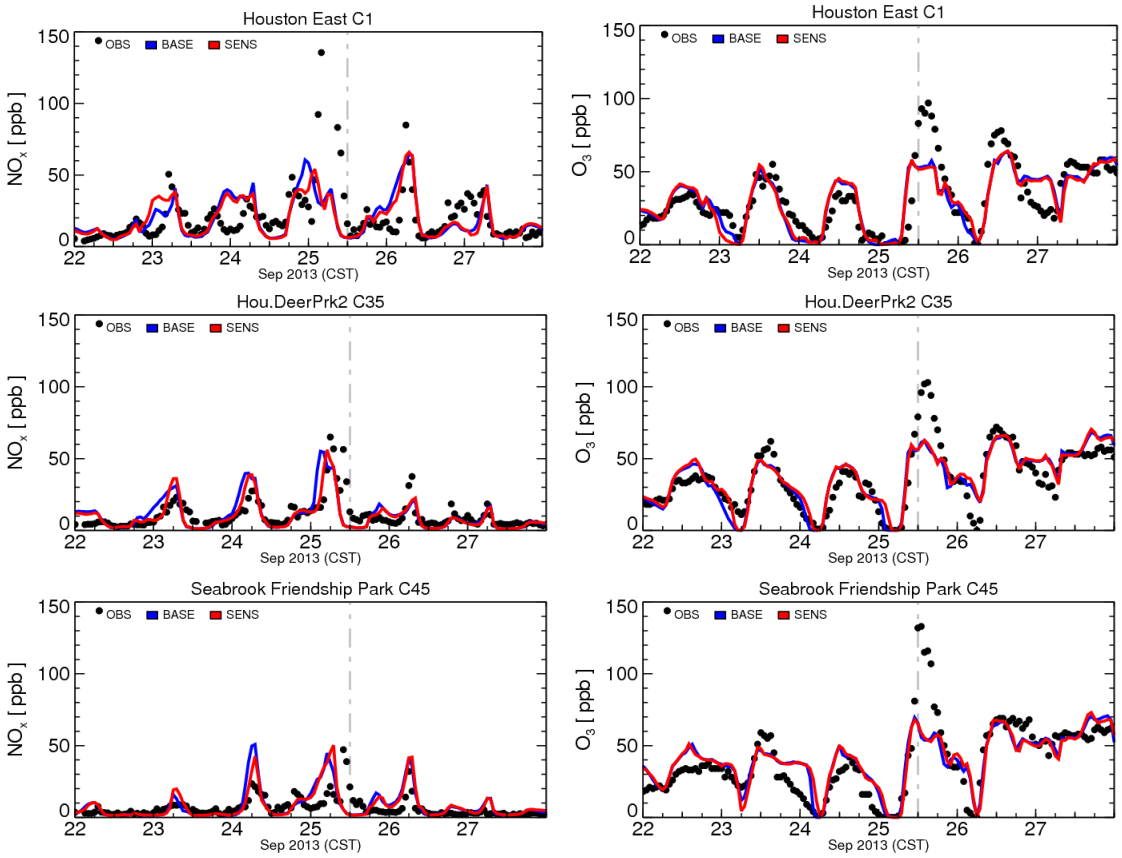

Fig. 3.8. Time series of surface NO_x (left) and O_3 (right) between CAMS surface observations (OBS) and two model simulations at three industrial monitoring sites (C1, C35, C45). The dashed line in each plot represents 12 CST on 25th September 2013.

The timing of observed NO_x peaks in the early morning of 25th September 2013 at three CAMS monitoring sites (C1, C35, C45) in the Ship Channel industrial region was

slightly improved by simulations using SST inputs as shown in Fig. 3.8 (in other words, the SENS simulated peaks shifted closer to the observed peaks). However, simulated O_3 changes were still marginal at these sites. A simulated O_3 change of about 5 ppb on the afternoon of 25th September could be seen at two monitoring sites (C562 and C618) located near the simulated peak O_3 (Fig. 3.7-d) over the land part of the domain as shown in Fig. 3.9. There was still a discrepancy between simulated and observed O_3 hotspots, and the model with updated SST failed to capture the high O_3 peak in the industrial area on 25th September.

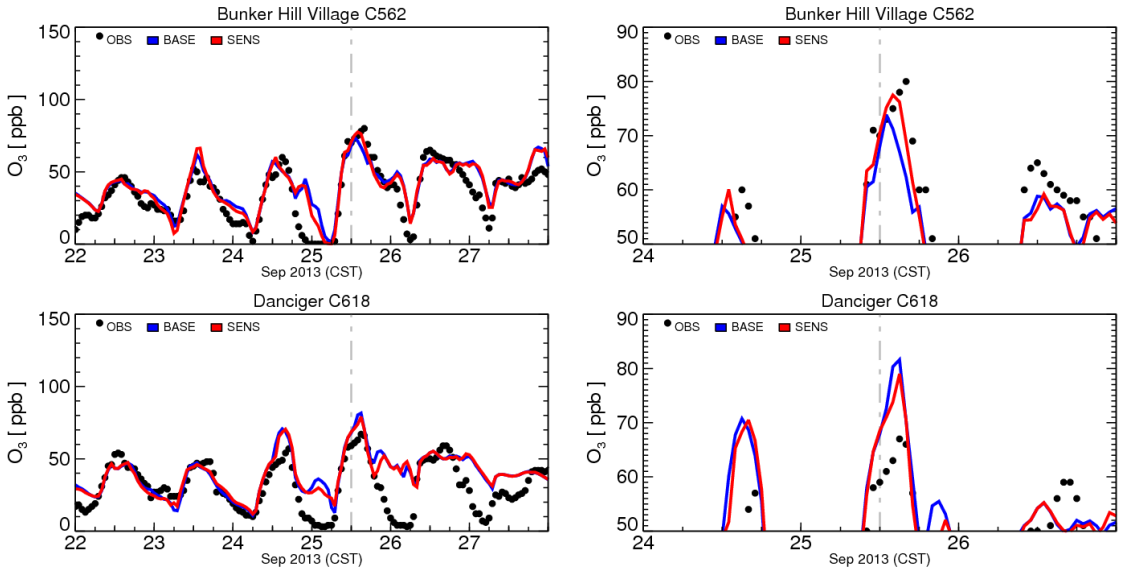

Fig. 3.9. Time series of surface O_3 between CAMS surface observations (OBS) and model simulations at C562 and C618 which were located near the area with peak simulated O_3. The right plots are the zoom-in of the left plots to show the simulated O_3 change on 25th September 2013. The dashed line in each plot represents 12 CST on 25th September 2013.

3.3.4. Possible cause of the high O_3 episode on 25th September 2013

The simulation results presented in the previous sections indicated that surface O_3 was significantly under-predicted in the industrial area during the afternoon of 25th September 2013 (Fig. 3.7 and Fig. 3.8). It must be noted that previous modeling studies

also reported this discrepancy (Loughner et al., 2015; Nopmongcol et al., 2015; Pan et al., 2015; Li et al., 2016). Additionally, high O_3 concentrations were also observed by the P-3B aircraft west and northwest of Galveston Bay as shown in Fig. 3.10. Hence, the cause of this observed high O_3 event and reasons for model under-estimation need to be further investigated.

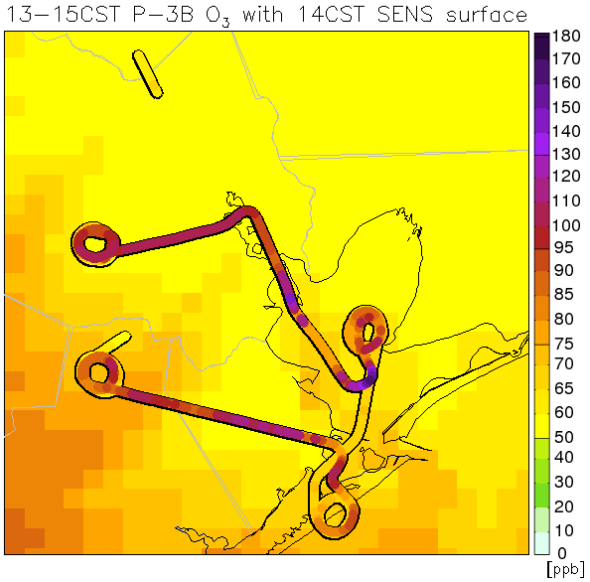

Fig. 3.10. O_3 measurements along NASA P-3B aircraft tracks on 25th September 2013 between 13 and 15 CST, overlaid upon SENS simulated surface O_3 at 14 CST in industrial and bay areas. The actual map is in 108 km × 104 km.

Excessively high concentrations of NO_x and VOC species were observed during the morning of 25th September 2013 at several surface monitoring stations. Spatial heterogeneity of observed NO_x and a mismatch of high NO_x concentrations between observations and simulations at urban and industrial areas were seen in previous sections (Fig. 3.6 and Fig. 3.7). Although the three industrial sites in Fig. 3.8 had similar high O_3 on 25th September, NO_x patterns at each site were quite different. The CAMS site C1 Houston East is located on the north side of the Ship Channel, close to industrial facilities

and several roadways. NO_x observations at this site were relatively high among the three sites in Fig. 3.8; while during the morning of 25th September, exceptionally high observed NO_x events occurred. Abnormally high concentrations of several highly reactive VOCs such as ethylene, isoprene, toluene and xylenes were also observed in the northern portion of the Ship Channel as shown in Fig. 3.11. These high values could be caused by large unexpected episodic flare emissions (Murphy and Allen, 2005; Vizuete et al., 2008), over-assisted flaring events (Loughner et al., 2015) or accidental mobile source releases.

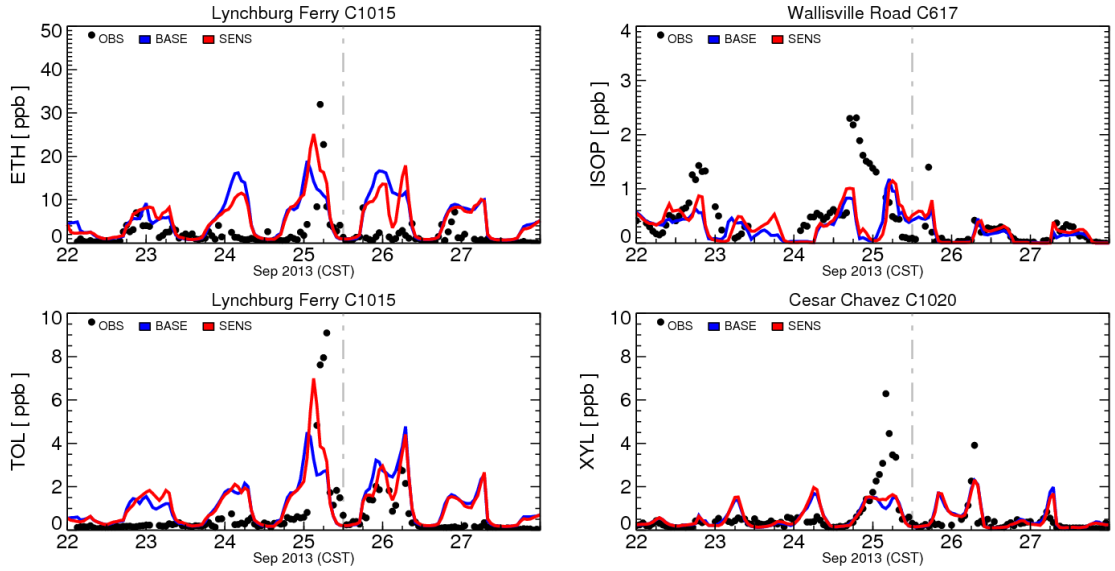

Fig. 3.11. Map of the VOC monitoring sites at Houston industrial region. And time series of several highly reactive VOC species between TCEQ Auto-GC measurements (OBS) and simulations (ETH: ethylene; ISOP: isoprene; TOL: toluene; XYL: xylenes).

Stable boundary layer conditions and model-measurement discrepancies for wind pattern in the early morning are possible sources of error. As shown in Fig. 3.12, high NO_x concentrations were detected in the northern portion of the industrial region (three circles lying almost in a horizontal line), which lasted for the entire morning period (05-10 CST, Fig. 3.13). Most other sites nearby still reported background level NO_x concentrations. For example, the site C35 Deer Park2 is about 8 miles away from C1 and located near industrial

facilities but enhanced NO_x was not observed during this period at this site. This suggests very stable surface layer conditions in the region, a shallow boundary layer was also observed during this interval (Li et al. 2016). Observed winds in the industrial region were calm or very weak westerly, which slowly but continuously transported pollutants to Galveston Bay as seen in Fig. 3.12. Simulated high NO_x concentrations were also located along major roadways (Freeway I-45 and another roadway reaching to urban core) during 05 to 07 CST (06 to 08 a.m. Local Time, morning rush hours) and simulated winds were northerly or northwesterly (land breeze pointing to the Gulf), pushing pollutants south.

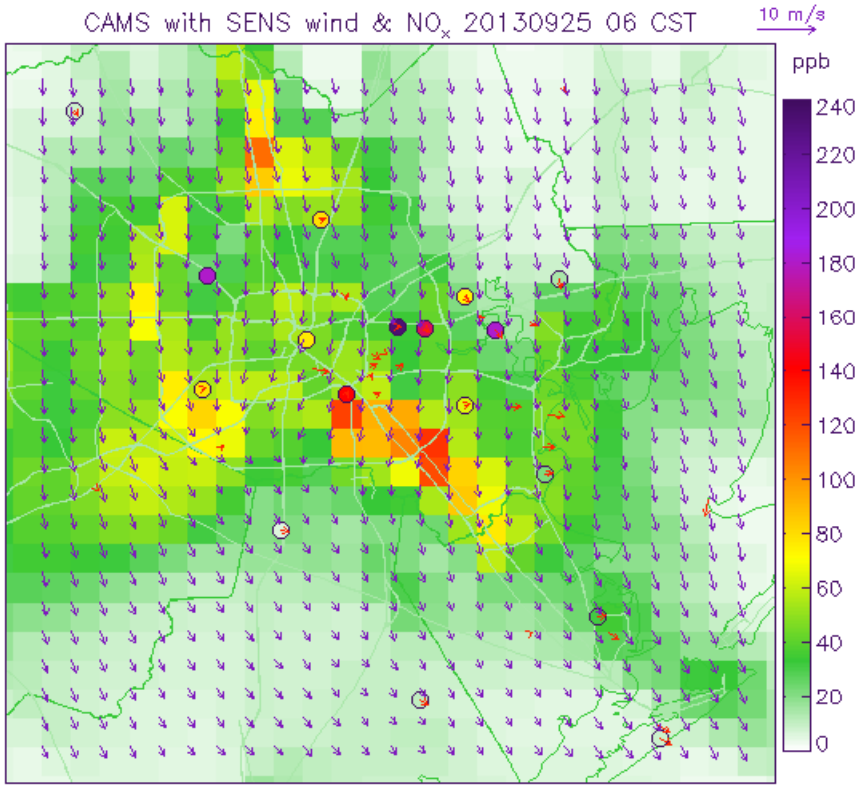

Fig. 3.12. Spatial comparisons of surface wind fields and NO_x concentrations between CAMS observations and SENS simulation at 06 CST on 25th September 2013 (red arrow: CAMS wind; purple arrow: SENS wind; circle: CAMS NO_x; background color: SENS NO_x). The actual map is in 104 km × 100 km.

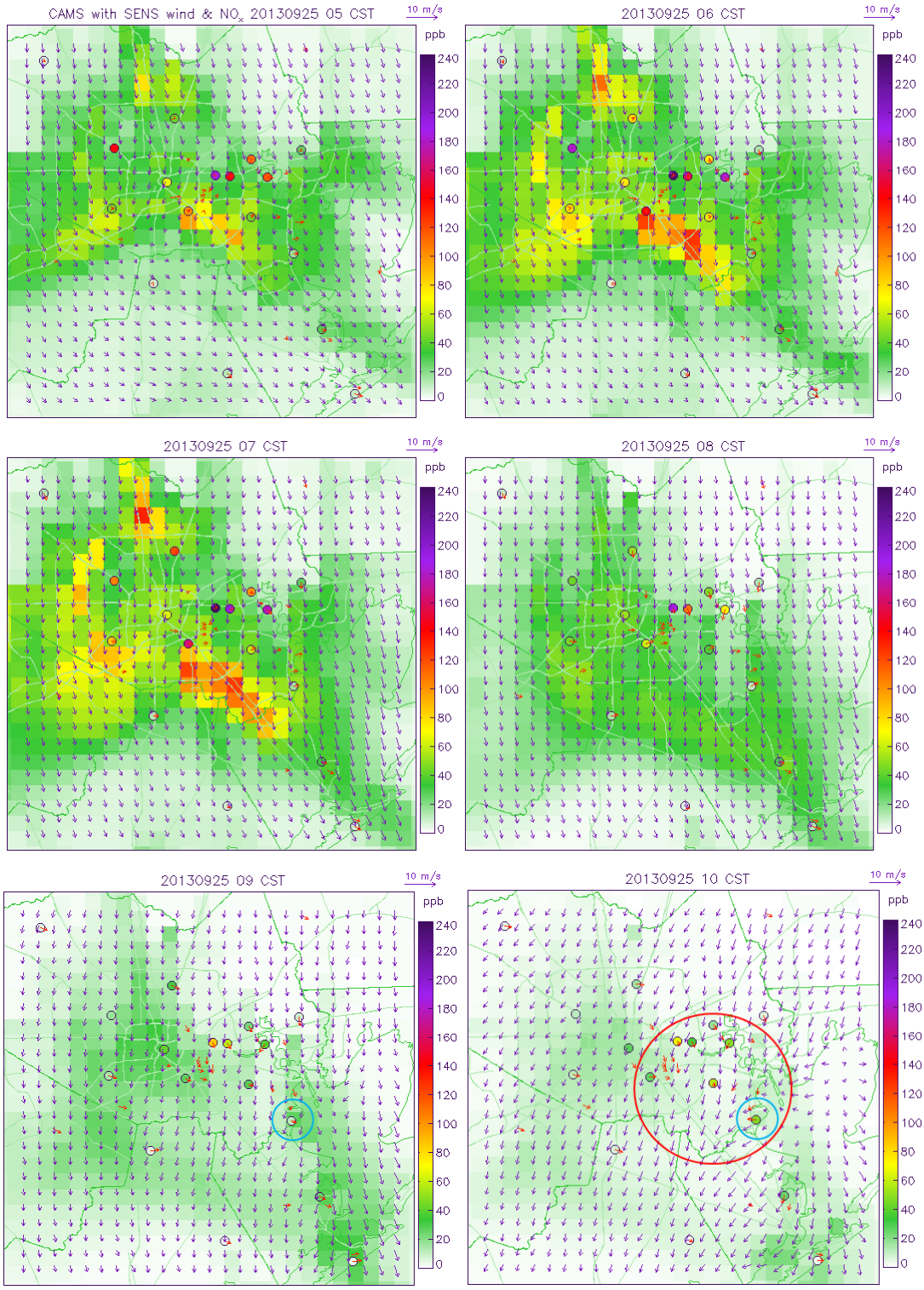

Fig. 3.13. Same as Fig. 3.12 in the paper but for the time span from 05 CST to 10 CST on 25th September 2013. The actual maps are in 104 km × 100 km.

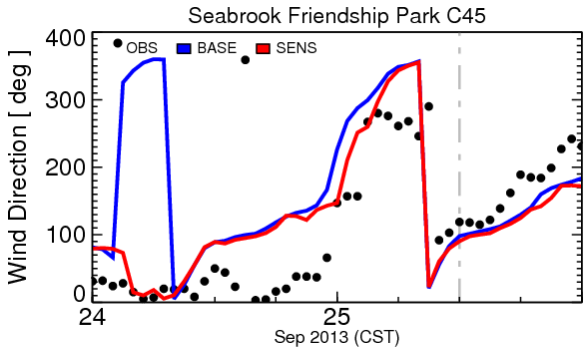

Fig. 3.14. Time series of surface wind direction between CAMS observations (OBS) and two model simulations at monitoring site C45 during 24th – 25th September 2013. Wind direction is reported in degrees with 0° or 360° representing northerly wind (or the wind from the north), 90°, 180° and 270° representing easterly, southerly and westerly, respectively. The dashed line in the plot represents 12 CST on 25th September 2013. A reversal of wind field from roughly westerly to easterly was observed between 09 CST and 10 CST on 25th September 2013.

Reversal of the observed wind field from land breeze to bay breeze happened between 9 and 10 CST at the western coastline of Galveston Bay (marked by blue circles in plots of 09 CST and 10 CST in Fig. 3.13). Time series of the wind reversal is plotted in Fig. 3.14. The bay breeze could return the pollutants which were previously blown into the bay in the early morning hours to the industrial area. This localized circulation phenomenon was also described by Banta et al. (2005) in their TexAQS-2000 study and Ngan et al. (2012) in their TexAQS-2006 study. After the wind reversal, a wind converging zone formed in the industrial area (marked by a red circle in the plot of 10 CST in Fig. 3.13). The converging zone persisted for the following several hours. High observed surface O_3 appeared first at the wind reversal area around noon time and extended to the industrial area and parts of the urban area by afternoon. Interestingly, areas with observed peak O_3 coincided with the wind converging zone. The observed peak O_3 areas and wind converging zone also matched with the location defined in Couzo et al. (2012), which indicated that 60% - 90% of all non-typical O_3 changes (NTOCs, at least 40 ppb in 1 hour,

or 60 ppb in 2-hour) (Vizuete et al., 2011) were measured in Houston during the years 2000 to 2009.

3.3.5. Impact of emission spikes and wind field change on simulated O_3

The extremely high daytime O_3 discrepancy over the industrial region could not be fully explained using improved SST inputs. However, it could potentially be attributed to the combined effects of SST and discrepancy in both local wind patterns and model emissions. These additional sensitivities on the SENS case were investigated by performing the following simulations:

(1) SENS-EMIS: Excessively high concentrations of NO_x (Fig. 3.8 and Fig. 3.12) and VOC species (Fig. 3.11) were observed during the morning of 25th September 2013 at several TCEQ CAMS surface monitoring sites. These could be caused by large emission upsets (e.g., Loughner et al., 2015; Souri et al., 2016). We adjusted the emissions at these locations to check their impact on O_3 simulation. Firstly, time series during September 2013 were plotted for O_3 precursor species which are routinely measured at the TCEQ CAMS surface sites and explicitly simulated in the CMAQ model. These species are NO, NO_2, and four highly reactive VOCs (ethylene, isoprene, toluene, and xylenes). For each species, we reviewed the time series at each site and selected the site which has significantly higher observed peaks during 25th September. For instance, at Houston East C1, observed NO peaks were lower than 45 ppb during most days except 7 CST on 25th September, when the peak was 235 ppb. Next, simulated/observed ratios at each hour between nighttime of 24th September and morning of 25th September were calculated, and emissions at these locations were adjusted using the following formulas:

$$ratio(species, site, hr) = \frac{sim(species,site,hr)}{obs(species,site,hr)} \quad (4.5)$$

$$EMISSION_{adj} = EMISSION/ratio(species, site, hr) \quad (4.6)$$

Table S3 and S4 in the supplemental information of Pan et al. (2017a) listed all the emission scaling factors. The factors are dependent on species, monitoring site location, and hour of the day. The SMOKE final merged emissions were adjusted and the emissions were added to surface layer grid cells. The hourly adjusting factors were used to get model O_3 precursor species reproduce the temporal variations of observations. The SENS-EMIS simulation was performed using adjusted emissions.

Table 3.3. Wind adjusting factors (1/ratio) for 25th September 2013.

Date	Hour	OM	MM	MM/OM (ratio)	1/ratio
09/25/2013	0:00	0.5	1.2	2.19	0.46
	1:00	0.6	0.9	1.66	0.60
	2:00	0.6	1.1	1.80	0.55
	3:00	0.7	1.1	1.67	0.60
	4:00	0.8	1.5	1.87	0.53
	5:00	0.8	1.7	2.03	0.49
	6:00	0.9	1.8	2.00	0.50
	7:00	1.2	2.1	1.67	0.60
	8:00	1.7	2.2	1.27	0.79
	9:00	1.7	2.1	1.24	0.81
	10:00	1.7	2.4	1.42	0.70
	11:00	1.6	2.6	1.58	0.63
	12:00	1.6	2.6	1.63	0.62
	13:00	1.7	2.5	1.47	0.69
	14:00	1.6	2.5	1.56	0.65
	15:00	1.7	2.5	1.47	0.66
	16:00	1.8	3.1	1.72	0.58

Notation: OM – Observed Mean; MM – Model Mean; MM/OM – Model Mean divided by Observed Mean. Units of OM and MM for Wind Speed: m/s.

(2) SENS-WIND: Simulated wind vectors in the meteorological input files were adjusted to represent the morning time weak westerly and afternoon wind converging zone. For the early morning (0 – 7 CST) of 25th September 2013, simulated/observed ratios of domain-wide surface wind speed at each hour were calculated, then the U- and V-components of simulated wind vectors were switched to effectively represent the weak westerly using the following formulas:

$$ratio(hr) = \frac{\sum_{i=1}^{n} sim(i,hr)/n}{\sum_{i=1}^{n} obs(i,hr)/n} \quad (4.7)$$

$$UWINDC_{adj} = |VWINDC|/ratio(hr) \quad (4.8)$$

$$VWINDC_{adj} = -|UWINDC|/ratio(hr) \quad (4.9)$$

Where *n* is the number of monitoring sites. Table 3.3 lists the hourly mean wind speed from 52 CAMS surface monitoring sites and corresponding model grid cells in the SENS case, the domain-wide simulated/observed ratios, and wind adjusting factors. Only the wind adjusting factors (1/ratio) between 0 – 7 CST of 25th September 2013 were used in the SENS-WIND and SENS-TOT cases. The early morning wind adjustment was applied from the surface to a height of about 160 meters (3 model vertical layers, early morning time PBL height). From 9 to 16 CST, same simple converging wind fields were used for each hour. The wind adjustment was from the surface to about 2 km (17 model vertical layers, daytime PBL height). The simulation was then performed using adjusted meteorological inputs. It should be noted that even as we adjusted the horizontal wind vectors in meteorological (MCIP output) files, the other meteorological variables were unchanged. In reality, if horizontal winds are changed, other meteorological factors (vertical wind, temperature, heat flux, etc.) will subsequently be changed. Hence the impact

of varied horizontal winds simulated by CMAQ can be different from that of real. Our corrections cannot fully consider them, so this is one of the drawbacks of our method. This approach is only used to check how simulations of O_3 and its precursors would respond, by effectively adjusting simulated wind fields closer to the in situ data. Due to the sparse number of wind observations, we cannot obtain a full picture of the three-dimensional wind fields. If the large O_3 bias could be mitigated by using the adjusted model wind fields, we may expect that similar wind conditions may result in high O_3 episode over the surface.

(3) SENS-TOT: This simulation case used both adjusted emissions and adjusted wind fields from the previous two scenarios. Fig. 3.15 depicts two examples of adjusted wind field inputs for the SENS-WIND and SENS-TOT cases. The simulated wind vectors matched better with the CAMS surface observations after adjustment. Fig. S4.16 plots wind profiles using data taken from aircraft taking off and landing at airports. The NOAA MADIS Aircraft-based dataset provides data obtained from many U.S. airlines reporting through Aircraft Communications Addressing and Reporting System (ACARS). Wind profiles were used to evaluate the adjusted winds aloft in the SENS-WIND and SENS-TOT cases. As shown in Fig. 3.16, at 7 CST of 25th September 2013, westerly winds were observed below 200 m (green arrows) near William P. Hobby Airport (HOU); the near-surface adjusted model winds were also westerly during the early morning. During daytime, observed winds at different altitudes above HOU airport were generally westerly; observed winds above IAH airport blew towards the Ship Channel region (in plots of 13 CST and 16 CST). We expect that the observed bay breeze at the western coastline of Galveston Bay might extend from surface to a height of approximately 1000 m. Then a combination

of these would form converging wind fields, which could be roughly represented by the adjusted model wind fields during the daytime.

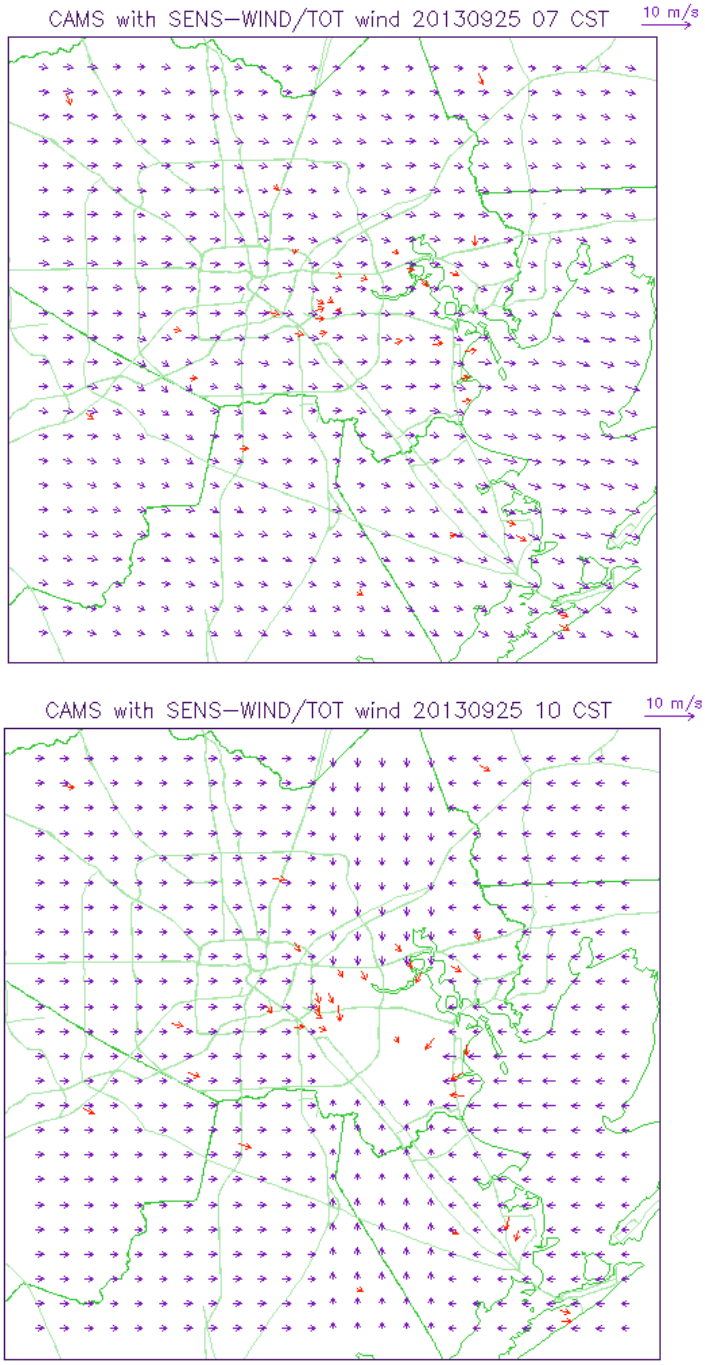

Fig. 3.15. The spatial pattern of adjusted wind fields input in the SENS-WIND and SENS-TOT cases. Note the original wind fields in SENS and SENS-EMIS cases were plotted in Fig. 3.13. The actual maps are in 104 km × 100 km.

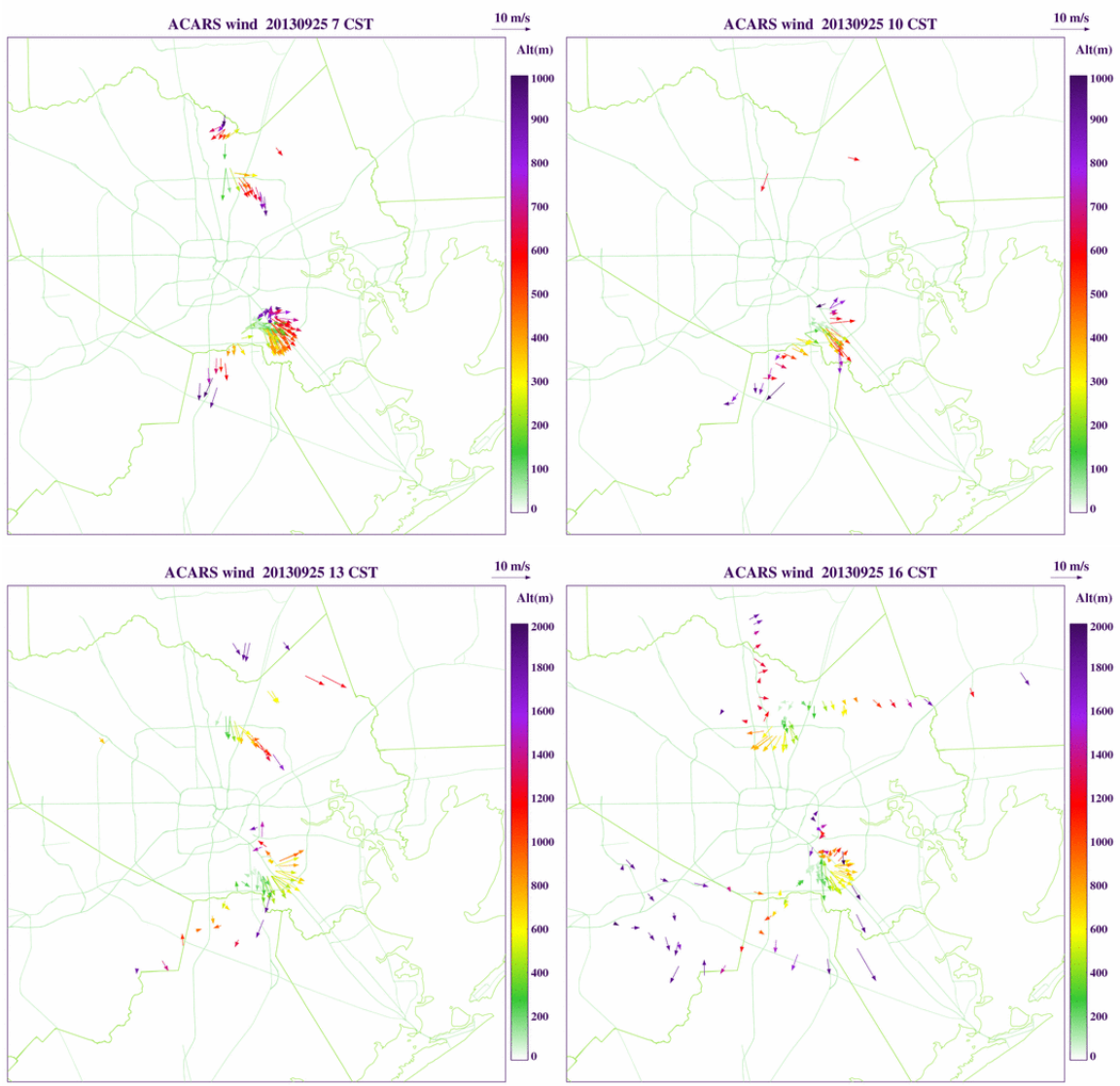

Fig. 3.16. ACARS wind profiles of 0-1000 m at 7 CST and 10 CST, and of 0-2000 m at 13 CST and16 CST. The data were recorded by aircraft taking off and landing at airports. The actual maps are in 112 km × 112 km.

3.3.5.1. NO_x sensitivities

As shown in Fig. 3.17, simulated NO_x concentrations agreed well with observations at monitoring sites reporting high concentrations (>100 ppb) in the morning for the SENS-EMIS case. This could be explained by application of updated emissions. Enhancements of simulated NO_x at sites that observed high NO_x concentrations in the SENS-WIND case

were smaller (about 20 ppb increases); significant under-estimation was still noticed at these locations. However, simulated NO_x concentrations demonstrated a domain-wide increase of about 40-80 ppb in the SENS-WIND case due to a reduction in wind intensity and an increase in westerly transport. The largest enhancement of simulated NO_x was obtained in the SENS-TOT case. In this case, both the magnitudes and the locations of NO_x hotspots matched well, resulting from improved wind fields and emissions.

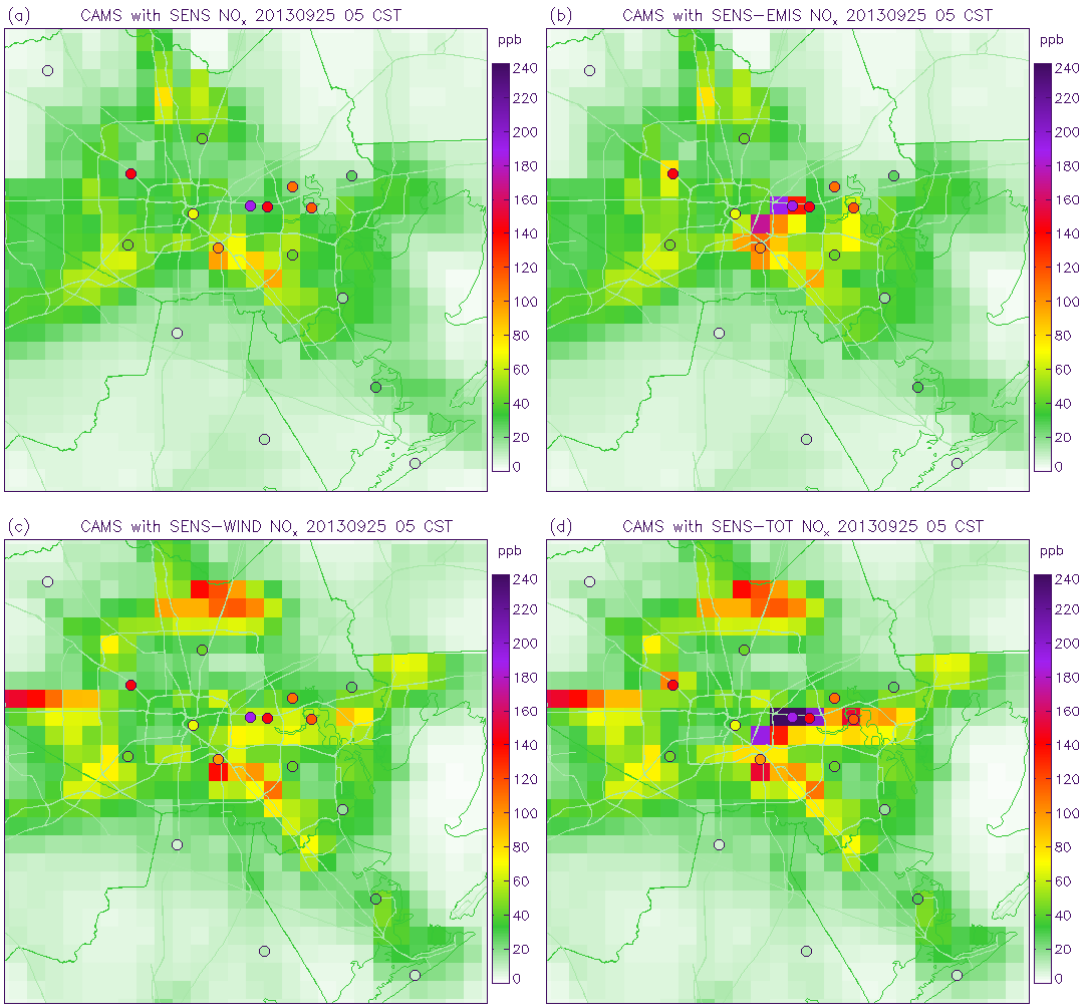

Fig. 3.17. Spatial comparisons of surface NO_x between CAMS observations and four sensitivity simulations (SENS, SENS-EMIS, SENS-WIND, and SENS-TOT) at 05 CST on 25th September 2013. The actual maps are in 104 km × 100 km.

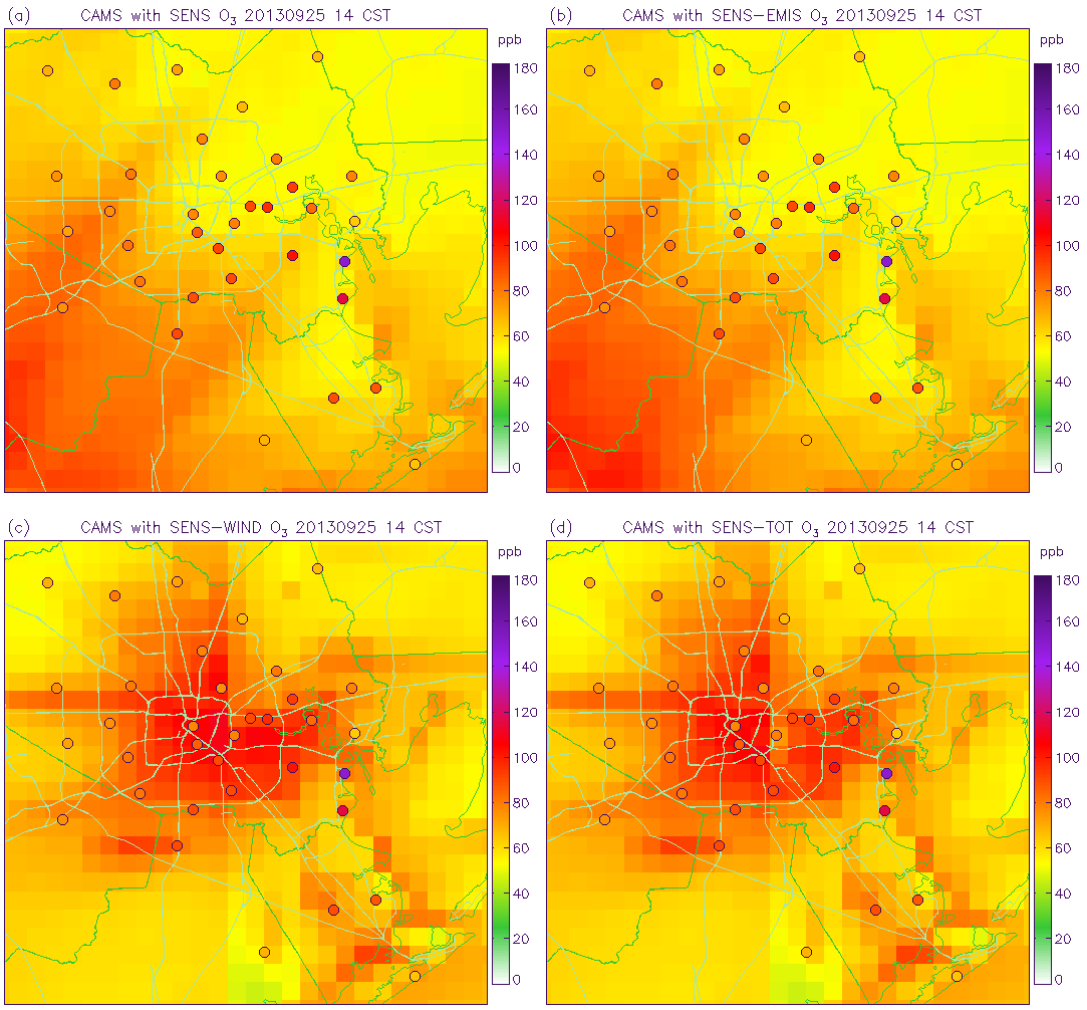

Fig. 3.18. Spatial comparisons of surface O_3 between CAMS observations and four sensitivity simulations (SENS, SENS-EMIS, SENS-WIND, and SENS-TOT) at 14 CST on 25th September 2013. Panel (a) is a zoom-in of the Fig. 3.7-d in urban-industrial-bay areas. The actual maps are in 104 km × 100 km.

3.3.5.2 Ozone sensitivities

Similar to the SENS case, the afternoon (14 CST) simulated O_3 hotspots did not coincide with the observed high values in the SENS-EMIS case, as can be seen in Fig. 3.18. The SENS-EMIS simulated O_3 hotspot was located to the southwest of the observations, again due to the erroneous wind pattern. The enhanced O_3 precursors were transported southwards by northerly wind in the early morning (before 9 CST), and southwestwards

by the northeasterly bay breeze after 9 CST (Fig. 3.13). Hence the model is unable to predict the expected O_3 enhancement over the industrial source region. However, both the magnitude and location of the simulated O_3 peak matched very well with surface observations in the SENS-WIND and SENS-TOT cases (Fig. 3.18-c and 4.18-d), highlighting the important effects of corrected meteorological fields in simulating regional O_3 concentrations.

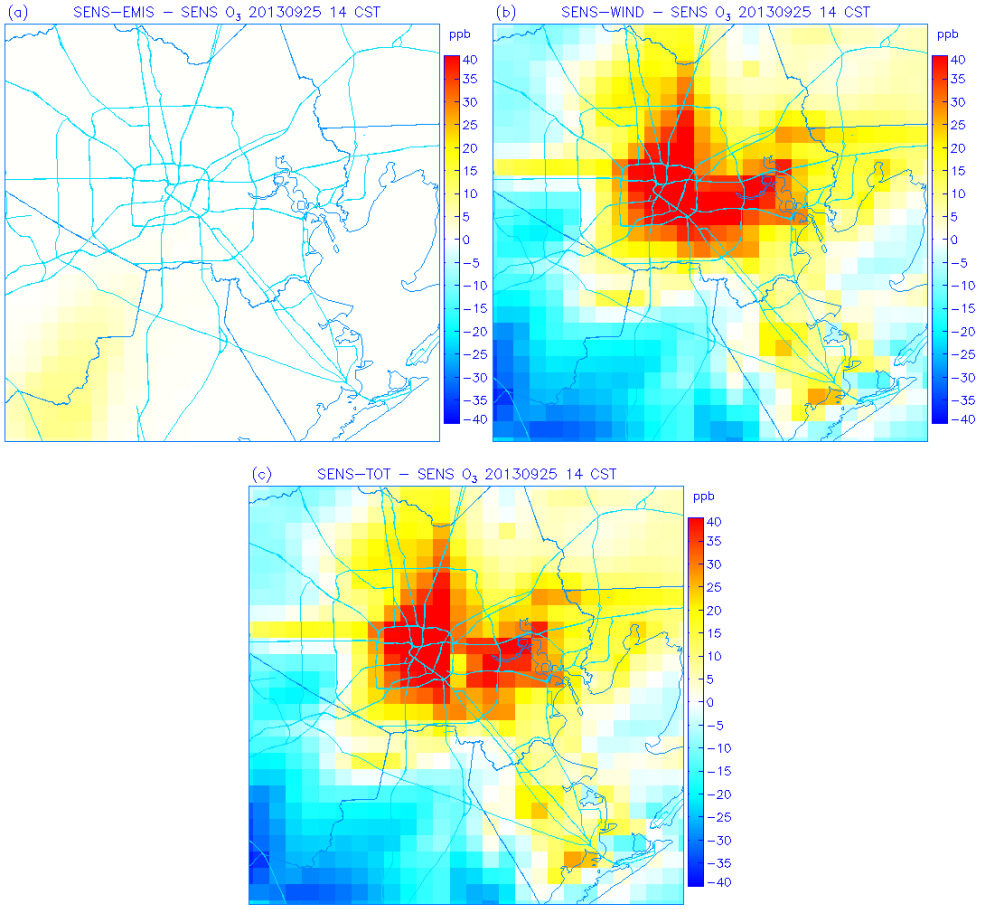

Fig. 3.19. The spatial difference of surface O_3 at 14 CST on 25th September 2013 between different simulations: (a) SENS-EMIS – SENS; (b) SENS-WIND – SENS; (c) SENS-TOT – SENS. The actual maps are in 104 km × 100 km.

Fig. 3.19 plotted the difference plots of afternoon surface O_3 between different simulation cases to illustrate the impact of emission and wind adjustments. The purpose of

wind adjustments (e.g., stagnation and converging zone) for the SENS-WIND and SENS-TOT cases was to aid the accumulation of O_3 precursors and subsequently O_3 formation over the source regions. Wind adjustments also significantly impacted O_3 precursor concentrations and distributions.

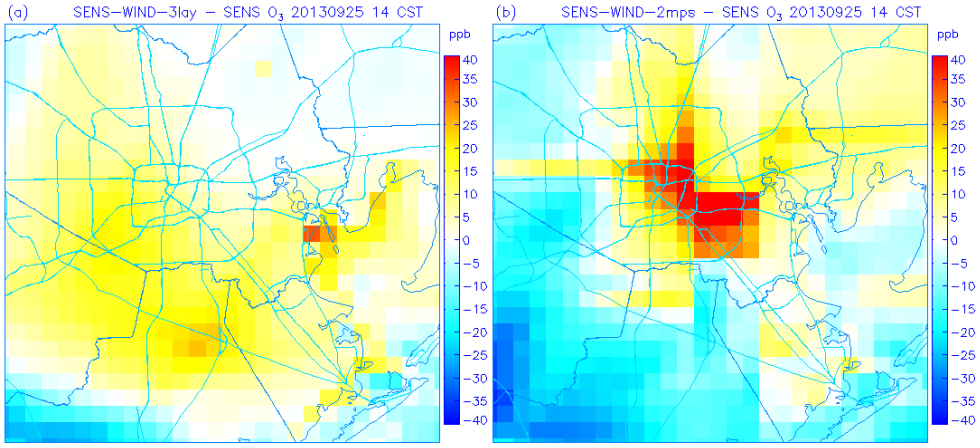

Fig. 3.20. The spatial difference of surface O_3 at 14 CST on 25th September 2013 between different simulations: (a) SENS-WIND-3lay – SENS; (b) SENS-WIND-2mps – SENS. The actual maps are in 104 km × 100 km.

Fig. 3.20 indicated that the simulated O_3 would respond differently if different adjustments were made to the wind fields. In the SENS-WIND case, during daytime (9 to 16 CST) of 25th September 2013, same simple converging wind fields were used, wind speeds were mostly 1 m s^{-1}, and the wind adjustment was applied from the surface to about 2 km height (17 model vertical layers). We performed two additional simulations: (1) SENS-WIND-3lay: the daytime wind adjustment was applied from the surface to about 160 m (3 model vertical layers); other conditions were same as the SENS-WIND case. (2) SENS-WIND-2mps: the daytime domain-wide wind speeds were 2 m s^{-1}; other conditions were same as the SENS-WIND case. As depicted in Fig. 3.20-a, even the wind converged around the industrial region from the surface to 160 m in the SENS-WIND-3lay case, the

O_3 enhancement still moved southwestwards due to likely dominant northwesterly wind within PBL, where the active photochemical O_3 production happened. As shown in Fig. 3.20-b, the increased wind speed in SENS-WIND-2mps case made the O_3 enhancement more concentrated in the center of wind converging zone.

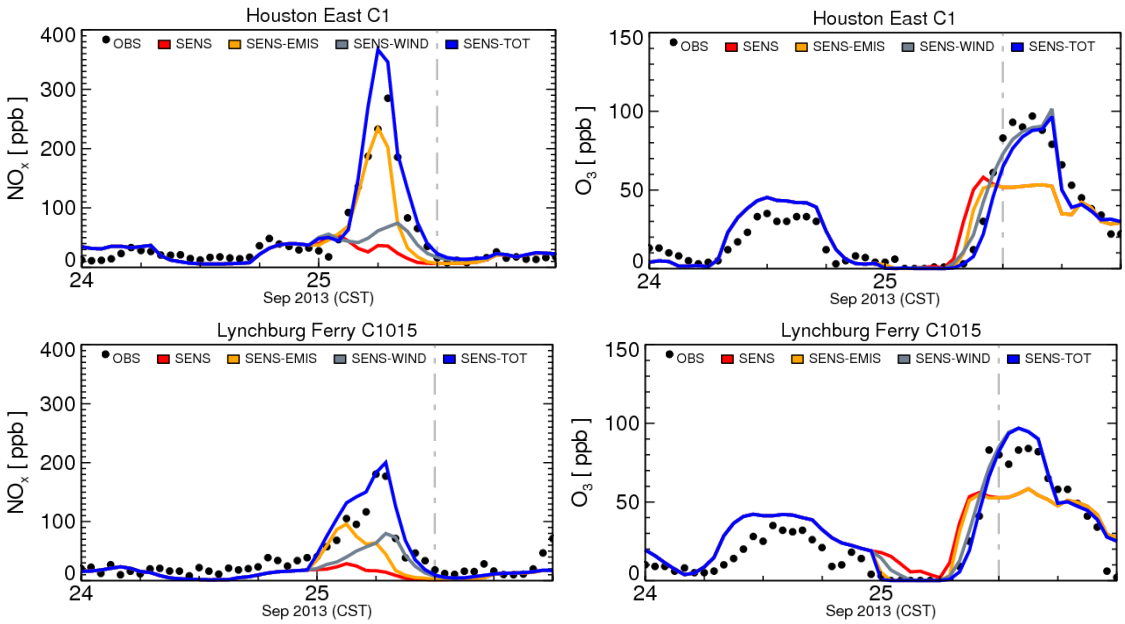

Fig. 3.21. Time series of surface NO_x (left) and O_3 (right) between CAMS surface observations (OBS) and four sensitivity model simulations at two industrial monitoring sites (C1 and C1015). The dashed line in each plot represents 12 CST on 25th September 2013. Time series of O_3 at a few more industrial monitoring sites were plotted in Fig. 3.22.

The improved NO_x simulation results in the SENS-EMIS and SENS-TOT cases and O_3 simulations in the SENS-WIND and SENS-TOT cases over the industrial region are corroborated in the time series comparisons in Fig. 3.21. For instance, the abnormally observed morning time peak NO_x (up to 285 ppb) at the C1 Houston East site was better captured by the SENS-EMIS and SENS-TOT cases. For the SENS-EMIS case, the predicted magnitude of the NO_x peak was around 235 ppb, which was closer to the peak

than any other case. The SENS-TOT case reported over-prediction (~350 ppb), which could be attributed to lowered wind speeds resulting in slower transport.

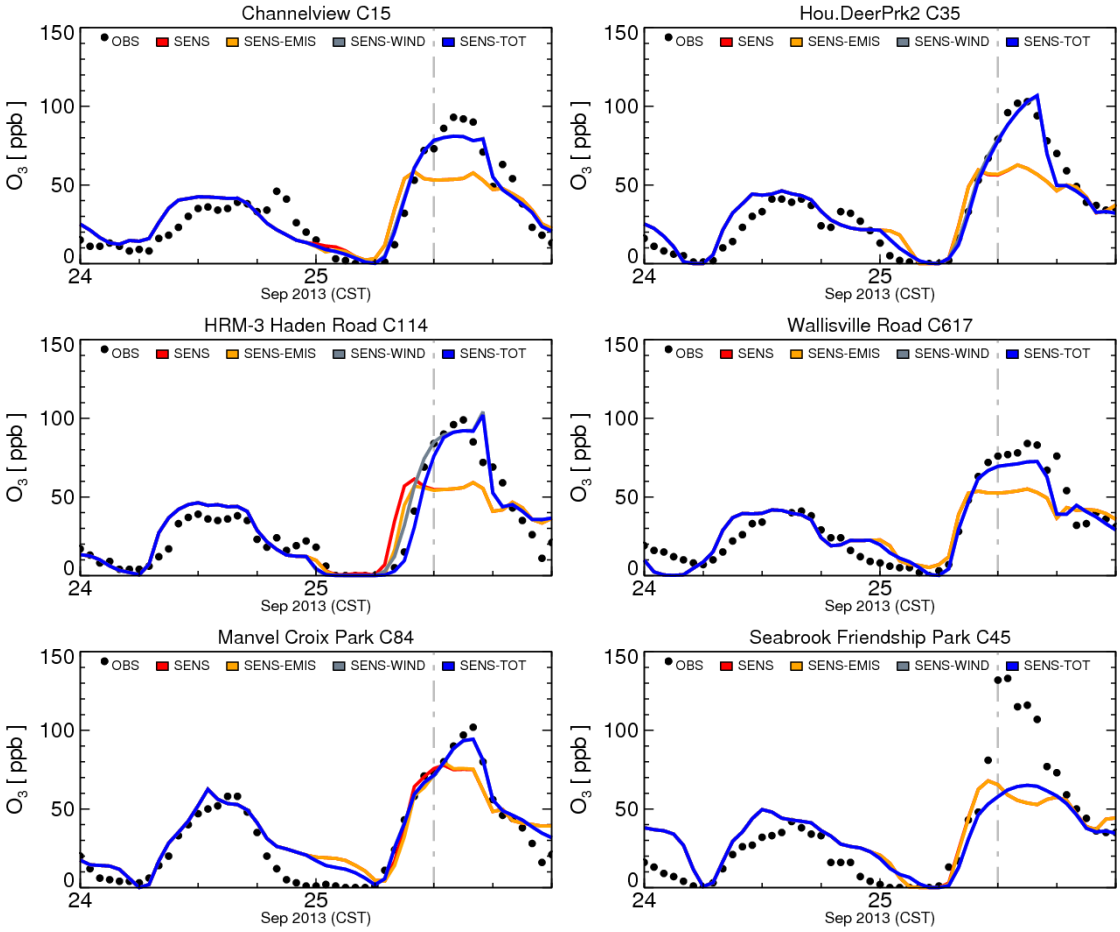

Fig. 3.22. Time series of surface O_3 between CAMS surface observations (OBS) and four model simulations at monitoring sites at the observed peak O_3 area.

Additionally, under-estimations (up to 50 ppb) of high afternoon O_3 were significantly mitigated in the SENS-WIND and SENS-TOT cases. For example, the magnitude of the observed peak O_3 (~100 ppb) on September 25th at the C1 site was under-estimated by 50 ppb for the SENS case, but the simulated peak matched the observations quite closely (negligible error, 7-9 ppb) for the SENS-WIND and SENS-TOT cases. Under-estimations (ranging from about 20 to 50 ppb) of the high O_3 were also mitigated in

these cases over other sites as depicted in Fig. 3.22. These sites were located in the observed peak O_3 area, inside or near the wind converging zone. These results suggest that wind patterns (wind direction especially) could be critically important in determining the location of O_3 hotspots. However, simulated O_3 concentrations still reported pronounced under-estimation at C45 (Fig. 3.22). This could be expected because unlike other monitoring sites, the wind pattern (speed, direction and timing) at C45 during the episode was quite complicated and could not be represented by a simple converging wind. Also, it should be noted that wind adjustments here were imprecise, applying fixed factors to the entire wind field, while actual wind fields were much more complex.

Model-measurement statistics for domain-wide surface NO_x and O_3 for 24^{th} – 25^{th} September 2013 for each simulation case are listed in Table 3.4. Comparing with the SENS case (correlation: 0.48; IOA: 0.55), the performance of the NO_x simulation was largely improved in the SENS-EMIS case (correlation: 0.81; IOA: 0.88). The SENS-TOT case showed the best statistics for NO_x (correlation: 0.84; IOA: 0.90). For O_3 simulations, SENS and SENS-EMIS cases had similar comparison results (correlation: 0.83; IOA: 0.89), SENS-WIND and SENS-TOT showed marginally better performance (correlation: 0.87; IOA: 0.92). Table 3.5 lists the model evaluation statistics for ethylene, isoprene, toluene, and xylenes. For each species, the correlation and IOA exhibited improvements when applying either one of temporally varied SST, emission adjustment, wind adjustment, or all of the above. Results indicate that the CMAQ model is quite sensitive to the changes in emissions and meteorological inputs, and can provide better predictions when using inputs closer to in situ data.

Table 3.4. Evaluation of surface NO_x and O_3 concentrations for the 24th - 25th September 2013.

Species	Case	N	R	IOA	MAE	MB	OM	MM	MM/OM
NO_x	BASE	1328	0.43	0.52	9.8	-3.7	14.4	10.8	0.75
	SENS	1328	0.48	0.55	9.3	-3.7	14.4	10.7	0.74
	SENS-EMIS	1328	0.81	0.88	7.8	-1.9	14.4	12.5	0.87
	SENS-WIND	1328	0.65	0.71	8.5	-2.4	14.4	12.0	0.83
	SENS-TOT	1328	0.84	0.90	8.0	0.8	14.4	15.2	1.05
O_3	BASE	2227	0.82	0.88	11.6	3.6	29.6	33.2	1.12
	SENS	2227	0.83	0.89	11.4	3.5	29.6	33.1	1.12
	SENS-EMIS	2227	0.83	0.89	11.2	3.2	29.6	32.8	1.11
	SENS-WIND	2227	0.87	0.92	10.2	5.3	29.6	34.9	1.18
	SENS-TOT	2227	0.87	0.92	10.1	5.0	29.6	34.6	1.17

Notation: Same as Table 3.1. Units of MAE/MB/OM/MM for NO_x/O_3: ppb.

Table 3.5. Evaluation of surface ethylene, isoprene, toluene and xylenes concentrations for the 24th – 25th September 2013.

Species	Case	N	R	IOA	MAE	MB	OM	MM	MM/OM
Ethylene	BASE	236	0.16	0.28	3.6	0.8	3.1	4.0	1.27
	SENS	236	0.21	0.32	3.5	1.0	3.1	4.1	1.33
	SENS-EMIS	236	0.22	0.34	3.5	1.0	3.1	4.2	1.34
	SENS-WIND	236	0.25	0.41	4.0	1.6	3.1	4.7	1.52
	SENS-TOT	236	0.25	0.42	4.0	1.7	3.1	4.8	1.54
Isoprene	BASE	192	0.14	0.44	0.4	-0.3	0.5	0.2	0.41
	SENS	192	0.20	0.46	0.4	-0.3	0.5	0.2	0.46
	SENS-EMIS	192	0.30	0.50	0.4	-0.2	0.5	0.3	0.53
	SENS-WIND	192	0.21	0.45	0.4	-0.3	0.5	0.2	0.34
	SENS-TOT	192	0.33	0.50	0.4	-0.3	0.5	0.2	0.45
Toluene	BASE	236	0.28	0.52	1.1	0.3	1.2	1.5	1.27
	SENS	236	0.34	0.57	1.1	0.4	1.2	1.6	1.35
	SENS-EMIS	236	0.44	0.65	1.0	0.5	1.2	1.7	1.41
	SENS-WIND	236	0.55	0.64	1.3	0.9	1.2	2.2	1.78
	SENS-TOT	236	0.60	0.65	1.4	1.1	1.2	2.3	1.88
Xylenes	BASE	236	0.40	0.59	0.6	0.0	0.7	0.8	1.05
	SENS	236	0.45	0.64	0.6	0.1	0.7	0.8	1.09
	SENS-EMIS	236	0.56	0.72	0.5	0.1	0.7	0.8	1.15
	SENS-WIND	236	0.53	0.70	0.6	0.3	0.7	1.0	1.35
	SENS-TOT	236	0.60	0.74	0.6	0.3	0.7	1.1	1.44

Notation: Same as Table 3.1. Units of MAE/MB/OM/MM for Ethylene/Isoprene/Toluene/Xylenes: ppb.

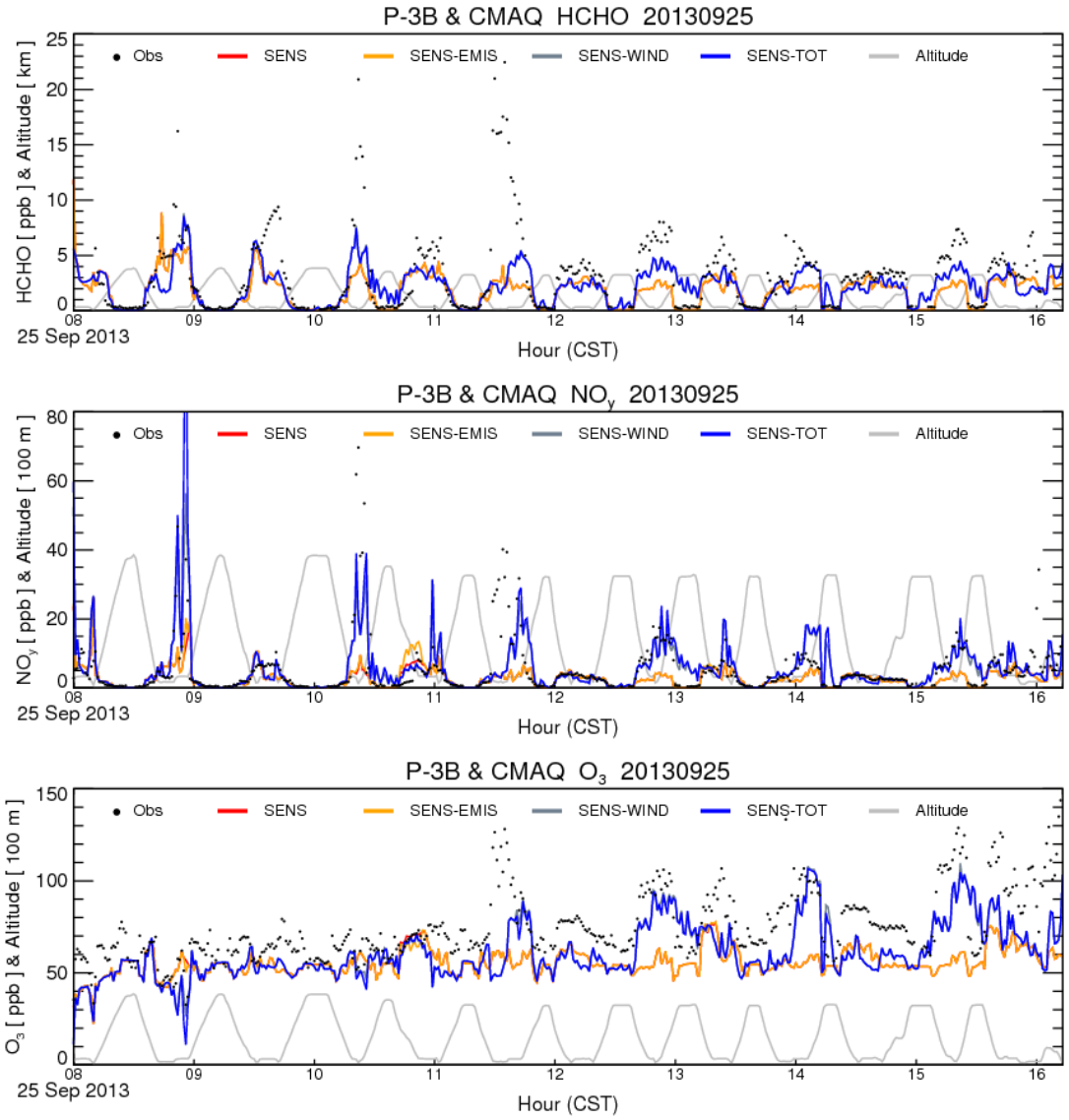

Fig. 3.23. Airborne measured and CMAQ-simulated HCHO, NO_y, and O_3 concentrations along NASA P-3B aircraft track during daytime of 25th September 2013.

As shown in Fig. 3.23, the red line (SENS) coincides with the orange line (SENS-EMIS), and the dark gray line (SENS-WIND) coincides with the blue line (SENS-TOT) for most of the time in each plot, suggesting that emission adjustment might be trivial to the daytime formation of exceptionally high O_3 concentrations. The HCHO and NO_y comparisons portray that the wind adjustment also significantly impacted O_3 precursor

concentrations. The simulations with wind adjustment show improvement in capturing the peak observed values. However, the SENS-WIND case still shows large under-estimations of HCHO and NO_y around 10:20 CST, and HCHO, NO_y, and O_3 during 11:30-12:00 CST. The NASA provides the P3-B Interactive Flight Tracks and Time/Profile Data Plotter (http://www-air.larc.nasa.gov/missions/discover-aq/flight_tracks.tx2013.html). From the interactive map, we can see the observed morning HCHO and NO_y peaks appeared near Ship Channel. They might partly come from industrial emission upsets, besides the impact of sea and bay breeze circulations (Loughner et al., 2015).

3.4. Summary and Discussion

A WRF-SMOKE-CMAQ air quality modeling system was used in conjunction with two WRF runs: a base WRF run and a WRF run initialized with hourly derived NOAA GOES satellite SST values. Modeling runs were conducted to evaluate the impact of high-resolution SST on simulated meteorological fields and surface O_3 over the Greater Houston area on 25th September 2013, the high O_3 episode in the NASA DISCOVER-AQ Texas campaign. The SENS simulation showed the reduced land-sea thermal contrast in the early morning due to 1-2˚C lower SST over water bodies, reducing the simulated wind speed to match observations more closely. Additionally, it slowed dilution and improved the timing of NO_x transport, subsequently leading to a simulated downwind O_3 change of ~5 ppb near the area over land with peak simulated afternoon O_3. However there was still a discrepancy between simulated and observed peak O_3 hotspots, and the model with updated SST failed to capture the magnitude of the O_3 peak at urban and industrial areas.

Excessively high concentrations of NO_x and several highly reactive VOC species were observed in the morning at several surface monitoring stations. These were also underpredicted by the model. Possible episodic flare emissions, dry sunny postfrontal stagnated conditions, and land-bay/sea breeze transitions could be the potential causes of the high O_3 on 25th September 2013. Differences in nocturnal and morning time local wind patterns and precursor conditions between observations and model likely led to the daytime high O_3 discrepancy. Three additional simulations were performed to investigate the sensitivity of O_3 concentrations to emission spikes and wind field changes. Increasing simulated NO_x and VOC emissions using simulated/observed ratios improved the performance of NO_x simulation (correlation and IOA increased from 0.48 and 0.55 to 0.81 and 0.88, respectively), but still showed a discrepancy of peak O_3 locations in the afternoon. Adjusting the wind to represent morning time weak westerly (land breeze pointing to the bay) and the afternoon converging zone significantly mitigated under-estimation (up to 50 ppb) of the high O_3, leading simulated peaked O_3 locations to match better with observed ones. The simulation case with both adjusted emissions and wind fields (SENS-TOT) showed the best statistics for NO_x (correlation: 0.84; IOA: 0.90) and O_3 (correlation: 0.87; IOA: 0.92). These comparisons suggest that wind patterns could be critical in determining the location of the high O_3 peaks and both reasonable emissions and wind fields are required for better O_3 simulations to predict both hotspots and absolute concentrations.

A rapid O_3 increase (up to 60 ppb in 1 hour and 100 ppb in 2-hour for the episode in this study) was observed in the Great Houston area. Despite large annual emission reductions of O_3 precursor species due to successful emissions control policies, continued

optimization of flaring operations to mitigate short-term episodic emission events could potentially contribute to achieving O_3 attainment in the region (Vizuete et al. 2011; Couzo et al. 2013). This study mainly focuses on a single high O_3 episode, impact of high-resolution SST on other episodes with different meteorological characteristics or other months of the year need to be further assessed. Improvement of the model's capability to reproduce small-scale meteorological conditions favoring O_3 production, such as stagnation and wind reversals, is also required.

Chapter 4. Allocating emissions to 4 km and 1 km horizontal spatial resolutions and its impact on simulated NO_x and ozone

4.1. Introduction

In addition to uncertainties in precursor emissions (Choi, 2014; Czader et al., 2015; Pan et al., 2015; Diao et al., 2016a; Souri et al., 2016) and meteorological fields (Ngan et al., 2012; Li et al., 2016; Diao et al., 2016b; Pan et al., 2017a), grid resolution is one of the factors that influence the formation and loss of ground-level O_3 in chemical transport models (Jang et al., 1995a, 1995b; Cohan et al., 2006; Arunachalam et al., 2006), and calculating high-resolution emissions is critical to obtain accurate model predictions of observational data (Valari and Menut, 2008; Roy et al., 2011; Fountoukis et al., 2013).

This study will use a WRF-SMOKE-CMAQ air quality modeling system to investigate the impact of spatial resolutions on model predictions of NO_x and O_3 in Houston, Texas. Most urban regions are typically NO_x-saturated due to significant vehicular traffic. The Houston region, however, has the unique distinction of having both NO_x-saturated and NO_x-limited areas. For example, downtown Houston is NO_x-saturated due to vehicular traffic, while the petrochemical industries typically cluster around the Houston Ship Channel, making it a VOC-rich area and hence NO_x-limited. Therefore the Houston area

[2] This chapter is for "Allocating emissions to 4 km and 1 km horizontal spatial resolutions and its impact on simulated NO_x and O_3 in Houston, TX", published at *Atmospheric Environment* in June 2017 (doi:10.1016/j.atmosenv.2017.06.026). Authors are S. Pan, Y. Choi, A. Roy, and W. Jeon.

is an ideal candidate region to study the impact of changing grid resolution on chemistry and transport of O_3 and its precursors over these different regions (e.g., Choi et al., 2014; Czader et al., 2015). The U.S. EPA's recommended approach will be applied for accurated gridding, which allocates county-based emission inventories to model grid cells using the Geographic Information System (GIS) Shapefiles and other innovative tools, such as U.S. EPA's Spatial Allocator. Using these, two sets of emission files for southeastern Texas in 1 km and 4 km resolutions will be generated. These inputs will be used to compare the effect of grid resolution on the distribution patterns of emissions from several emission source sectors and simulated concentrations of surface NO_x and O_3.

The Integrated Process Rate (IPR) (Byun and Ching, 1999) analysis tool has been used in several modeling studies to quantify the integral contributions of atmospheric physical and chemical processes on model predictions. Previous modeling studies using IPR analyses have indicated chemistry and vertical transport to be the major processes influencing O_3 concentrations in highly polluted areas (Jang et al., 1995a; Li et al., 2012; Jeon et al., 2012). This study will perform IPR analyses at a NO_x-saturated urban location and a NO_x-limited industrial location. Pan et al. (2015) reported that chemistry is the major contribution to daytime O_3 production within the planetary boundary layer (PBL) over urban Houston. In addition to IPR analysis, we will perform the Integrated Reaction Rate (IRR) analyses to evaluate the contributions from various chemical transformations part of the model's chemistry mechanism (Jeffries and Tonnesen, 1994; Jang et al., 1995b; Byun and Ching, 1999). Here, the IRR analyses are utilized to investigate the horizontal and vertical distributions of net O_3 change resulting from chemistry.

This study primarily intends to answer the following questions: (1) What are the similarities and differences in meteorological and emissions fields between the two fine-scale grid resolutions? How do these fields impact the predictions of NO_x and O_3 concentrations? (2) How do major atmospheric processes (e.g. emissions, transport, and chemistry) vary between 1 and 4 km model grids over urban and industrial locations, and how do they affect predictions of O_3 concentrations in these areas? (3) How do the two grid models differ in modeling surface and aloft O_3 concentrations? (4) What resolution provides better model-measurement evaluation? If they have similar reasonable results, what is the benefit of using each of them? Is grid resolution the major cause of O_3 model-observation bias in Houston?

4.2. Methodology

4.2.1. Model set-up and observational data

The CMAQ model version 5.0.2 with the CB05 chemical mechanism and AERO6 module, WRF model version 3.7, and SMOKE version 3.6 with NEI-2011 were used. Firstly, we defined the simulation domains covering southeast Texas with same horizontal coverage and vertical structure but different horizontal grid resolutions (1 km and 4 km), as shown in Table 4.1 and Fig. 4.1. We ran the WRF model using both 1 km and 4 km horizontal grid spacing, as well as with the same WRF physics configurations. Next, we prepared two sets of emissions (in 1 and 4 km) using the approach recommended by the U.S. EPA. Two CMAQ simulation cases were considered: (1) 1KM (called hereafter) – meteorology and emissions prepared in 1 km grid spacing; (2) 4KM (called hereafter) –

meteorology and emissions prepared in 4 km grid spacing. Both cases used same initial and boundary conditions, obtained from the AQF-UH 12 km CONUS domain (the larger domains in Fig. 4.1). The TCEQ's CAMS network NO_x and O_3 measurements and the NASA P-3B aircraft O_3, NO_y, and isoprene measurements were used to evaluate model performance.

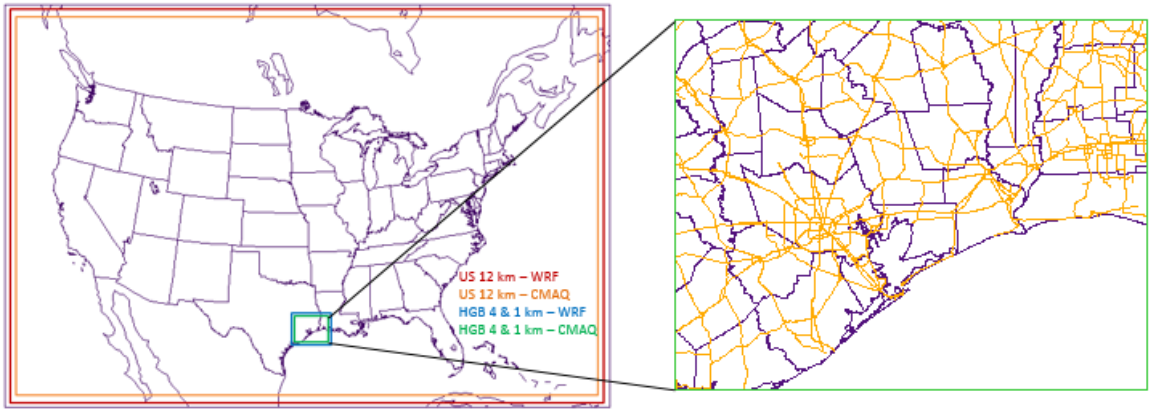

Fig. 4.1. Horizontal domains of WRF and CMAQ at different grid resolution; the HGB 4 and 1 km are used in this study while the US 12 km is used to provide boundary conditions. The US 12 km domain has 459 × 299 grids. For the zoomed-in plot on the right, roadways are represented in orange and county boundaries in purple.

Table 4.1. The modeling domain information for 1KM and 4KM cases.

Case	Horizontal resolution	East-west direction	North-south direction	Vertical layers
4KM	4 km	84 grids	66 grids	27 layers
1KM	1 km	336 grids	264 grids	27 layers

4.2.2. Preparation of emissions for different grid resolutions

Fig. 4.2 depicts a schematic of the emissions processing system for a given grid resolution. Anthropogenic emissions inventories included point, area, non-road, and mobile sources. These were reported annually, monthly and in some cases, daily. Point sources were reported with latitude and longitude data, other sources were county-level.

The inventories included a large suite of pollutants, such as CO, NO_x, VOC, PM_{10}, $PM_{2.5}$, and SO_2. The SMOKE model performs several processes, including temporal allocation to transform annual or monthly inventory data to hourly data, spatial allocation to distribute point or county-level emissions to model grid cells, chemical speciation to map the emissions to "model species" used in the CB05 photochemical mechanism, and plume rise estimation to allocate the point source emissions vertically. The SMOKE model processed each emission source separately and then merged them to create gridded hourly CMAQ model-ready 3-D emission input files. Among all the processes, the spatial allocation was domain-specific and most relevant to grid resolution.

A set of ancillary files called spatial surrogates were used in the spatial allocation of emissions. These surrogates consist of values between 0 and 1.0 that specify the fraction of the county emissions that should be allocated to each grid cell that intersects the county for a given source/set of sources. There are more than 100 spatial surrogates available. They were classified into several categories, such as population and housing, home heating, road and rail, land-use and land cover, building square footage, the number of gas stations/diesel terminals and shipping, and other industrial and commercial activities (Adelman, 2015). They can be generated by the Surrogate Tool of the Spatial Allocator (SA) (https://www.cmascenter.org/sa-tools/). A list of GIS Shapefiles, having finer resolutions than county data, was used as input of SA to generate spatial surrogates. The GIS Shapefiles were mostly circa 2010-based data, including 2010 U.S. Census data at the block group level, 2010 American Community Survey Data for heating fuels, 2010 TIGER/Line data for railroads and roads, the 2006 National Land Cover Database, 2011

gas station and dry cleaner data, and the 2012 National Transportation Atlas Data for rail-lines, ports and navigable waterways (U.S. EPA, 2015a).

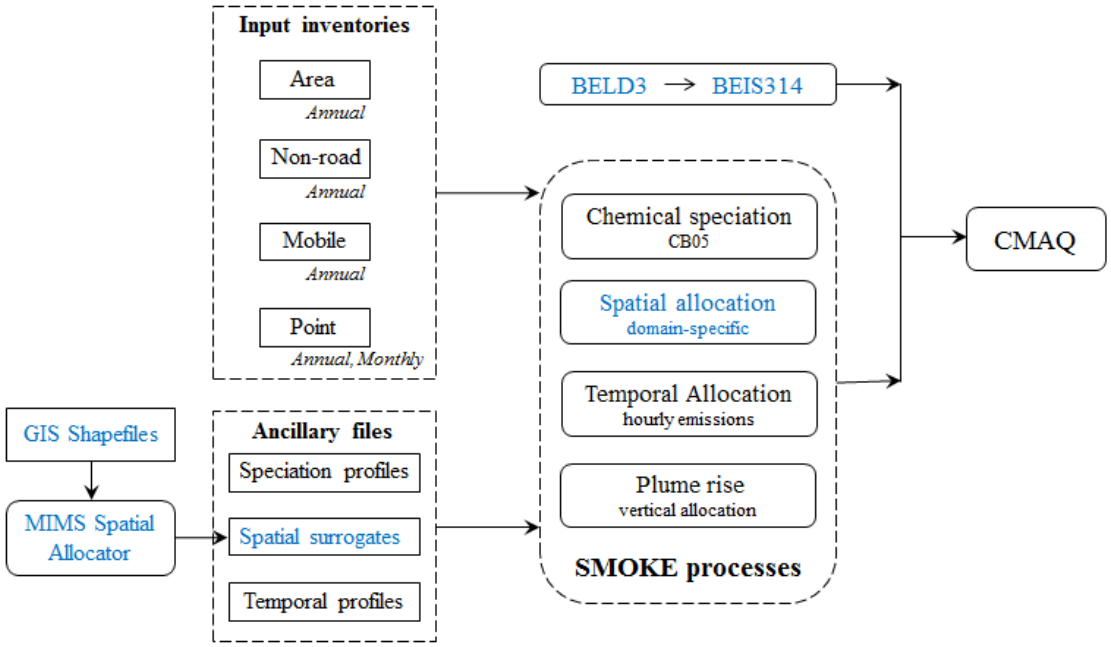

Fig. 4.2. Schematic of the SMOKE emission processing system. The text in blue color represents the files or processes related to spatial resolution and modified in this study.

Gridded hourly biogenic emissions were estimated using the U.S. EPA's Biogenic Emission Inventory System, version 3.14 (BEIS314) (Pouliot and Pierce, 2009). The BEIS314 uses vegetation speciation data from the Biogenic Emissions Landuse Database version 3 (BELD3), which provides data on 230 land-use and vegetation classes at 1 km resolution over the contiguous United States. The BELD3 data are based on combined county-level U.S. Department of Agriculture (USDA) data and U.S. Forest Service (USFS) Forest Inventory and Analysis (FIA) vegetation species data. The Vector Tool of Spatial Allocator was used to prepare domain-specific BELD3 data.

4.3. Results

4.3.1. Basic meteorological model performance evaluation

Domain-wide time series comparisons of surface temperature, wind speed and direction between CAMS observations and simulation results for the month of September 2013 are presented in Fig. 4.3. Both 1KM and 4KM cases show very similar performance. The results are also similar to the 4 km simulation of Li et al. (2016) and Pan et al. (2017a). Evaluation statistics such as correlation, index of agreement (IOA), and mean bias (MB) between CAMS observations and the two simulations are listed in Table 4.2. No significant differences were reported between the two simulations for any of the meteorological parameters.

Table 4.2. Model-measurement comparison of meteorological parameters for September 2013.

Variable	Case	N	R	IOA	MAE	MB	OM	MM	MM/OM
Temperature	4KM	41058	0.85	0.90	1.6	1.0	27.4	28.4	1.04
	1KM	41058	0.85	0.88	1.7	1.3	27.4	28.7	1.05
Wind Speed	4KM	43246	0.70	0.76	1.3	1.0	2.5	3.5	1.40
	1KM	43246	0.69	0.75	1.3	1.0	2.5	3.5	1.42
Wind Direction	4KM	43246	0.51	0.71	43.1	7.7	127.5	135.2	1.06
	1KM	43246	0.50	0.71	44.1	9.1	127.5	136.5	1.07

Notation: N – Number of data points; R– Correlation; IOA – Index of Agreement; MAE – Mean Absolute Error; MB – Mean Bias; OM – Observed Mean; MM – Model Mean; MM/OM – Model Mean divided by Observed Mean. Units of MAE/MB/OM/MM for Temperature: ˚C, Wind Speed: m/s, Wind Direction: degree.

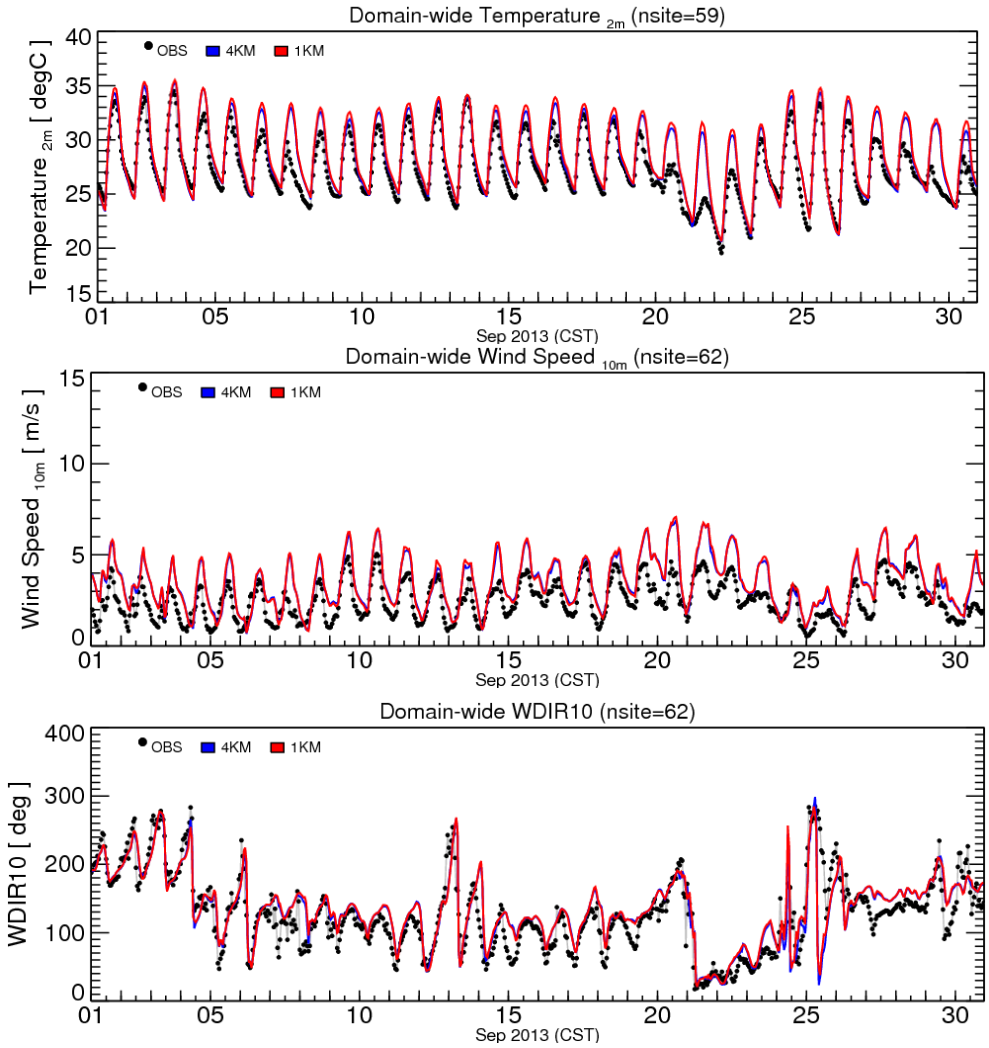

Fig. 4.3. Time series of domain-wide 2-m temperature, wind speed, and wind direction comparison between 4KM and 1KM cases and TCEQ CAMS surface observations (OBS).

4.3.2. Spatial distribution comparisons

4.3.2.1. Meteorological factors

Simulated surface temperatures in 1KM case reflected clearer features of the Galveston Bay coastline (Fig. 4.4 and 5.5). Also, there were a few small-scale cooler regions in 1KM case. These small-scale cooler regions coincided with significant lower PBL (Fig. 4.5-c), more detailed cloud (Fig. 4.5-e), and diverging surface winds (Fig. 4.5-g

and 5.6). These differences could be attributed to varying cloud cover with grid resolution. For example, the cloud fraction for the 1KM case was much more localized.

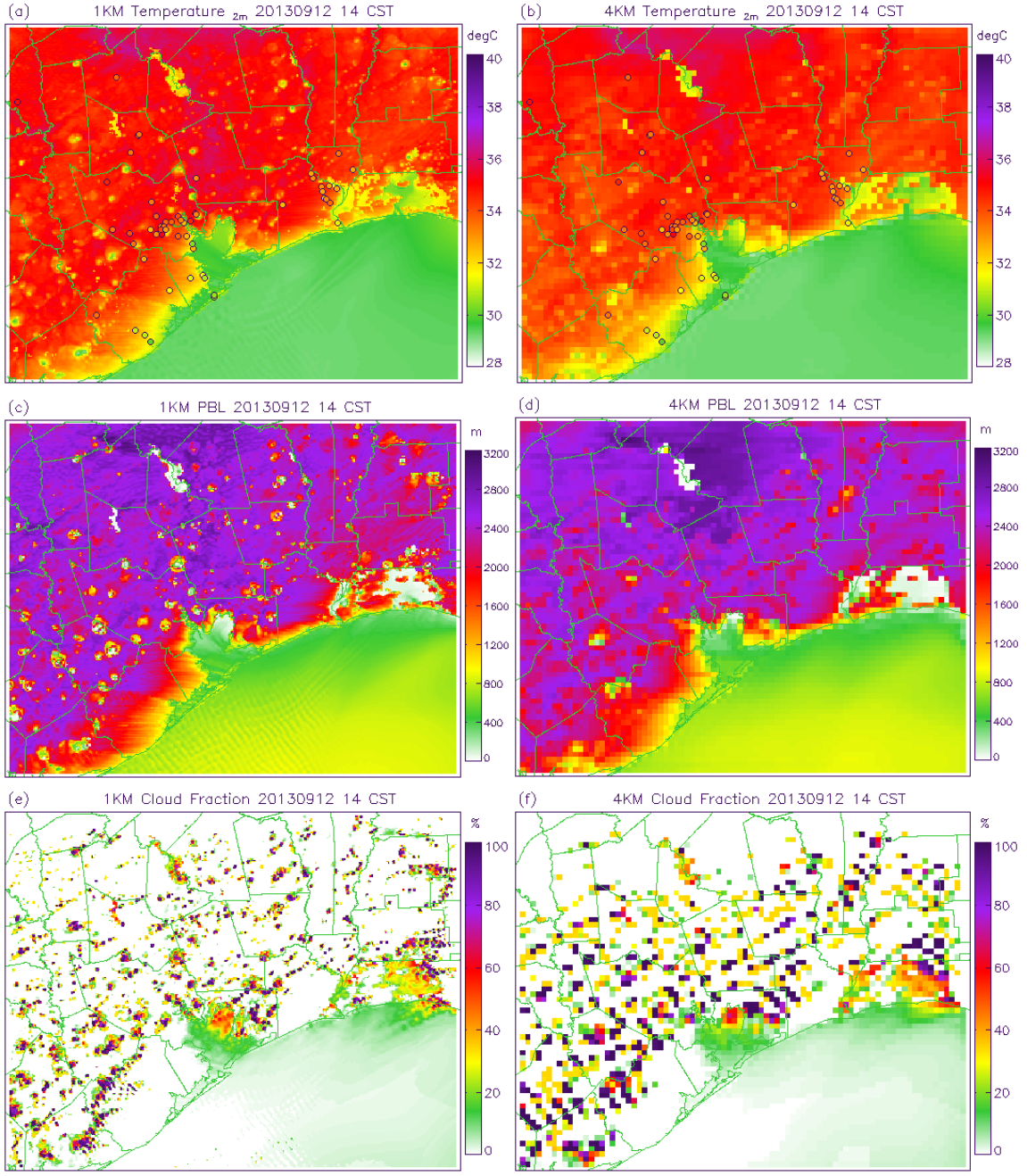

Fig. 4.4. Spatial distributions of surface meteorological fields at 14 CST on 12th September 2013: (a) 1KM with CAMS 2-m temperature; (b) 4KM with CAMS 2-m temperature ; (c) 1KM PBL; (d) 4KM PBL; (e) 1KM cloud fraction; (f) 4KM cloud fraction. The actual maps are in 336 km × 264 km.

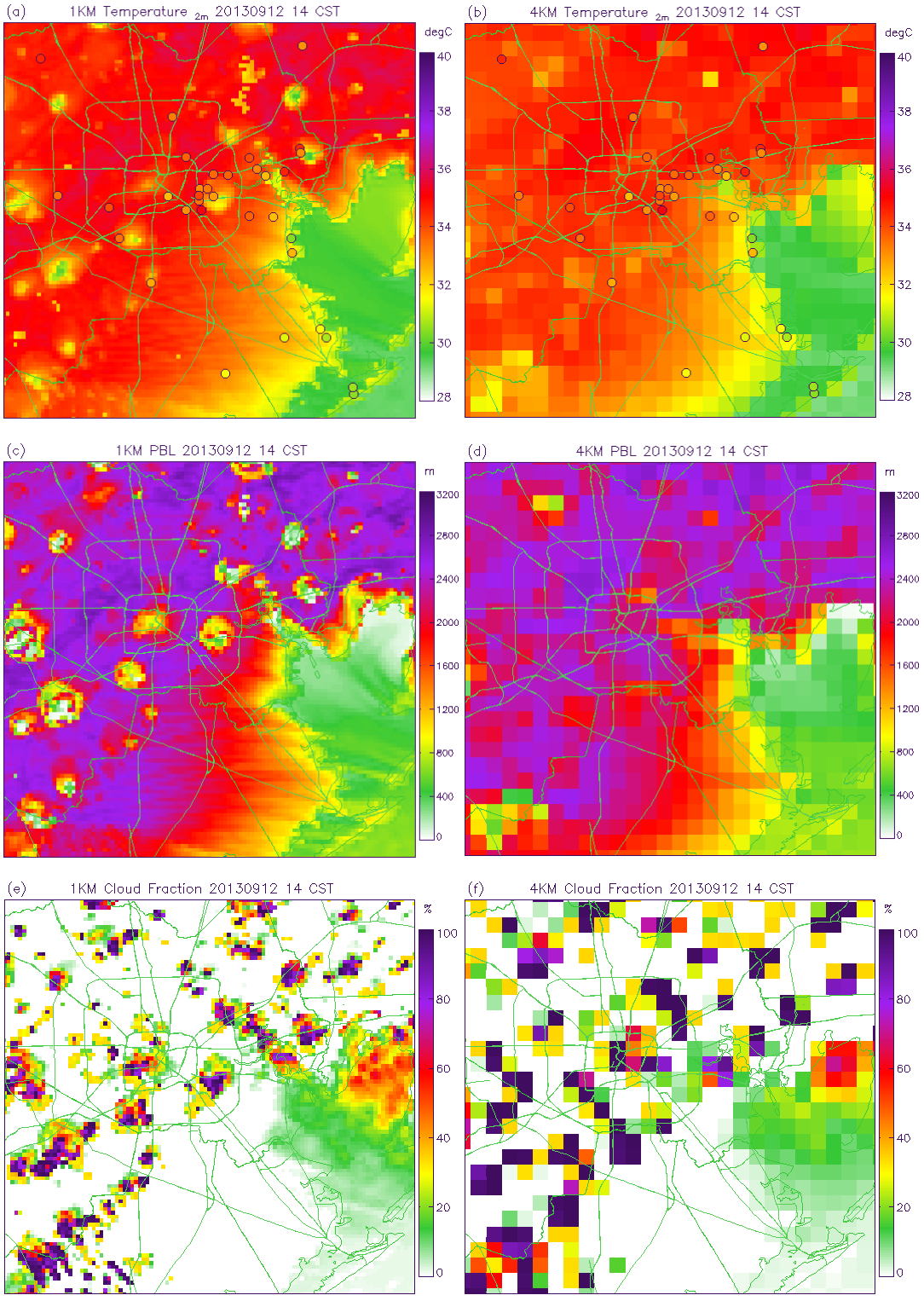

Fig. 4.5. Spatial distributions of surface meteorological fields at 14 CST on 12th September 2013: (a) 1KM with CAMS 2-m temperature; (b) 4KM with CAMS 2-m temperature ; (c) 1KM PBL; (d) 4KM PBL; (e) 1KM cloud fraction; (f) 4KM cloud

fraction; (g) 1KM 10-m wind (purple arrow), with CAMS wind (red arrow); (h) 4KM 10-m wind with CAMS wind. These are the distributions in the urban-industrial-bay areas. The actual maps are in 104 km × 100 km.

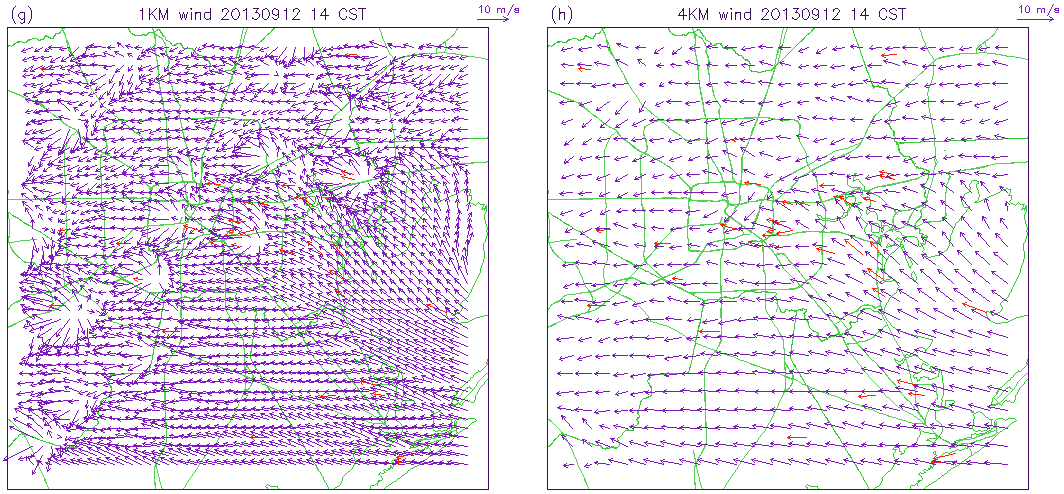

Fig. 4.5. Continued. Note: in panel (g), the 1KM modeled wind vectors were plotted at 2 km intervals to improve legibility.

The plots in Fig. 4.7 indicate the simulated surface temperature was similar during most of the time between 1KM and 4KM cases. However, certain subtle differences are predicted. For instance, at site C1017, the simulated temperature for 1KM case fell sharply and then rose during the afternoon of 12th September 2013. It dropped about 3 ºC and then moved upward in a very short period (2-3 hours). Similar phenomena with smaller magnitude also occurred in other days or monitoring sites. These may be attributed to uncertainties in simulations of cloud formation and movement in different grid resolutions.

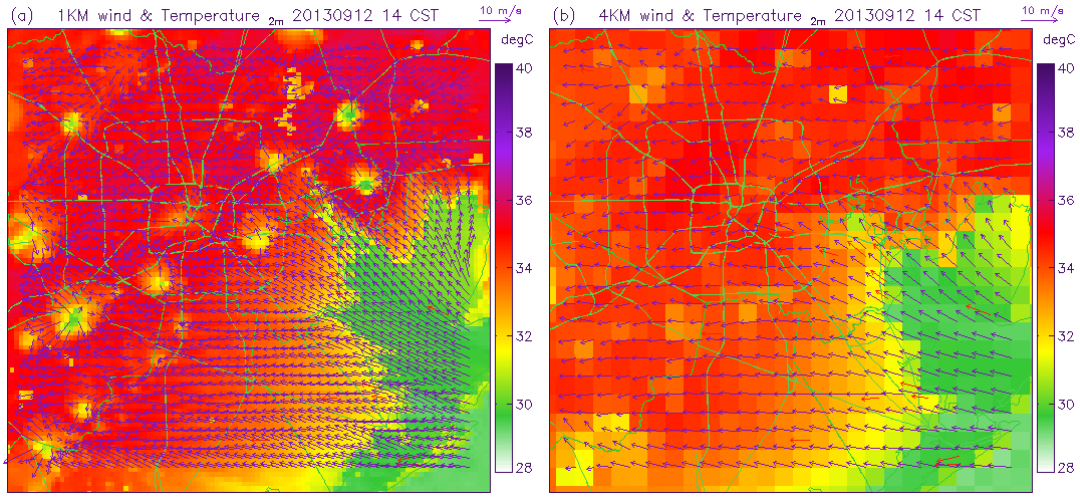

Fig. 4.6. Spatial distributions of simulated 2-m temperature and 10-m wind at 14 CST on 12th September 2013. The small-scale cooler regions exactly coincided with the point of diverging winds in 1KM case (left panel). The actual maps are in 104 km × 100 km.

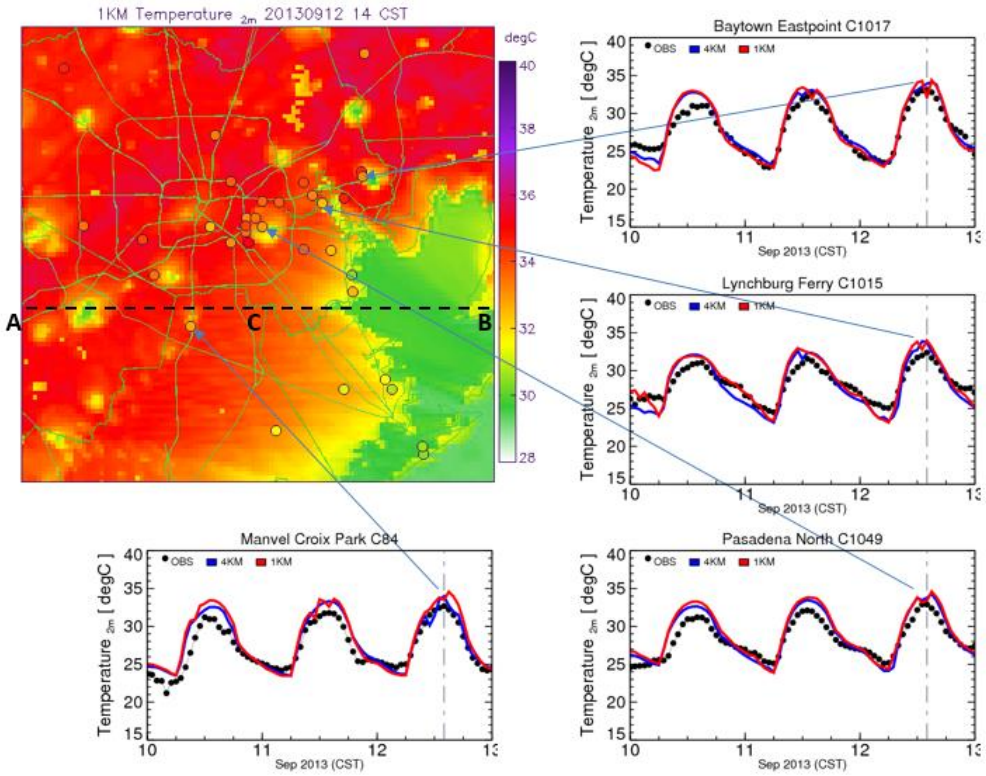

Fig. 4.7. Time series of 2-m temperature at monitoring sites which are located near the small-scale cooler regions in 1KM case. The gray dashed vertical line in each time series represents 14 CST on 12th September 2013.

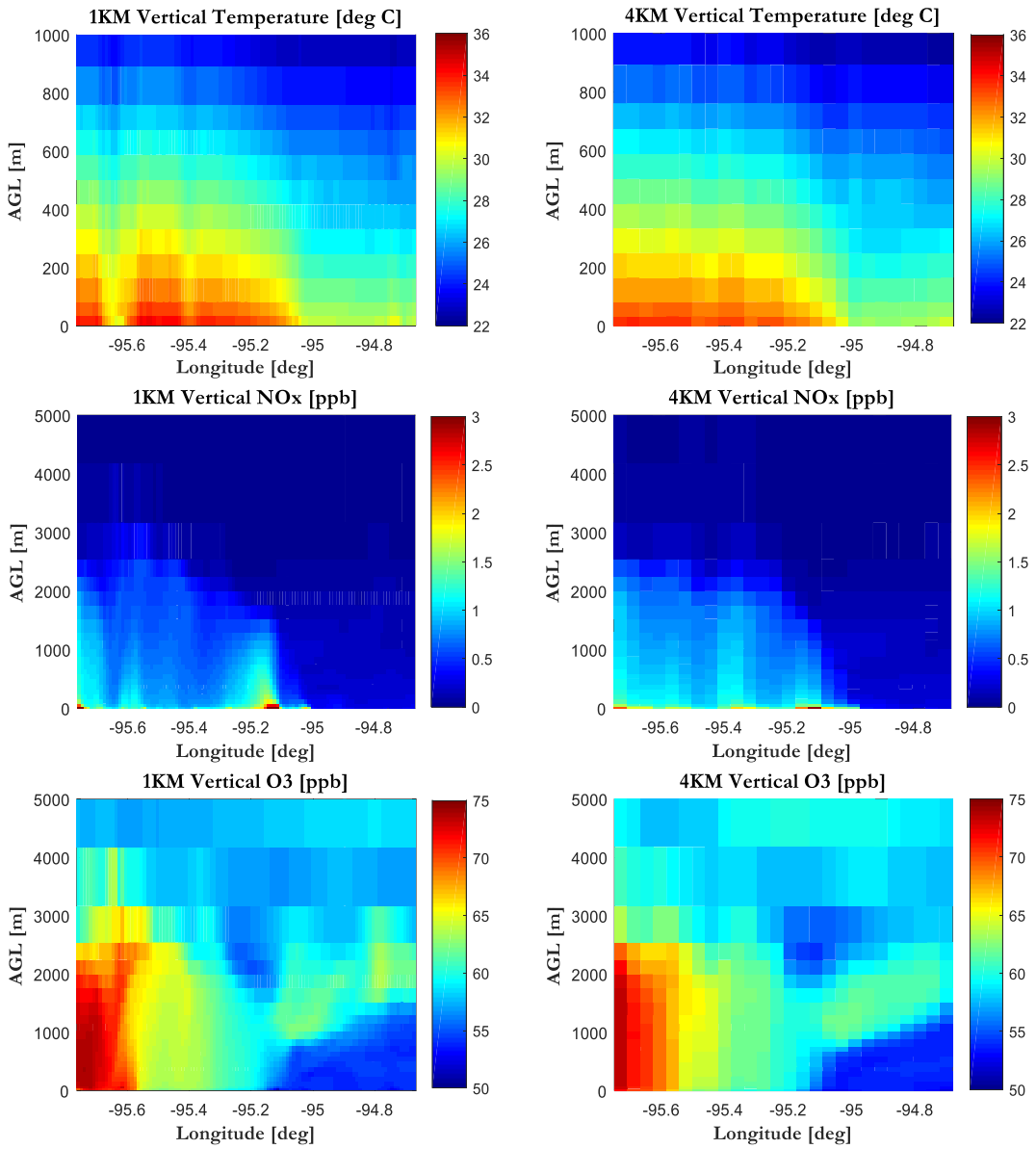

Fig. 4.8. Vertical cross section of temperature, NO_x and O_3 in 1KM and 4KM cases at 14 CST on 12th September 2013 along the dashed line "AB" in the spatial plot of Fig. 4.7.

In Fig. 4.8, the small-scale cooler region in 1KM case extended from the surface up to a height of ~900 m. For chemical species in both cases, the vertical profiles of high aloft NO_x concentrations corresponded with source regions at the surface. High O_3 concentrations extended from surface to a height of ~2.5 km in the west part of the domain under the impact of westward bay breeze. The differences in NO_x and O_3 between two

cases could be attributed to both meteorology and emissions. The vertical wind plots in Fig. 4.9 indicate the small-scale downdraft in 1KM case was not evident in 4KM case. These small-scale differences in meteorological factors may have localized impact on the concentrations of air pollutants.

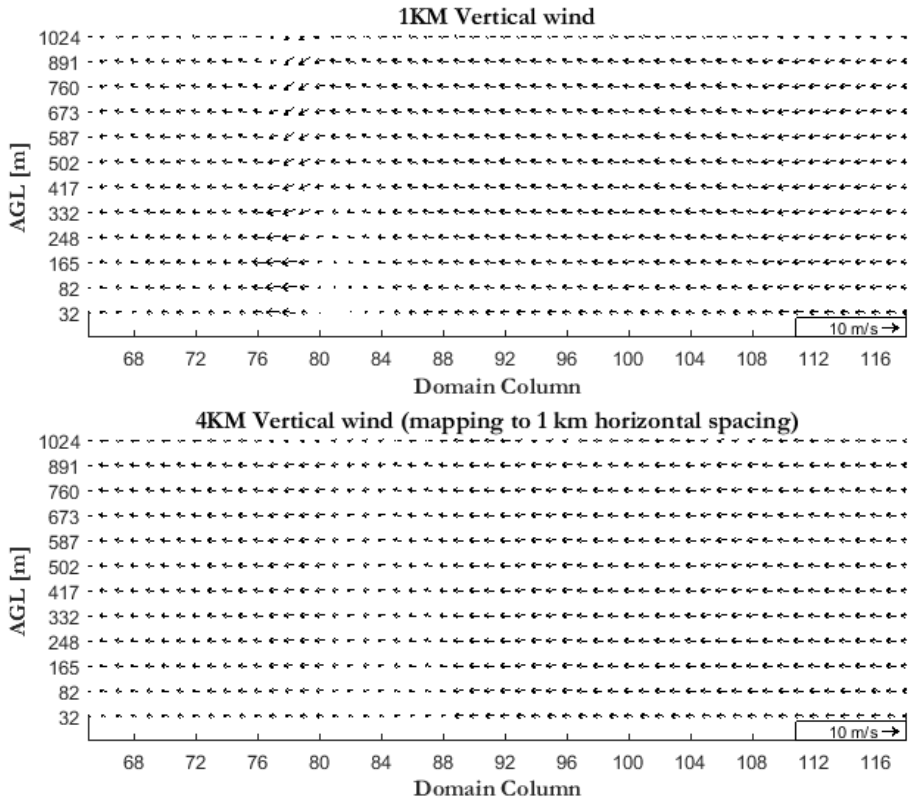

Fig. 4.9. Vertical cross section of the wind in 1KM and 4KM cases at 14 CST on 12th September 2013 along the dashed line "AC" in the spatial plot of Fig. 4.7. The small-scale downdraft in the 1KM case was not shown in the 4KM case.

4.3.2.2. Emission comparisons using nitric oxide (NO) as an example

The Houston metropolitan area has a unique pollutant mix from significant anthropogenic emission sources such as large clusters of petrochemical and chemical manufacturing facilities, motor vehicles and marine vessels (Czader et al., 2008; Cheng et al., 2008; Olaguer et al., 2009), and biogenic sources such as vegetation (Byun et al., 2005;

Cheng and Byun, 2008). The NO emissions plotted in Fig. 4.10 and 5.11 are used as an example to demonstrate how emission distribution patterns changed between 1KM and 4KM cases. These emissions represented in these plots include several emissions source sectors. Each major source category (e.g., area, mobile, or point) also included several specific sectors using different temporal and spatial allocation profiles. In Fig. 4.10, the 'rateperdistance' represents on-road mobile sources and emission processes (e.g., running and crankcase exhaust for NO_x emissions). Both cases (Fig. 4.10-a, 1KM case and Fig. 4.10-b, 4KM case) highlight the roadway networks inside the simulation domain. The plots indicate clearer features for on-roadway emissions in the 1 km case than the 4 km one. The 'nonroad' vehicles sector is treated an area source, which includes lawn, garden and construction equipment, recreational marine craft, portable industrial, commercial, and agricultural engines (U.S. EPA, 2015b). For our simulation domain, these emissions were predominantly concentrated in the urban area, and more detailed emission features were exhibited in 1KM case (Fig. 4.10-c) than 4KM case (Fig. 4.10-d). The area and mobile sources were assigned to the model surface layer and point sources were allocated vertically. The 'ptnonipm' sector in Fig. 4.11 represents point sources other than Electric Generating Units. The spatial allocation of point sources was very straightforward since they were reported along with their latitude and longitude coordinates. Hence, the 'ptnonipm' emissions were apportioned to the corresponding grid cells intersecting the coordinates. Both 1KM and 4KM cases reported exactly same numbers of emission point sources. In the Ship Channel industrial region, NO emissions from chemical plants and petroleum refineries, are lower in the model surface layer (Fig. 4.11-a and 5.11-b) than the second layer (Fig. 4.11-c and 5.11-d). Fig. 4.12 depicts emission comparisons from

biogenic sources (NO emissions from soil). To summarize, spatial allocation of emissions to a finer grid allows for the consideration of detailed emission features. However, the temporal allocation remained invariant with grid size. Since fixed monthly, the day of the week, and hourly temporal profiles were used, the emission distributions in both cases at other time of the day or at other days were similar to those in Fig. 4.10 and Fig. 4.11, but with different magnitude.

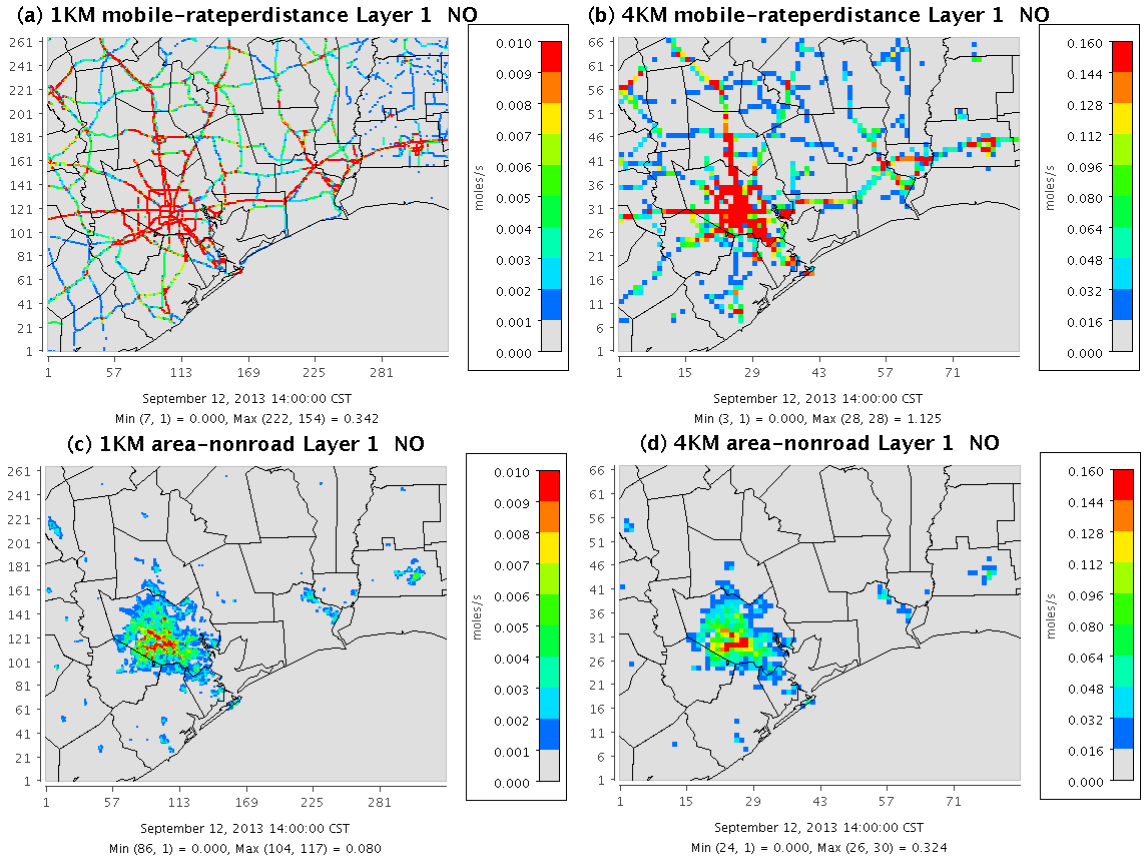

Fig. 4.10. Spatial comparisons of NO emissions (from mobile sources) for 1KM and 4KM simulation cases at 14 CST on 12th September 2013. The numerals on the bottom and left side of the maps are the numbers of grid cells.

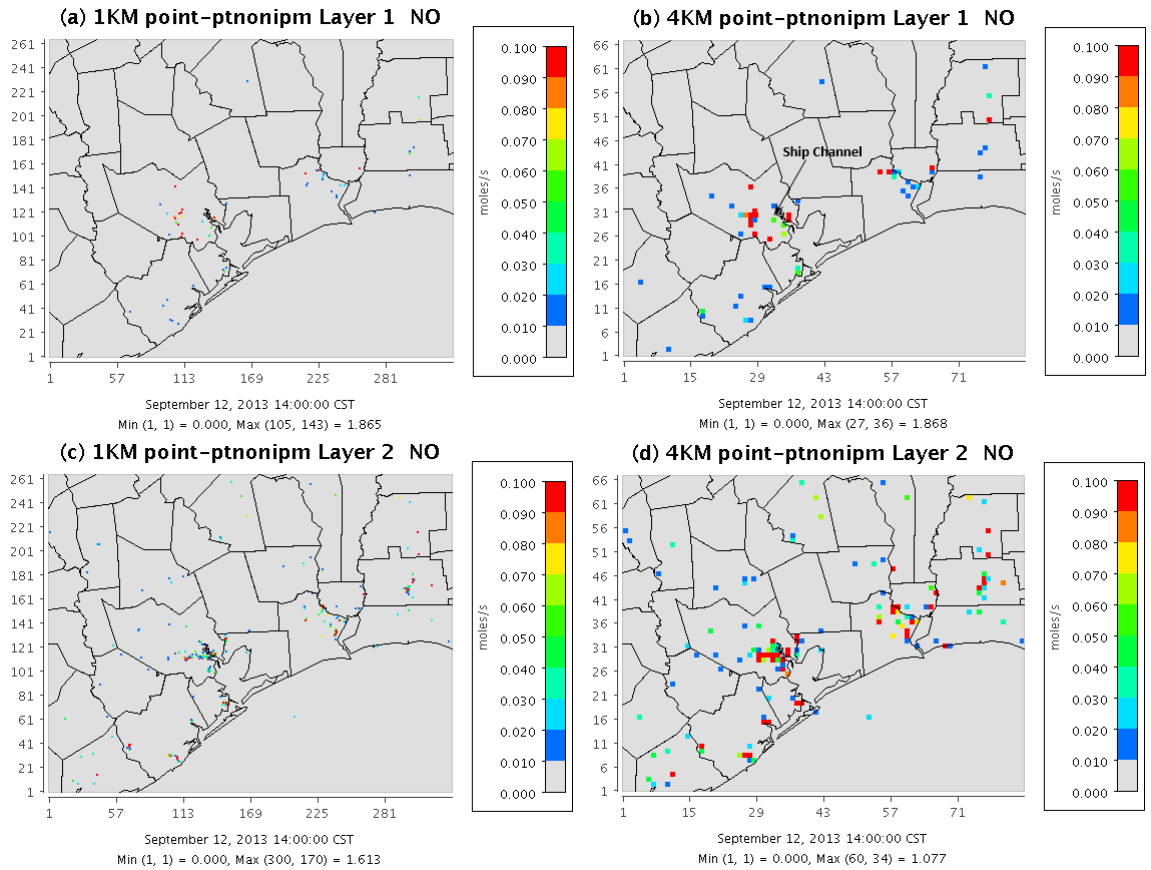

Fig. 4.11. Spatial comparisons of NO emissions (from non-EGU point source) for 1KM and 4KM simulations at 14 CST on 12th September 2013. The full layer height for the 1st layer and 2nd layer are 32 m and 82 m, respectively. The numerals on the bottom and left side of the maps are the numbers of grid cells.

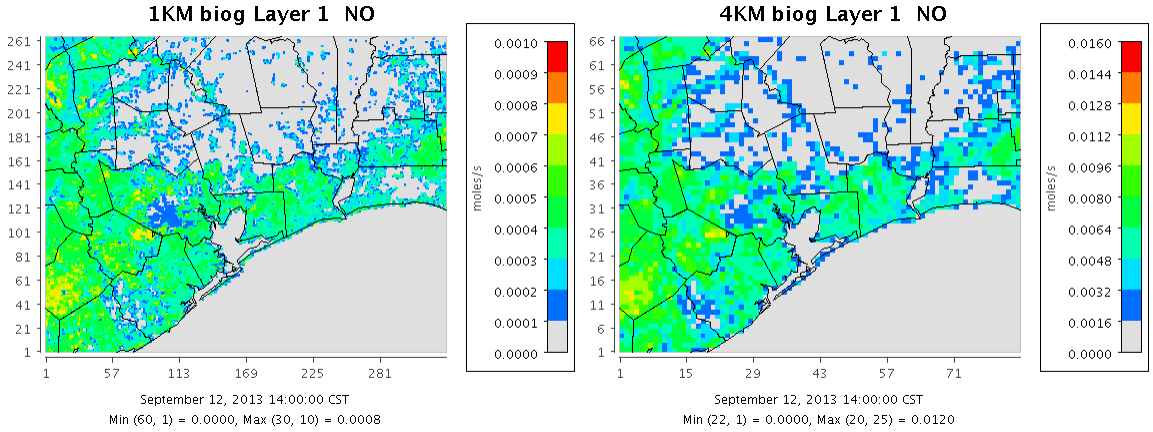

Fig. 4.12. Spatial comparisons of NO emissions (from biogenic sources: soil NO) between 1KM and 4KM simulations at 14 CST on 12th September 2013. The numerals on the bottom and left side of the maps are the numbers of grid cells.

4.3.2.3. Concentration comparisons

At heavily polluted areas such as those around an industrial power plant, coarse model grids typically allocate the high emissions uniformly across the grid cell, creating a physically inconsistent high emission density not just around the source but also its immediate surroundings (Tan et al., 2015). This density can be mitigated using a finer resolution, which allocates emissions only to the source grid cell but not those surrounding it. Hence, the spatial allocation of emissions to model grids at different resolutions could potentially result in a difference in predicted concentrations of pollutants. As depicted in Fig. 4.13, the CMAQ-simulated NO_x spatial distributions were significantly different for 1 km and 4 km resolutions. In 1KM case, high simulated NO_x concentrations coincided with highways, and large gradients of the simulated values were shown at airports and industrial point sources due to the short atmospheric lifetime of NO_x (Fig. 4.13-a). The 4KM case also showed high simulated NO_x concentrations at urban and industrial regions (Fig. 4.13-b) but lacked the detailed granularity of 1KM case. The magnitudes of peak simulated NO_x in the 1KM case were also higher than the 4KM case. Simulated surface O_3 concentrations were relatively low at grid cells with high simulated peak NO_x concentrations in both cases. These grid cells could be represented as NO_x-saturated areas. Simulated O_3 hotspot patterns appeared quite different for 1KM and 4KM cases. For example, in 1KM case, areas having O_3 concentrations greater 75 ppb appeared to be quite uniform outside the highway network, while they seemed to be clustered in one spot for the 4KM case. The patterns suggest that O_3 was formed in the outflow from the NO_x-saturated highway network (in the urban region) into a NO_x-limited area. Similar phenomena have been predicted by Pan et al.

(2015). The transport was due to northeasterly and southeasterly wind patterns merging near the highway. The results suggest the 1 km resolution is able to distinctly capture the formation of O_3 in the highway outflow, which the 4 km case is unable to reproduce. The difference in the spatial distribution of hotspots in 4KM and 1KM cases could be possibly due to a combination of the difference in the distribution of emissions and meteorological fields. Grid resolution impacts on low simulated HO_2 are similar to that on simulated peak NO_x. A high NO_x environment promotes higher reaction of HO_2 with NO (Czader et al., 2013), leading to relatively lower HO_2 concentrations over urban and industrial regions, especially along highways and at industrial facilities (Fig. 4.13-e and 5.13-f). To summarize, the results demonstrate that varying grid resolutions will change spatial patterns of pollutants around heavy polluted areas.

In addition to emissions, transport processes can also play an important role in the difference in concentrations due to changing grid resolutions. Fig. 4.14 plots the surface wind fields superimposed over evening time NO_x concentrations. The results indicate southeasterly sea-breezes blew from the Gulf of Mexico into the city during the afternoon to evening hours. The wind patterns for the two cases were very similar during the time. However, NO_x hotspots showed different spatial patterns between the two cases. The NO_x hotspots appeared as narrow plumes in the 1KM case; while more downwind areas were impacted in 4KM case. This is because 4KM case allocated larger emissions over a bigger grid cell, hence the effects of transport are also predicted over larger regions. In other words, the gradients are steeper for 1KM case as opposed to the 4KM case.

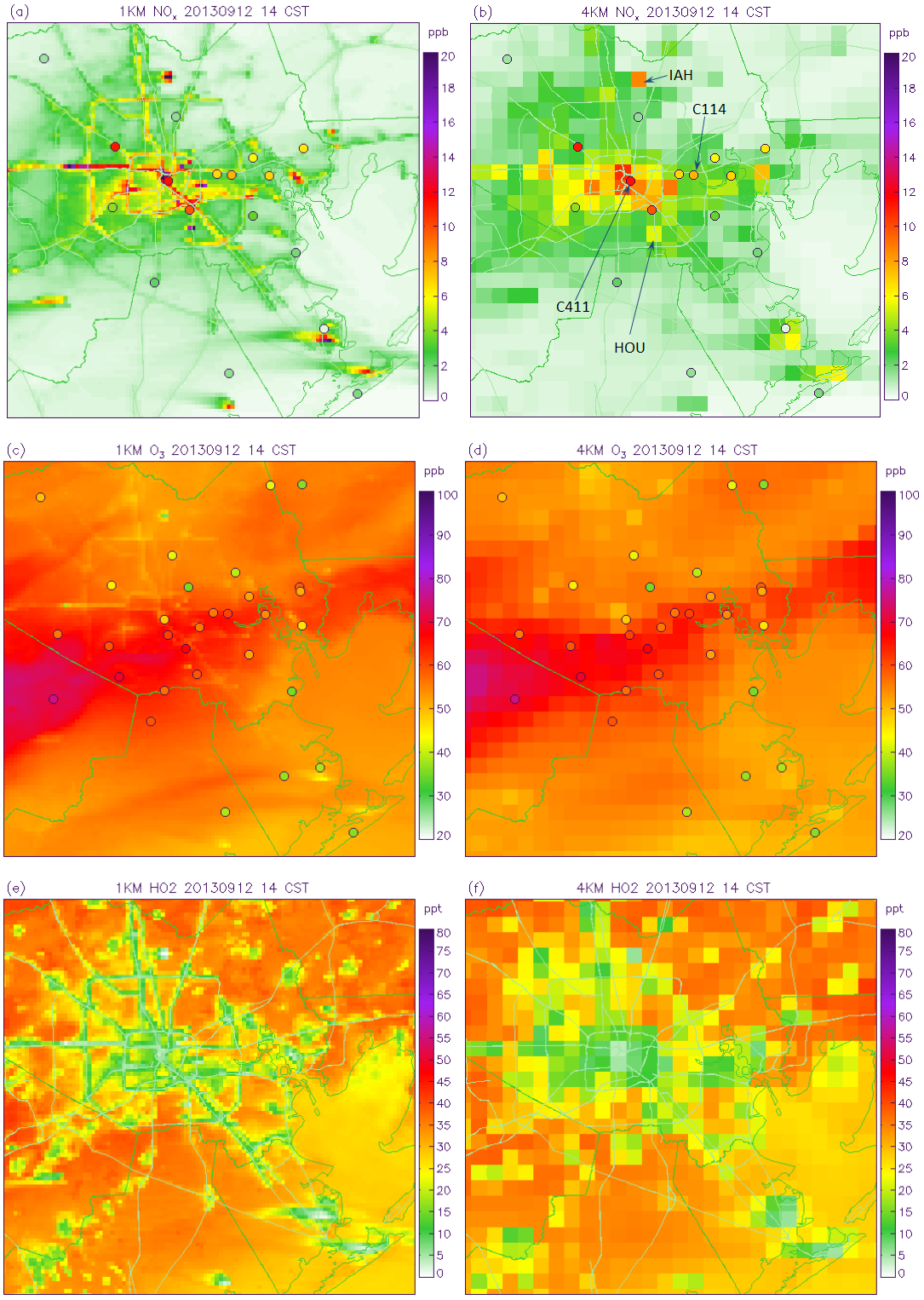

Fig. 4.13. Spatial comparisons of surface NO_x, O_3 and HO_2 concentrations at different grid resolutions at 14 CST on 12th September 2013: (a) 1KM with CAMS NO_x; (b) 4KM with CAMS NO_x; (c) 1KM with CAMS O_3; (d) 4KM with CAMS O_3; (e) 1KM HO_2; (f) 4KM

HO_2. In panel (b), IAH and HOU are airports, C411 is an urban monitoring site, and C114 is an industrial site. The actual maps are in 104 km × 100 km.

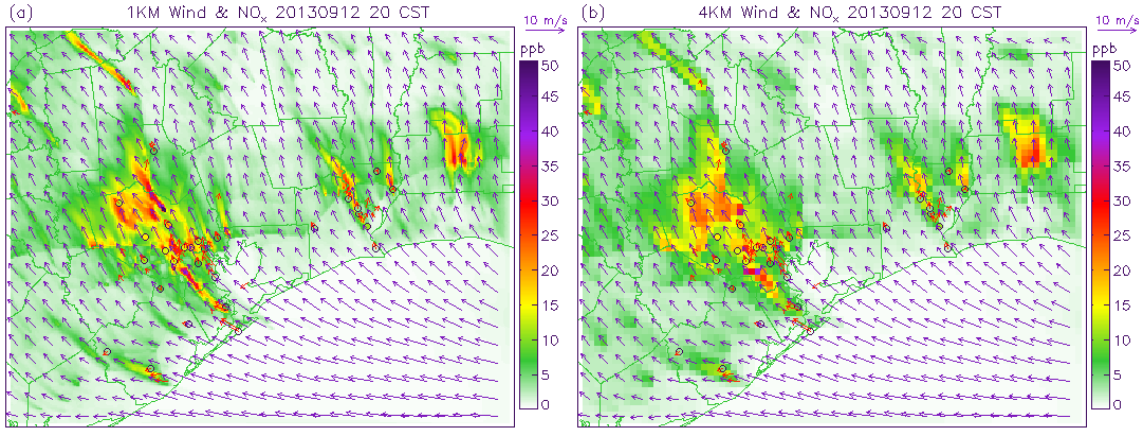

Fig. 4.14. Spatial distributions of surface wind fields and NO_x concentrations at 20 CST on 12th September 2013 (red arrow: CAMS wind; purple arrow: modeled wind; circle: CAMS NO_x; background color: modeled NO_x). The modeled wind vectors were plotted at 12 km intervals for both cases. The actual maps are in 336 km × 264 km.

4.3.3. Site-wide analysis

4.3.3.1. Urban monitoring site

The CAMS site Houston Texas Avenue C411 monitoring site is located in downtown Houston, which experiences high NO_x emissions from vehicular traffic. Time series of simulated surface NO_x and O_3 concentrations from 4KM and 1KM simulations during 5th - 14th September 2013 are plotted in Fig. 4.15 for this site, along with the observational data. Simulated NO_x concentrations reproduced the daily variations in the observations. Both observed and simulated NO_x concentrations were relatively higher during nighttime and peaked early morning, falling to about 10 to 15 ppb persisting during the daytime. The NO_x peaks from the 1KM simulation were higher than those from 4KM,

probably due to emission allocation differences at the location. Simulated O_3 concentrations for 1KM case were lower than 4KM case because of more NO inhibition.

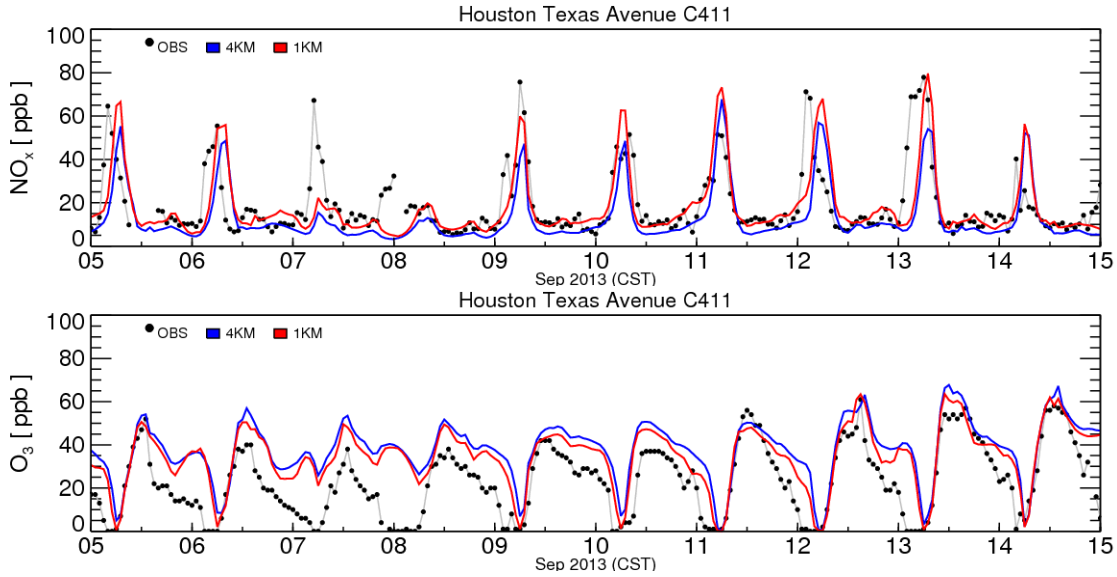

Fig. 4.15. Time series of surface NO_x and O_3 concentrations at CAMS site C411 (in downtown Houston) and from 4KM and 1KM simulations during 5th - 14th September 2013.

The IPR analysis was conducted to identify the main processes contributing to the differences in simulated concentrations for the two cases. Fig. 4.16 plots the IPR results for NO_x at the C411 site during 5th to 14th September 2013 for both cases. As shown in Figs. 5.16-a and b, emission (EMIS) represents the main addition and transport (TRAN) the main removal process. The emission contribution time series here represents the temporal profile of aggregate NO_x emissions from all sources. The maximum emission rates appear around noon each day. Negative transport processes also peak during the same time due to active vertical turbulent diffusion (Fig. 4.17). Emissions still contribute at night albeit with significantly lower magnitudes due to decreased motor vehicle activity (Czader and Rappenglück, 2015). Contribution from cloud processes (CLDS) and dry deposition (DDEP) appear negligible. Hence, both 1KM and 4KM cases exhibited similar process

contribution patterns. The biggest difference between the two model cases was the change in the magnitude of emission and transport processes. The magnitudes of these NO_x emissions varied from 50 ppb hr^{-1} to 400 ppb hr^{-1} for the 1KM case. As NO_x emissions decreased in 4KM case, the positive emission contributions decreased, ranging from 20 ppb hr^{-1} to 180 ppb hr^{-1}; and the negative transport contributions also decreased correspondingly during same period. Despite the large difference in emission rates between 1KM and 4KM model grids, the net change (NET, the sum of all atmospheric physics and chemistry processes) of NO_x in both simulated cases showed similar variation patterns (red lines in Fig. 4.16-a and 5.16-b). A positive NET value indicates an increase in concentrations while a negative indicates decrease. The difference of net change rate between 1KM and 4KM is displayed in Fig. 4.16-c. The daily NET and NET differences were more significant during the night and early morning than daytime. This can be explained by the fact that vertical mixing usually transports smaller proportions of emissions during nighttime/early morning than daytime. For instance, at early morning of 13th September, the combination of emission and transport processes made a positive NET peak about 28 ppb hr^{-1} in 1KM case (Fig. 4.16-a) and 20 ppb hr^{-1} in 4KM case (Fig. 4.16-b), the NET difference is 8 ppb hr^{-1}; while at around noon time when NO_x emission peaks appeared, the vertical mixing currents due to enhanced surface heating were large enough to transport most of the pollutants to upper layers, resulting in reduced NET values and NET difference. Overall, emission rates difference was the primary contributor to NO_x concentrations, while competing emission and transport contributed to the difference in final predicted NO_x concentrations in 1KM and 4KM cases at the urban site.

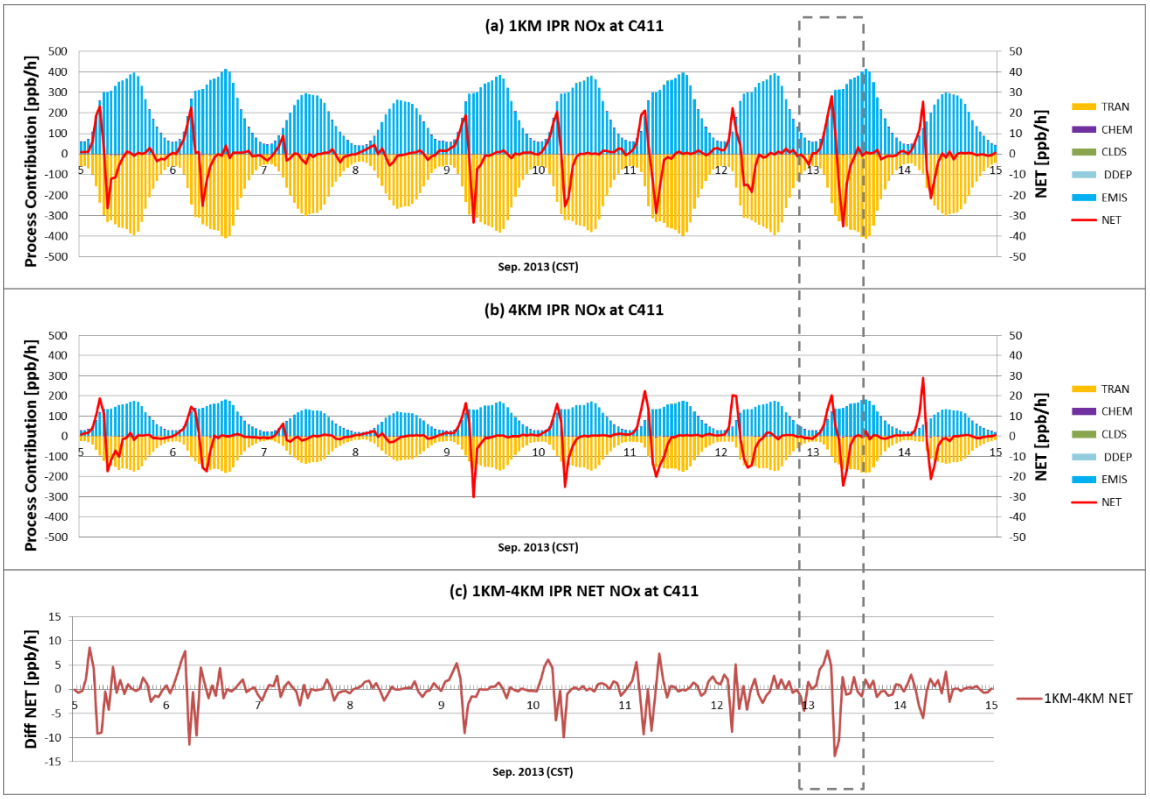

Fig. 4.16. The contributions of atmospheric processes to NO_x concentrations between 1KM and 4KM simulations at urban site C411. (TRAN – total transport processes, CHEM – chemistry reaction, CLDS – cloud process, DDEP – dry deposition, EMIS – emissions; NET – sum of all processes)

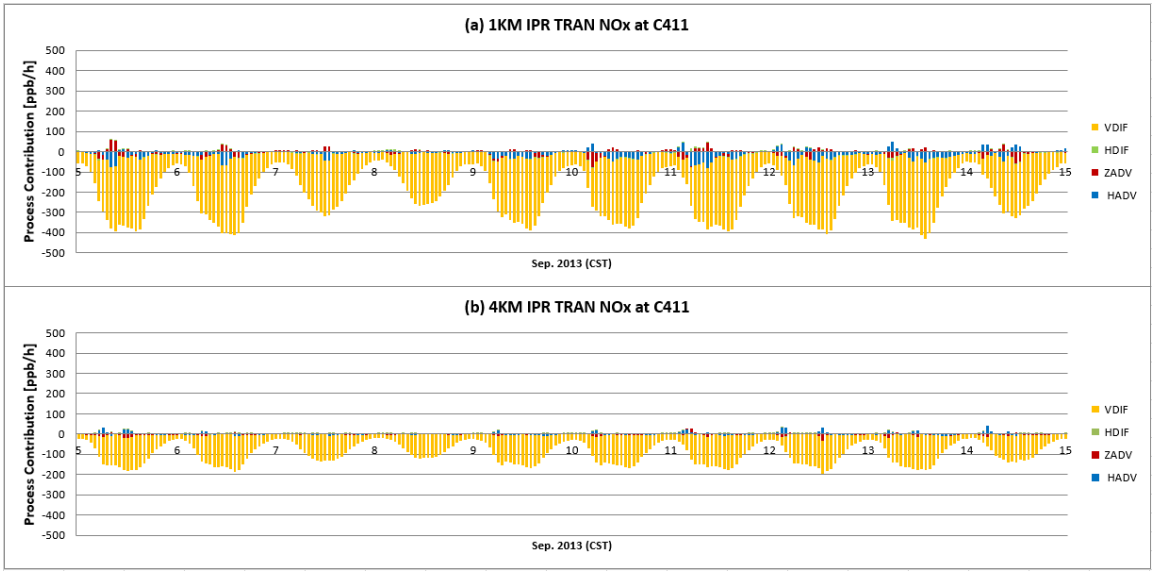

Fig. 4.17. The contributions of transport processes to NO_x concentrations at urban site C411. (VDIF-vertical diffusion, HDIF-horizontal diffusion, ZADV-vertical advection,

HADV-horizontal advection). At this site, vertical diffusion was the dominant transport process during both daytime and nighttime.

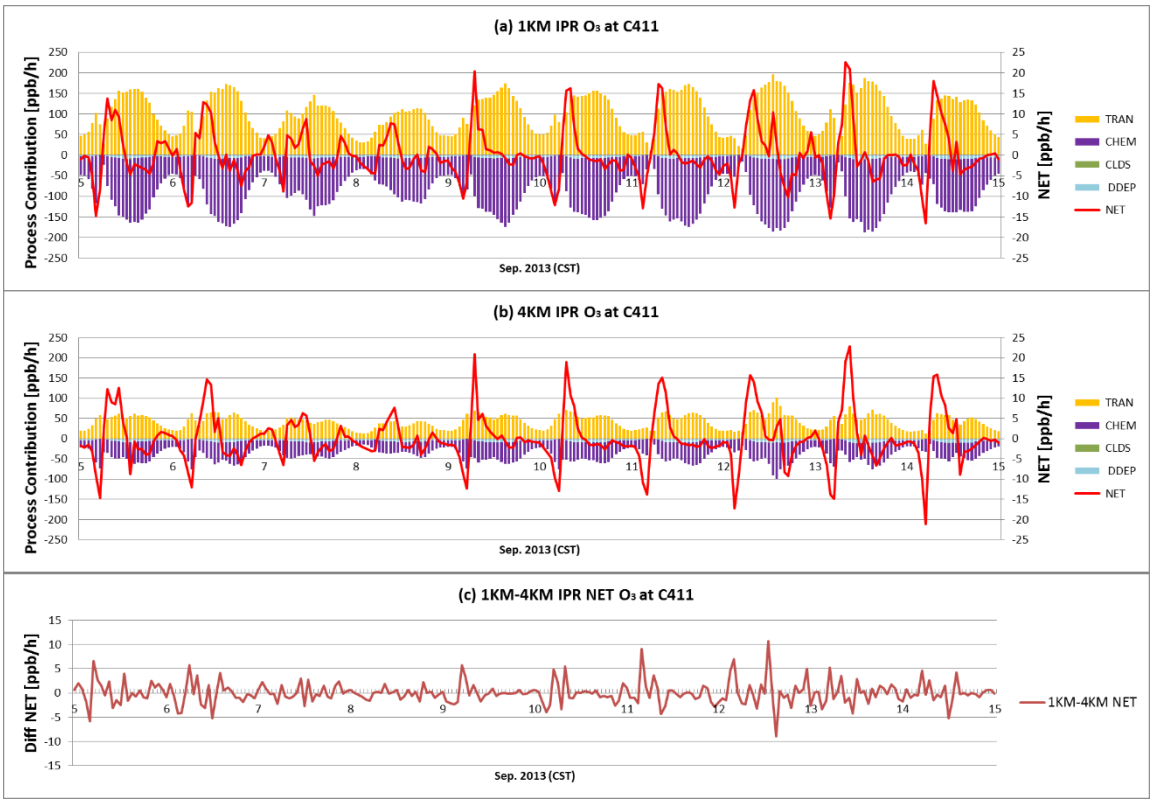

Fig. 4.18. Similar to Fig. 4.16 but for O_3 at urban site C411.

Fig. 4.18 plots the IPR analysis for O_3 in the surface layer at urban site C411. A significant consumption of O_3 by chemistry (CHEM) is predicted during daytime in both cases due to titration by high NO_x concentrations. Specifically, O_3 can react with NO to form NO_2 in the high NO_x environment (Jang et al., 1995b). This suggests that the urban site location, like most other urban sites, was NO_x-saturated as indicated by Choi (2014). The magnitudes of O_3 consumption (Fig. 4.18-a and 5.18-b) are also very different due to large differences in NO_x emission contributions between the two cases (Fig. 4.16). Transport (TRAN) was the main positive contribution to O_3 concentration. So both 1KM and 4KM cases showed similar process contribution patterns for O_3, with the main

difference being in the magnitude of each main contributing process. The difference in NO_x emissions at this location in different size model grids could be treated as the driver behind the differences in O_3 chemistry and simulated O_3 concentrations.

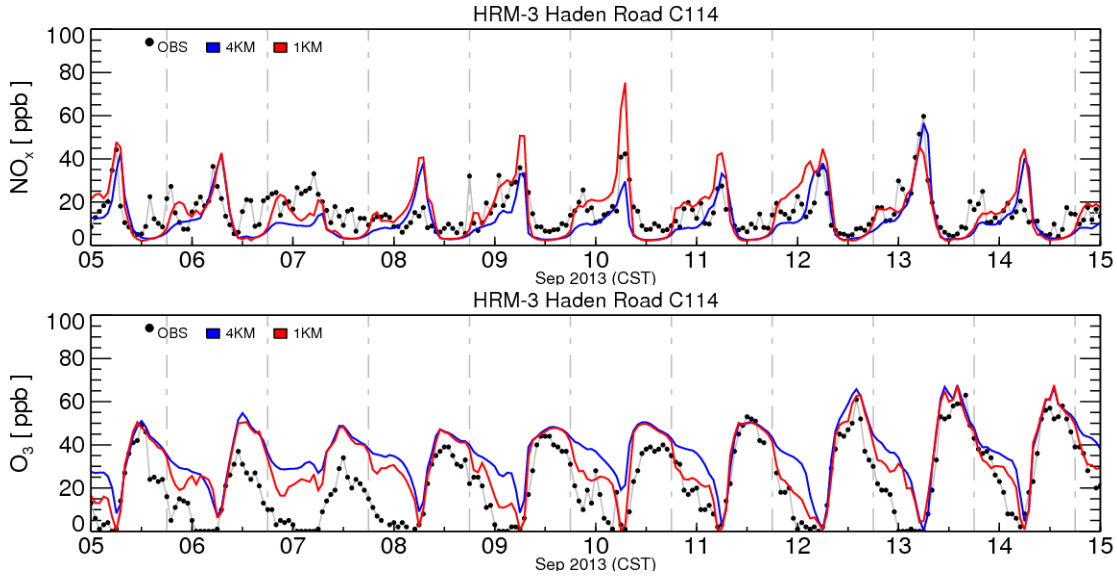

Fig. 4.19. Similar to Fig. 4.15 but at industrial monitoring site C114. The gray dashed lines represent 18 CST on each day.

4.3.3.2. Industrial monitoring site

The HRM-3 Haden Road monitoring site C114 is located in the Ship Channel industrial region. Surface NO_x emissions are relatively low here due to lack of heavy vehicular traffic as compared to the urban site. However, there are significant NO_x emissions above the model surface layer from the petrochemical industrial point sources as indicated in Fig. 4.11. Time series of surface NO_x and O_3 concentrations between CAMS observations and simulations at the industrial site are plotted in Fig. 4.19. The temporal variation patterns for NO_x (with a peak in the early morning) and O_3 (with a peak around noon time) at the industrial site resemble the urban site. However, a notable difference

between time series at the industrial site and urban site was the timing of difference in simulated concentrations between 1KM and 4KM cases. For instance, at the urban site NO_x difference between two model cases appeared distinctly throughout the most of the daytime (Fig. 4.15), while at the industrial site NO_x differences appeared during 18 CST to the early morning of the next day. Also, the 1KM case exhibited higher NO_x and lower O_3 than 4KM case during the nighttime and early morning (Fig. 4.19).

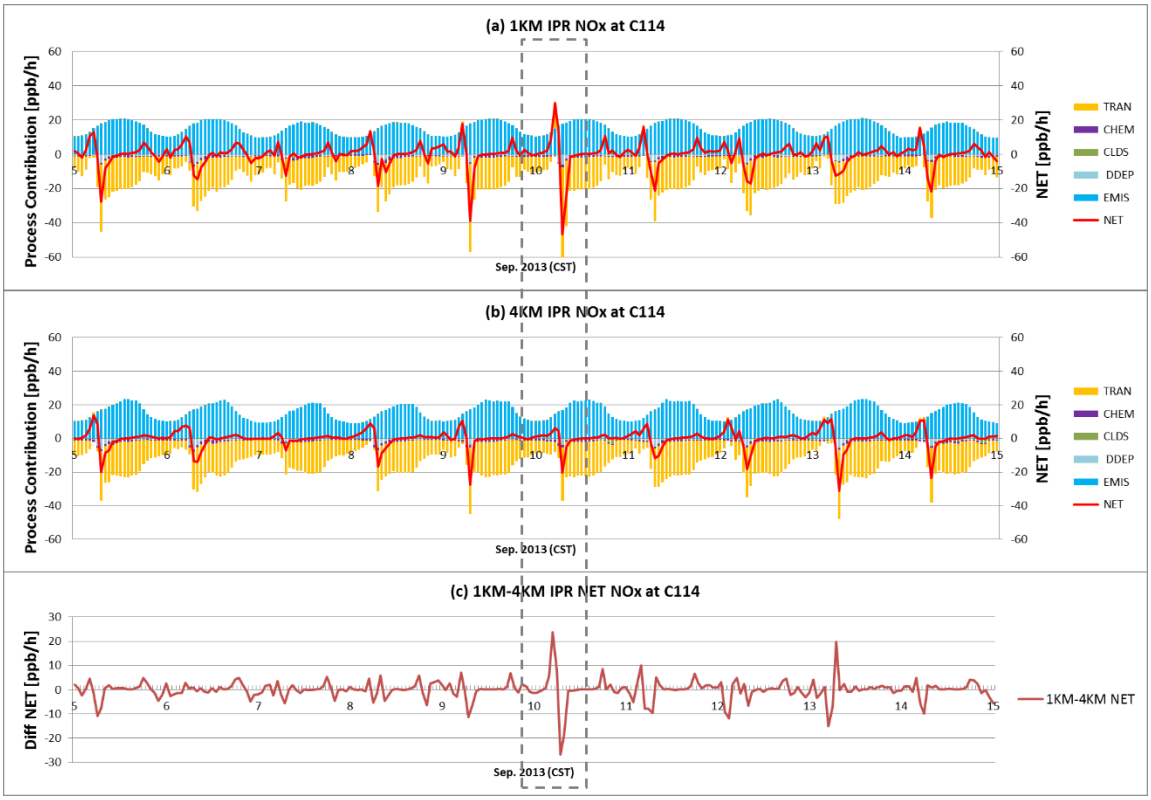

Fig. 4.20. Similar to Fig. 4.16 but for NO_x at industrial site C114.

Fig. 4.20 displays the IPR results for surface layer NO_x at the industrial site C114 for both simulation cases. Similar to the IPR NO_x at the urban site, both 1KM and 4KM cases at the industrial site exhibited similar process contribution patterns, with positive emission contribution and negative transport contribution in general. However, unlike the

urban site where the large difference in emission rates between 1KM and 4KM model grids were exhibited, there was no substantial change in the magnitude of emissions between the two cases. The emission contribution rates at the industrial site were also significantly smaller than the urban site, with a daytime peak about 20 ppb hr^{-1} and nighttime minimum about 10 ppb hr^{-1}. Since the emission contributions in 1KM and 4KM cases were similar, the negative transport process could be considered as the predominant cause behind the different NET NO_x change and different simulated NO_x concentrations. During daytime the transport process or active air mixing transported most of the surface NO_x emissions to the upper layer, causing no clear difference in net change rate between 1KM and 4KM cases (Fig. 4.20-c); while during nighttime and early morning the transport process contributions in the two simulations were not similar. For instance, at 6 CST of 10^{th} September, the transport process contribution even became positive which made a 30 ppb/h positive NET peak in 1KM case (Fig. 4.20-a); at the same time the NET peak in 4KM case was 6 ppb hr^{-1} (Fig. 4.20-b), the NET difference was 24 ppb hr^{-1} (Fig. 4.20-c). The 1KM grid experienced downward advection from the upper layer at the time (Fig. 4.21). Overall, transport rates difference could be the essential contributor to the difference in simulated NO_x concentrations in 1KM and 4KM cases at the industrial site.

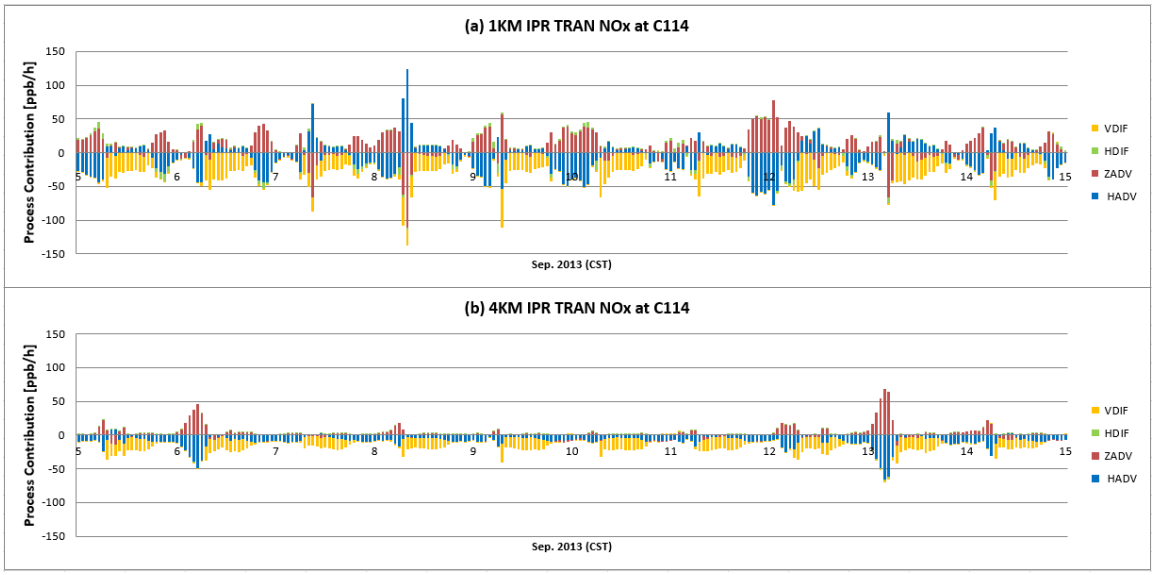

Fig. 4.21. Similar to Fig. 4.17 but at industrial site C114. During the early morning of 10th September, vertical advection contribution was positive and horizontal advection contribution was negative in 1KM case, indicating a downward advection from the upper layer to this grid.

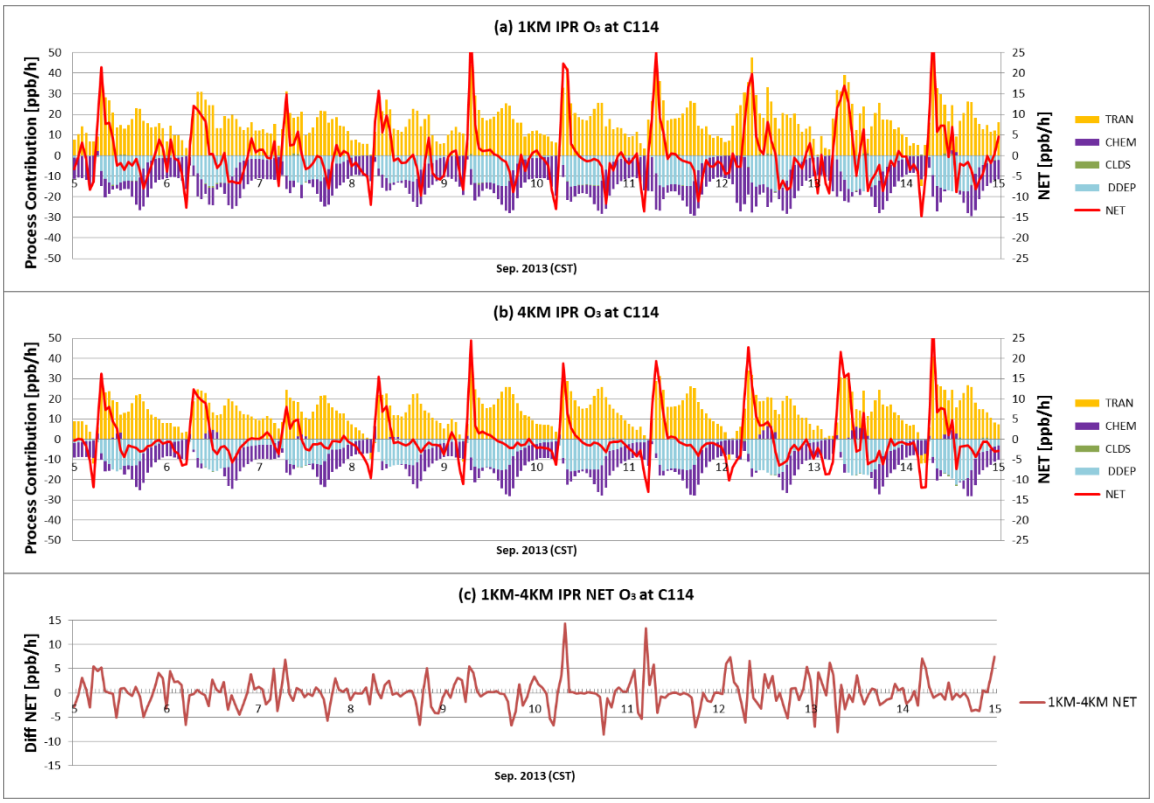

Fig. 4.22. The similar plot as Fig. 4.16 but for O_3 at industrial site C114.

Fig. 4.22 shows the IPR analysis for O_3 in the surface layer for site C114. In both 1KM and 4KM cases, dry deposition was the dominant sink during daytime while chemistry was the major sink during the night to early morning. These were significantly different from the urban location, which experienced significant titration of O_3 by NO_x. The magnitudes of the chemistry destructions in both simulation cases were smaller than at the urban site. Due to the enhanced NO_x concentrations after 18 CST in each day in 1KM case (Fig. 4.19), the magnitudes of chemistry consumptions for O_3 were also a few ppb/h higher during nighttime and early morning in 1KM case (Fig. 4.22-a and 5.22-b). The dry deposition contributions in both cases were similar. In general, chemistry and transport processes should be the main contributors to the difference in simulated O_3 concentrations in 1KM and 4KM cases.

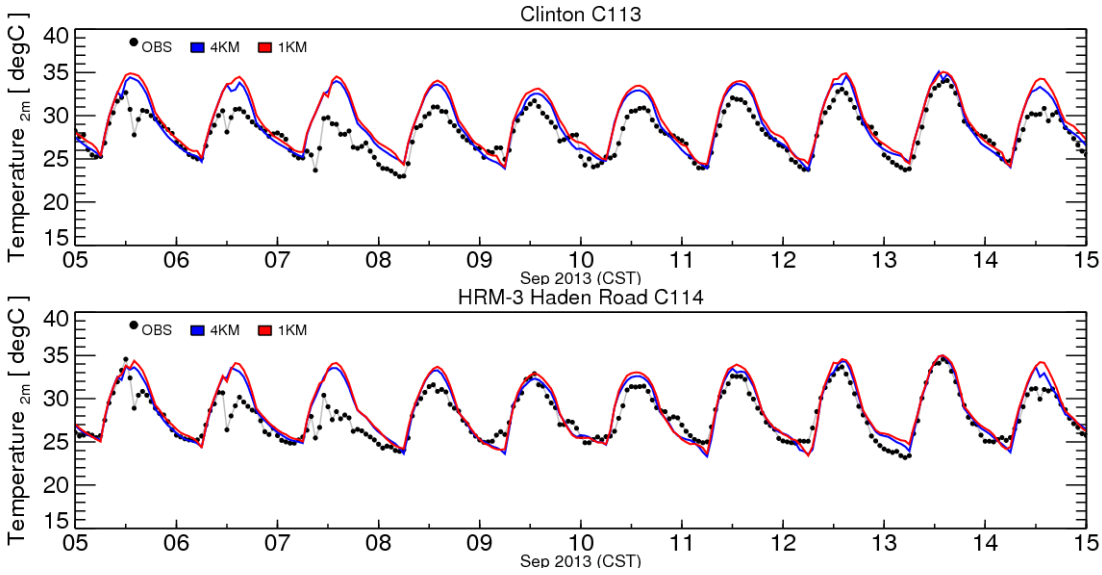

Fig. 4.23. Time series of surface temperature at CAMS site C113 (near C411) and C114 from 4KM and 1KM simulations during 5th - 14th September 2013.

Fig. 4.23 suggests that the over-prediction of O_3 during the nighttime of 5th – 7th September 2013 (in Fig. 4.15 and 5.19) was most likely caused by over-prediction of

daytime temperature. The over-predicted temperature (~5 ºC) in both cases led to higher simulated O_3 during the daytime, accumulating at night due to lower PBL heights. The observations also showed sudden drops right before mid-day of these days, which might be due to the influence of cold fronts in eastern U.S. and local cloud formation.

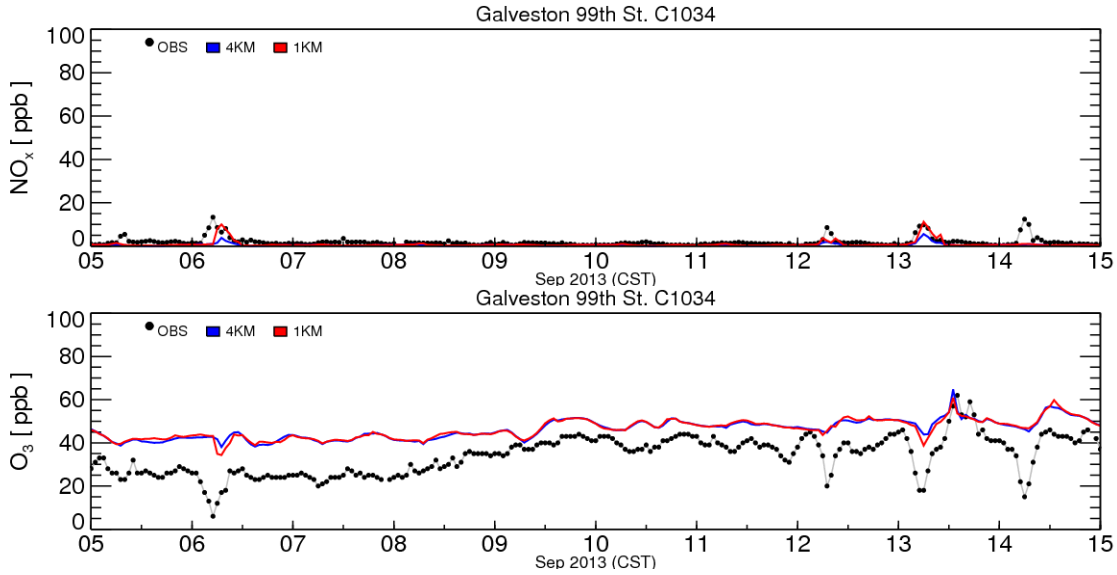

Fig. 4.24. Time series of surface NO_x and O_3 concentrations at CAMS site C1034 and from 4KM and 1KM simulations during 5th - 14th September 2013.

Fig. 4.24 plots a location (CAMS site C1034) with significant lower NO_x emissions than the urban and industrial sites. The differences in NO_x and O_3 between two simulations were also much smaller because of lower NO_x emissions in that environment and negligible influence of transport. The relatively bigger difference in the early morning of 6th and 13th September could be due to the difference in magnitude of transport rates, which could be originally induced by the difference in emissions from source high-NO_x regions. Both simulations over-predicted O_3. The relatively large over-prediction of O_3 along Gulf of Mexico coastline has also been reported in other studies (Nopmongcol et al., 2015; Loughner et al., 2015). These studies suggest halogen chemistry and other possible removal

processes (e.g., dry deposition) specific to the coastal conditions need to be further considered and improved.

Table 4.3. Evaluation of surface NO_x and O_3 concentrations for 5^{th}-14^{th} September 2013.

Site name	Species	Case	N	R	IOA	MAE	MB	OM	MM	MM/OM
Houston Texas Avenue C411	NO_x	4KM	233	0.55	0.70	9.6	-5.9	19.2	13.2	0.69
		1KM	233	0.62	0.78	8.3	-0.6	19.2	18.6	0.97
	O_3	4KM	239	0.79	0.74	15.2	14.9	22.9	37.8	1.65
		1KM	239	0.80	0.80	12.1	11.4	22.9	34.3	1.50
HRM-3 Haden Rd. C114	NO_x	4KM	241	0.64	0.77	7.0	-4.0	15.3	11.3	0.74
		1KM	241	0.67	0.79	7.3	0.1	15.3	15.5	1.01
	O_3	4KM	236	0.84	0.76	15.1	14.8	21.9	36.8	1.68
		1KM	236	0.87	0.86	10.7	10.0	21.9	31.9	1.45

Notation: Same as Table 4.2. Units of MAE/MB/OM/MM for NO_x and O_3: ppb.

Table 4.4. Evaluation of surface NO_x and O_3 concentrations for September 2013.

Site name	Species	Case	N	R	IOA	MAE	MB	OM	MM	MM/OM
Houston Texas Avenue C411	NO_x	4KM	692	0.58	0.72	8.2	-4.6	16.6	12.0	0.72
		1KM	692	0.62	0.77	7.7	0.2	16.6	16.9	1.01
	O_3	4KM	711	0.75	0.73	15.0	13.9	22.6	36.5	1.61
		1KM	711	0.75	0.77	12.8	10.9	22.6	33.5	1.48
HRM-3 Haden Rd. C114	NO_x	4KM	708	0.44	0.58	7.2	-3.8	14.3	10.5	0.73
		1KM	708	0.42	0.61	7.6	-1.4	14.3	12.9	0.90
	O_3	4KM	713	0.76	0.76	14.4	12.1	23.3	35.4	1.52
		1KM	713	0.77	0.81	12.3	9.3	23.3	32.6	1.40

Notation: Same as Table 4.2. Units of MAE/MB/OM/MM for NO_x and O_3: ppb.

Model-measurement statistics for surface NO_x and O_3 for 5^{th} – 14^{th} September 2013 at the urban and industrial monitoring sites for each simulation case are listed in Table 4.3. At the urban site, comparing with 4KM case (correlation: 0.55; IOA: 0.70), the performance of the NO_x simulation was slightly improved in 1KM case (correlation: 0.62; IOA: 0.78). Additionally, the mean bias (MB) showed a large improvement from -5.9 ppb to -0.6 ppb. The evaluation statistics for O_3 were also marginally better for the 1KM case. Similar improvements with finer resolution were noticed for the industrial site for NO_x and O_3. Table 4.4 lists the evaluation statistics for the entire month of September 2013. Due to

the strong synoptic weather influence in the latter half of the month, the performance of O_3 simulations at both monitoring sites decreased, resulting in no significant difference between the two cases.

4.3.4 Vertical difference

4.3.4.1 Comparing with airborne measurements

In order to evaluate model performance for vertical O_3 profiles, the CMAQ simulation results for both grid cases were compared with the NASA P-3B aircraft measurements. Fig. 4.25 displays the time series of NO_y (total reactive nitrogen species), isoprene, and O_3 concentrations during 8:00 CST to 15:45 CST on 12th September 2013. The model values were extracted from the corresponding model grid cells and layers along the flight track. The gray line in each plot represents the flight altitude, which ranged from 90 m to 4.5 km above the surface. Observed NO_y concentrations decreased with increasing altitude, due to lack of aloft emissions sources. Simulated NO_y concentrations agreed with the observations. A difference of up to 5 ppb for simulated NO_y concentrations between 1KM and 4KM cases was reported at lower altitudes (e.g., 300 m height at 10:50, 13:40 and 14:15 CST). No clear change was seen at higher altitudes where NO_y concentrations were relatively low. For isoprene comparisons, simulated values in both cases under-predicted when the high observed values appeared (e.g., at 9:30, 12:20 and 15:00 CST). These high values were measured when the aircraft flew through the forest region near Conroe in Northern Houston. Simulated O_3 differences between two cases appeared at higher altitudes (e.g., at 4.5 km at 15:20 CST), probably due to the difference in transport aloft, which could be originally induced by the surface emissions differences. Fig. 4.26

plots the difference between two simulations to illustrate the grid resolution impact vertically. Overall, both 1KM and 4KM cases had similarly reasonable predictions of the variability of aircraft measurements of NO_y and O_3 in the lower atmosphere.

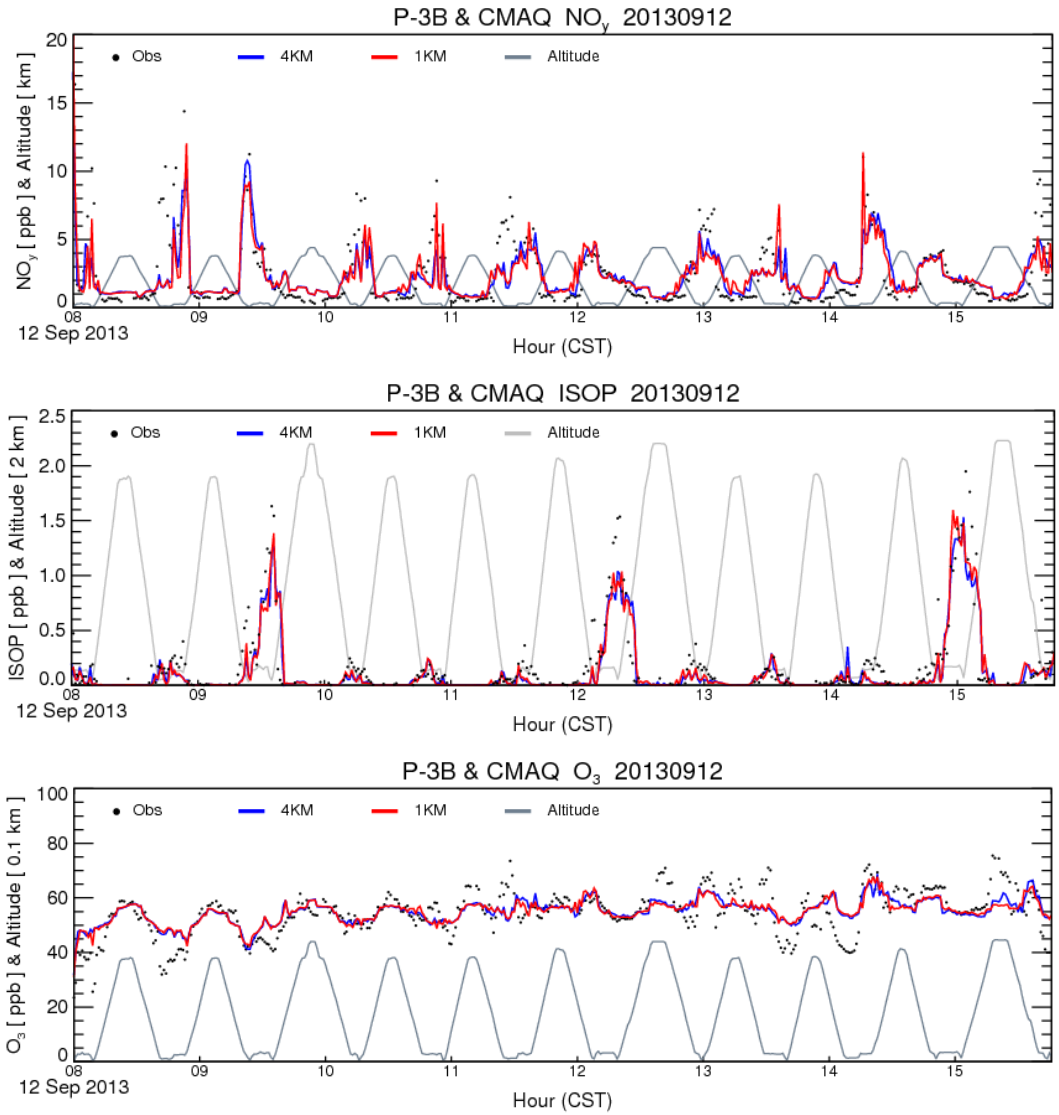

Fig. 4.25. Comparison between aircraft measured and CMAQ-simulated NO_y, isoprene, and O_3 concentrations along NASA P-3B aircraft track during daytime of 12th September 2013. The "Altitude" (gray line) in each plot represents the height reached by aircraft at a given time. Note: the "Altitude" and chemical species shared the same label on left y-axis.

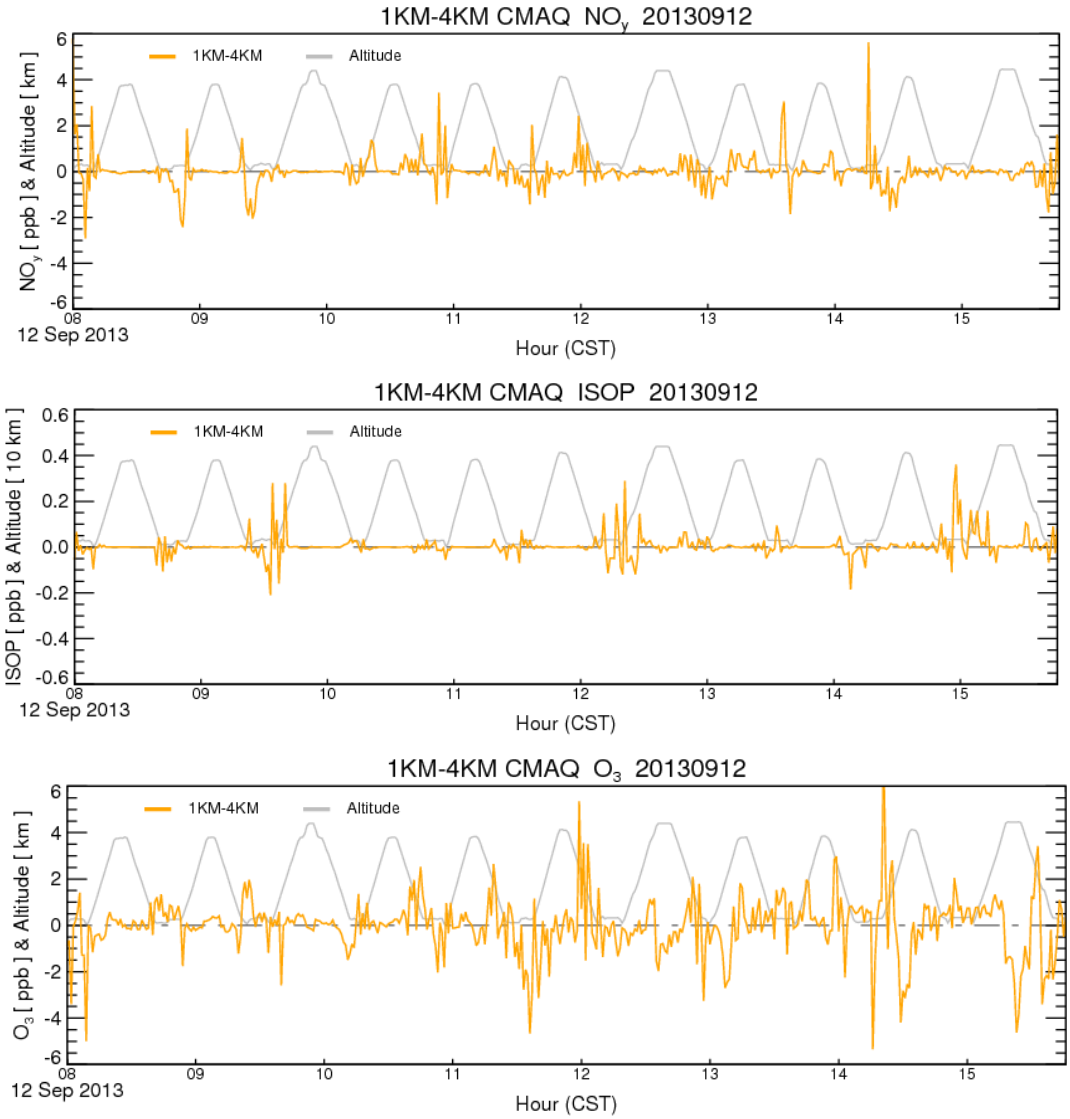

Fig. 4.26. The difference (up to ~5 ppb) between 1KM and 4KM CMAQ-simulated NO_y, isoprene, and O_3 concentrations along NASA P-3B aircraft track during daytime of 12th September 2013.

4.3.4.2 Distributions of O_3 change rate resulting from chemistry reactions

The IRR tool in CMAQ was used to calculate the net O_3 change by considering all chemical reactions related to the production or loss of O_3 (henceforth referred as NET [O_3]). In short, NET [O_3] = total O_3 (chemistry, production) – total O_3 (chemistry, loss); at a given hour. Fig. 4.27 plots NET [O_3] for 1KM and 4KM cases at 5 CST on 12th September 2013

at the surface layer. During the early morning, O_3 destruction by NO titration resulted in large negative NET [O_3] rates over urban areas and along roadways.

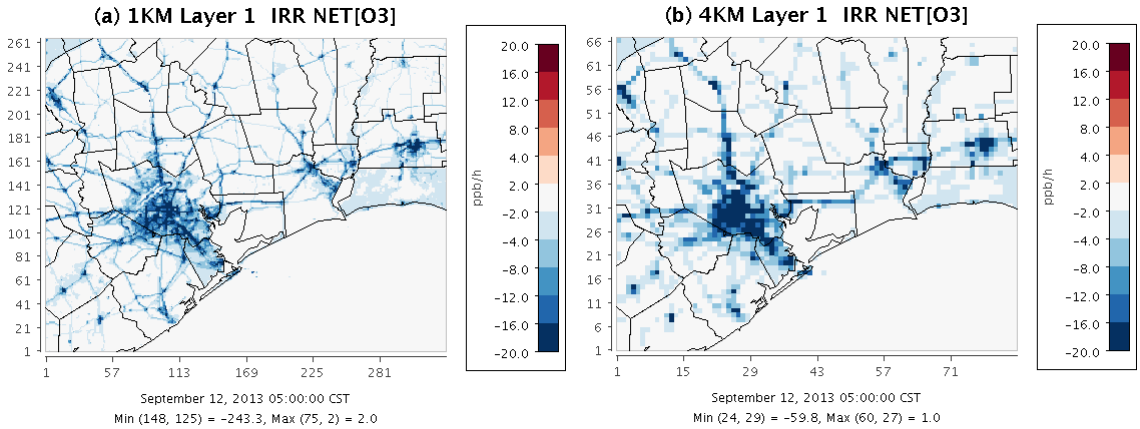

Fig. 4.27. Surface-layer chemistry-induced net O_3 differences between 1KM and 4KM cases at 5 CST on 12th September 2013. The numerals on the bottom and left side of the maps are the numbers of grid cells.

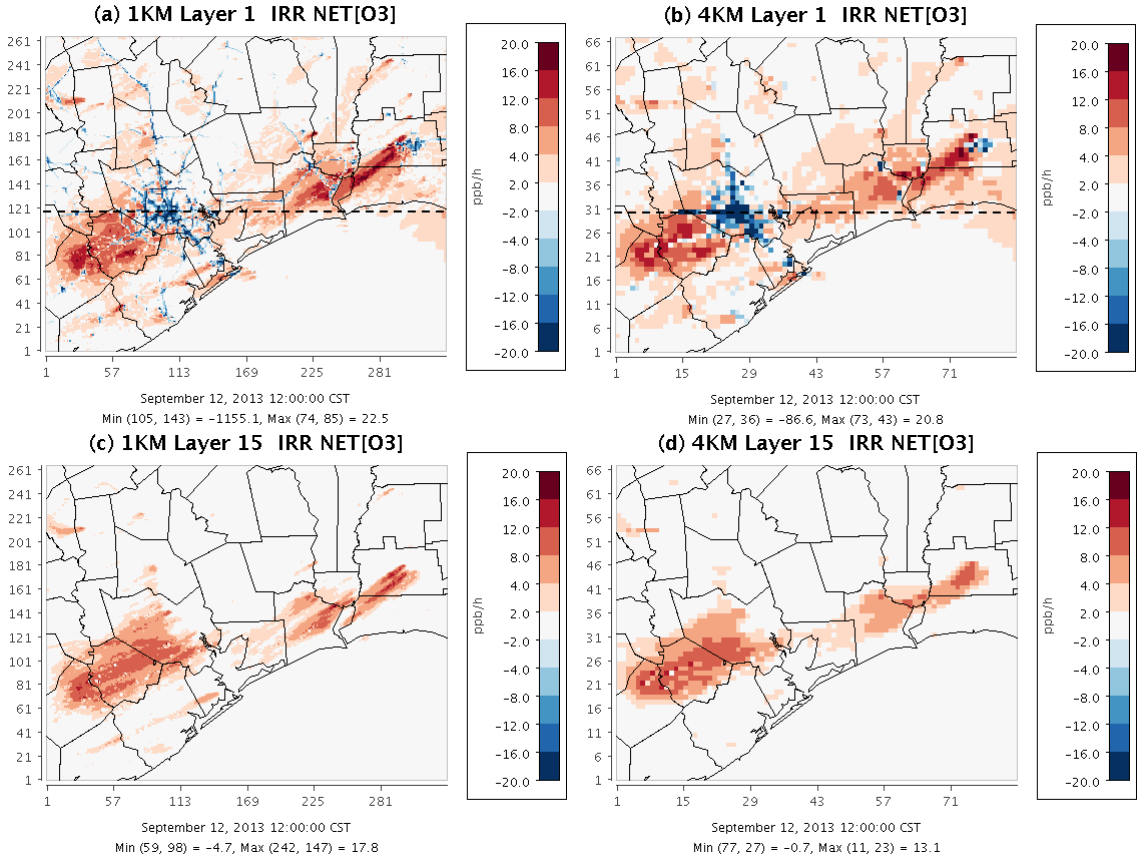

Fig. 4.28. The chemistry-induced net O_3 change between 1KM and 4KM cases at 12 CST

on 12th September 2013, at varying altitudes (Layer 1: surface; Layer 15: a height of about 1.5 km). The numerals on the bottom and left side of the maps are the numbers of grid cells.

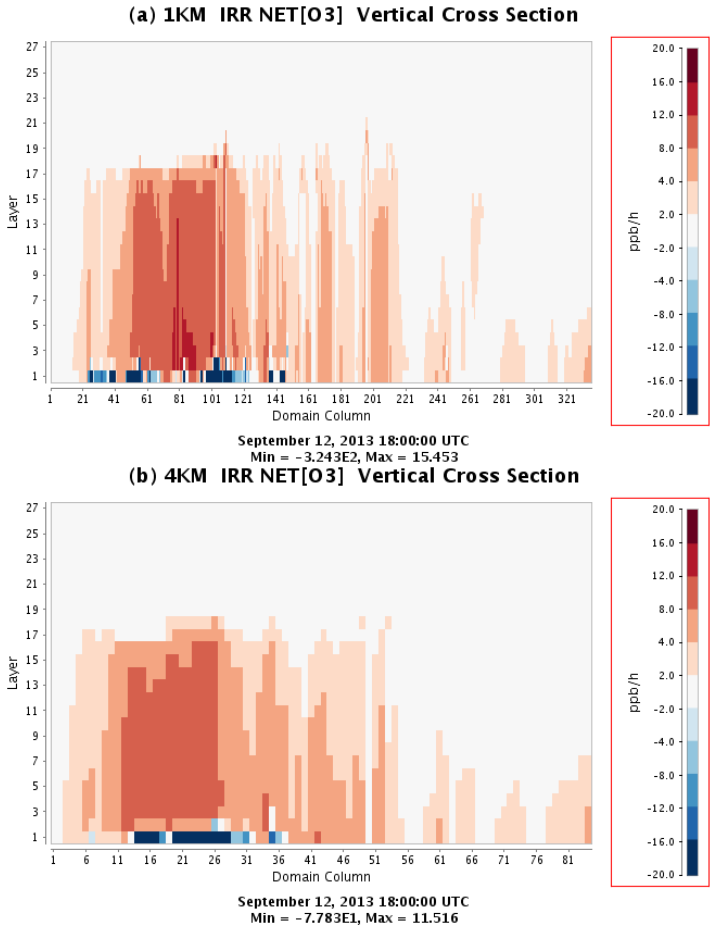

Fig. 4.29. Vertical cross section of chemistry-induced net O_3 difference between 1KM and 4KM cases at 12 CST on 12th September 2013, along the dashed lines (shown in Fig. 4.28-a and 5.28-b) crossing the Houston downtown area.

As shown in Fig. 4.28, at noon time the negative NET [O_3] were still dominant in the urban area at surface layer; and the positive NET [O_3] areas were located downwind of urban or heavy NO_x emission regions, suggesting O_3 formation in the outflow. Both simulation cases showed similar distribution patterns of O_3 chemistry change. However, the maximum chemistry destruction of O_3 in 1KM case (-1155.1 ppb hr^{-1}, Fig. 4.28-a) was more than 10 times higher than in 4KM case (-86.6 ppb hr^{-1}, in Fig. 4.28-b). The maximum

chemistry destruction of O_3 in both cases occurred at the IAH airport, a location with significant NO_x emissions from aircraft, motor vehicles and non-road airport duty vehicles. The large difference between the two cases here was similar to the difference in CHEM process at the urban site in Fig. 4.18. At 1.5 km height, the NET [O_3] at an urban area in both cases turned positive due to lower NO_x concentrations at this layer. Fig. 4.29 plots the NET [O_3] vertical cross section at noon time along dashed horizontal lines (shown in Fig. 4.28-a and 5.28-b) crossing the Houston downtown area. Both cases had similar distribution patterns, with negative values at the surface over urban areas, major positive values aloft in the west part of the lower atmosphere due to easterly wind at the time, and vertical extent reaching to model's 18^{th} layer (about 2.3 km height). However, several differences could be found considering detailed model patterns. For instance, the only negative location in the second layer in 4KM case (above domain 26^{th} column) was right above the urban center; the corresponding location in 1KM case had darker colors indicating significantly lower values. In 1KM case, more NO_x was transported from surface layer to the second layer at the urban area (Fig. 4.16), titrating more O_3 in the second layer. Also, the 1KM case showed higher positive values (>12 ppb hr^{-1}) in the lower atmosphere, indicating that the combinations of NO_x and VOC in these NO_x-limited areas were more favorable to O_3 production. Larger variability of the chemistry-induced net O_3 change were predicted in 1KM case (-324.3 to 15.5 ppb hr^{-1}) than 4KM case (-77.8 to 11.5 ppb hr^{-1}) vertically.

4.4. Summary and Discussion

This study used a WRF-SMOKE-CMAQ air quality modeling system to investigate the impact of spatial resolution on model predictions of NO_x and O_3. We used the U.S. EPA's approach to allocate county-based emissions to model grid cells, and generated two sets of emission files for southeastern Texas in 1 km and 4 km horizontal resolutions. Detailed spatial emissions features from various sources and steeper gradients of surface NO_x and O_3 concentrations were seen at 1 km resolution for heavily polluted areas. In addition to the fine resolution emissions, this study also used WRF meteorology fields at 1 and 4 km resolution for the modeling system. Although the two WRF runs used same physics parameterizations and grid analysis nudging, there were small-scale difference of temperature, wind, PBL, and cloud fraction. These differences are probably due to the difference in cloud simulation over fine-scale grid spacing. A detailed study of the fine-scale cloud simulations using different schemes and their impact on air quality is needed in the future.

Since both meteorology and emissions can impact the CMAQ results, the Integrated Process Rates and Integrated Reaction Rates diagnostic tools in CMAQ were used to differentiate the impact of emissions, transport, chemistry, and deposition. Our results indicated that in source regions with high NO_x emissions, the difference in emission rates was the primary contributor to the difference in final predicted NO_x and O_3 concentrations for the two resolutions. In industrial regions with significantly lower NO_x emissions, transport rates were the main cause of the difference. However, the difference in magnitude of transport could originally be induced by the emissions difference in source regions. One

interesting point from the IPR analysis is that while emissions exhibit the substantial difference between 1 and 4 km grids or urban and industrial locations, the NO_x concentrations are similar. These could partially explain the results of Czader et al. (2015), who found that after reduction of on-road NO_x emissions by 30% and anthropogenic point source emissions by 20%, the change in NO_x concentrations were very small during the daytime and the change in O_3 concentrations were below 1%, between the original and reduced emissions cases. Due to the interplay of various atmospheric processes (e.g. emission, transport, and chemistry), we cannot expect a similar level of reduction of the gas-phase air pollutants as the reduction of emissions.

Both simulations reproduced the variability of NASA P-3B aircraft measurements of NO_y and O_3 concentrations aloft (from 90 m to 4.5 km). The difference between the two simulations aloft was up to ~5 ppb, due to higher NO_x concentrations from the 1KM case being transported into the NO_x-limited upper layer. The statistical analyses showed no significant difference between the two simulations for ground-level concentrations, while 1KM case showed more detailed features of emissions and concentrations in heavily polluted areas, such as highways, airports and industrial regions. Our results indicate that finer resolution can help understand the causes of pollution at zipcode-level and also quantify the effect of range transport from suburban industrial regions to populated urban locations and vice versa. So it is needed to use 1 km grid resolution when performing air quality model simulations to study the response of future projections of mobile source emissions (e.g. gasoline and diesel vehicles) or point source emissions (e.g. coal and natural gas power plants). In the perspective of the operational O_3 forecast, due to the

computational expensive of 1 km simulation, a fine-scale prediction in 4 km grid resolution might be enough.

The IRR analyses indicated distinctive differences of chemical processes between the model surface layer and upper layers. The O_3 titration still occurred in the urban area in the surface layer (0-32 m) even during the noon time, while the O_3 production started from the 2nd model vertical layer and continued to the height of PBL (~2.3 km). This implies that correcting the meteorological conditions in the surface layer (e.g. WRF observational nudging of temperature and wind fields using surface observations) can improve the performance of meteorological predictions at surface monitoring stations, but may not help to significantly improve the O_3 model prediction. The model-observation O_3 bias in our studies, such as relatively large over-prediction during the nighttime in some days, or over-predictions along the Gulf of Mexico coastline, are due to inaccurate meteorology (e.g. over-prediction of temperature resulting in sustained O_3 chemistry), uncertainties in chemistry or other processes, which warrant further investigation. Horizontal grid resolution is unlikely the major contributor to these biases.

Chapter 5. Evaluation of the air quality impacts of increased freight traffic in the Houston Metropolitan Area in a future year

5.1 Introduction

The Houston Metropolitan region is the 4th largest urban area nationally and is in nonattainment for ozone (O_3). It is also in borderline attainment for fine particulate matter ($PM_{2.5}$). Additionally, the counties bordering the region (namely Brazoria, Chambers, Fort Bend, Galveston, Harris, Liberty, Montgomery, and Waller) are in nonattainment with respect to O_3. Hence, it is necessary to identify the sources of these pollutants and their precursors so as to develop appropriate control policy. Transportation sources in urban areas (gasoline motor vehicles and diesel trucks) are the major sources of nitrogen oxides (NO_x) and Volatile Organic Compounds (VOCs), which react in the presence of sunlight to form O_3. In addition to O_3 precursors, vehicular traffic also emits important components of particulate matter such as organic and elemental carbon.

As indicated by the 2013 Houston-Galveston Area Council (H-GAC) Regional Goods Movement Plan, the population of the Houston Area is projected to grow by 50% in 2040, which could potentially result in an increased trucking and other freight activity to meet the needs of the growing population. It is projected that the number of trucks in the region could double by 2040. It is, therefore, imperative to carry out an impact analysis study to evaluate the air quality impacts of increased transportation and the effects of

control technologies and strategies. In this study, we developed future projections for trucking emissions and evaluated various emissions scenarios related to varying levels of emission control. Each scenario was used in a fine resolution (1 km) WRF-SMOKE-CMAQ air quality modeling system to estimate its impacts on regional ozone and $PM_{2.5}$.

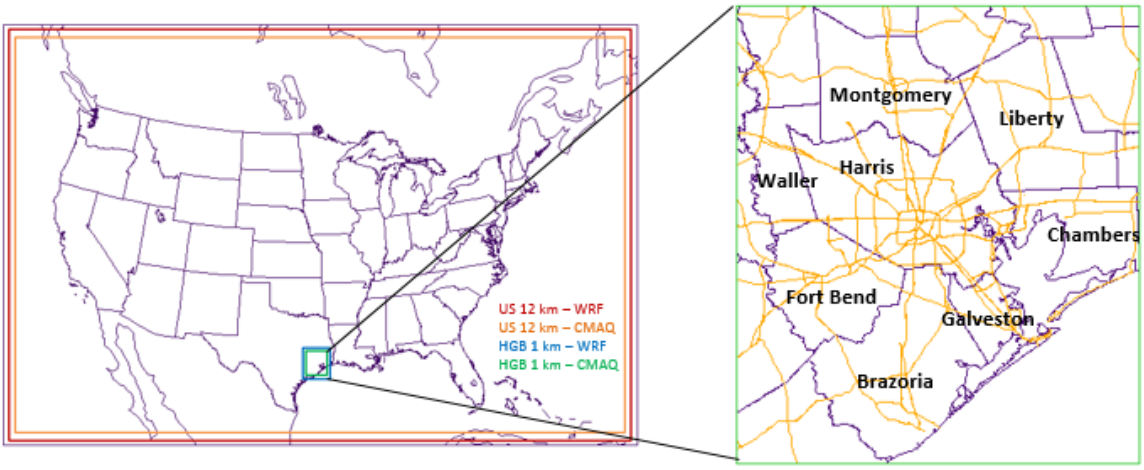

Fig. 5.1. Horizontal domains of WRF and CMAQ at different grid resolution; the HGB 1 km is used in this study while the US 12 km is used to provide boundary conditions. For the zoomed-in plot on the right, roadways are represented in orange and county boundaries in purple. The HGB 1 km CMAQ domain is in 176 km × 200 km.

5.2. Methodology

5.2.1. Model set-up and observational data

This study used the CMAQ model version 5.0.2 with the CB05 chemical mechanism and AERO6 module, WRF model version 3.7, and SMOKE version 3.6 with NEI-2011. The 1 km resolution simulation domain covered the 8-county HGB area, as depicted in Fig. 5.1.

The TCEQ's CAMS network chemical species measurements were used to evaluate model performance for O_3, NO_x, CO, ethylene, toluene, and xylenes.

5.2.2. Mobile source emission processing

This study employed the USEPA's Motor Vehicle Emissions Simulator (MOVES) (https://www.epa.gov/moves) and SMOKE coupled model. The MOVES model provides emission factor look-up tables for mobile emissions as a function of speed, fuel type, vehicle type, road type, and meteorological conditions, while SMOKE does the spatial and temporal allocation, and speciation for CB05.

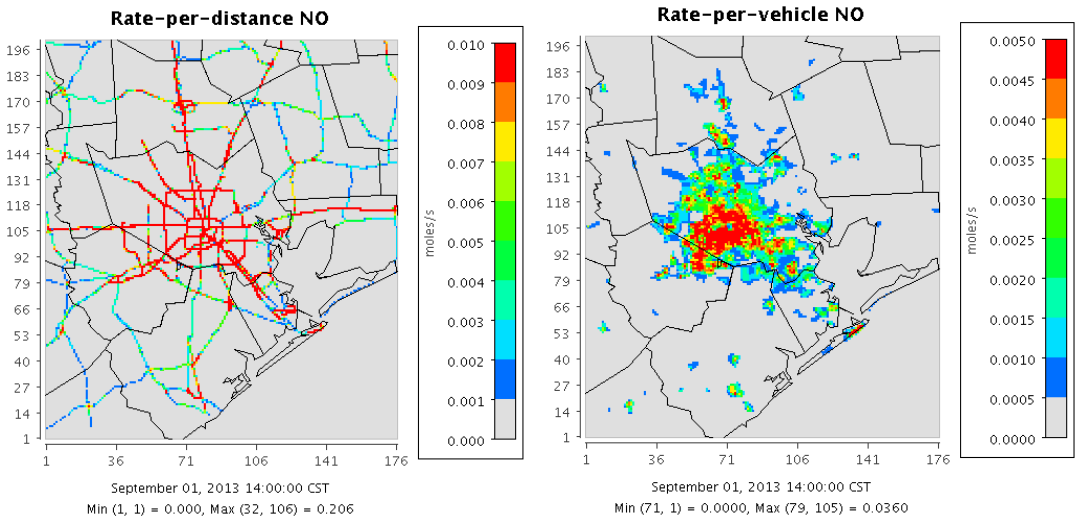

Fig. 5.2. Spatial distributions of Base-year NO emissions from different source sectors at 14 CST on 1st September 2013. The left panel depicts Rate-per-distance while the right panel plots Rate-per-vehicle. The numerals on the bottom and left side of the maps are the numbers of grid cells.

In Fig. 5.2, the 'Rate-per-distance' or RPD represents on-roadway mobile sources and emission processes (e.g., running and crankcase running exhaust, evaporative, brake and tire wear). These emissions distributions highlight the roadway networks inside the simulation domain. The RPD emissions can be calculated using the following simplified formula:

$$Emission_{RPD} = EF_{RPD} \times hourly\ VMT \quad (6.1)$$

where the unit of EF_{RPD} is g/mile and VMT represents vehicle miles travelled.

The 'Rate-per-vehicle' or RPV represents off-network mobile emissions (e.g., start exhaust, evaporative permeation, fuel leaks). These emissions were predominantly concentrated in the urban locations and calculated as:

$$Emission_{RPV} = EF_{RPV} \times VPOP \quad (6.2)$$

where the unit of EF_{RPV} is g vehicle^{-1} hour^{-1}, and $VPOP$ denotes vehicle population in numbers. The VMT and VPOP activity data are from NEI-2011 and vary with county and source attributes such as fuel type, vehicle type, road type, and emission processes.

5.2.3. Base year and future projection scenarios

Future projections were developed for diesel freight trucking emissions, and designed several emissions scenarios with varying levels of emission control. The following simulation scenarios will be considered:

(1) A Base-year case, representing the month of September 2013.

(2) A "un-control" (UC), or "business as usual" case, where the trucking fleet in 2040 will have the same emission factors as in 2011. The VMT and VPOP will increase to the 2040 values.

(3) An "intermediate emissions" (INT) case, where 50% fleet turnover is assumed, i.e., 50% of the fleet is replaced with vehicles using clean combustion or stringent emission control technologies.

(4) A "best control" (BC) case, where 100% of the trucking in 2040 is replaced by state-of-the-art vehicles.

(5) A "zeroing diesel freight" (ZDF) case. This case is only used to calculate the diesel fraction in the mobile emissions from all type of fuels. It could also be potentially interpreted as 100% of the trucking fleet being replaced by electric vehicles under the completely green grid.

Table 5.1. Descriptions of the simulation scenarios.

Simulation Scenario	Scaling factors for future projections			
	EF_{RPD}	VMT	EF_{RPV}	VPOP
Base-year (2013)	× 1	× 1	× 1	× 1
Un-control (UC)	× 1	× 1.5	× 1	× 2
Intermediate (INT)	× 0.525		× 1	
Best-control (BC)	× 0.05		× 1	
Zeroing diesel freight (ZDF)	× 0		× 0	

Table 5.1 lists the scaling factors for each simulation scenario. The effective emission factors were calculated as described in the USEPA's National Mobile Inventory Model (NMIM):

$$EF_i(2040) = EF_i(2013)\left[f_{replaced}(1 - f_{control}) + 1 - f_{replaced}\right] \qquad (6.3)$$

where $EF_i(2040)$ is the emission factor for 2040, $EF_i(2013)$ the emission factor for the base year of 2013, $f_{replaced}$ represents the cumulative fraction of the fleet that has been replaced with newer, lower emitting sources between 2013 and 2040, and $f_{control}$ represents the fractional reduction of emissions brought about by this fleet replacement; assumed to be 95% based on Roy et al. (2014). The $f_{replaced}$ term equals 50% and 100% in the INT and BC cases, respectively. Based on equation (6.3), the scaling factors listed in Table 5.1 (0.525 and 0.05) for EF_{RPD} were obtained.

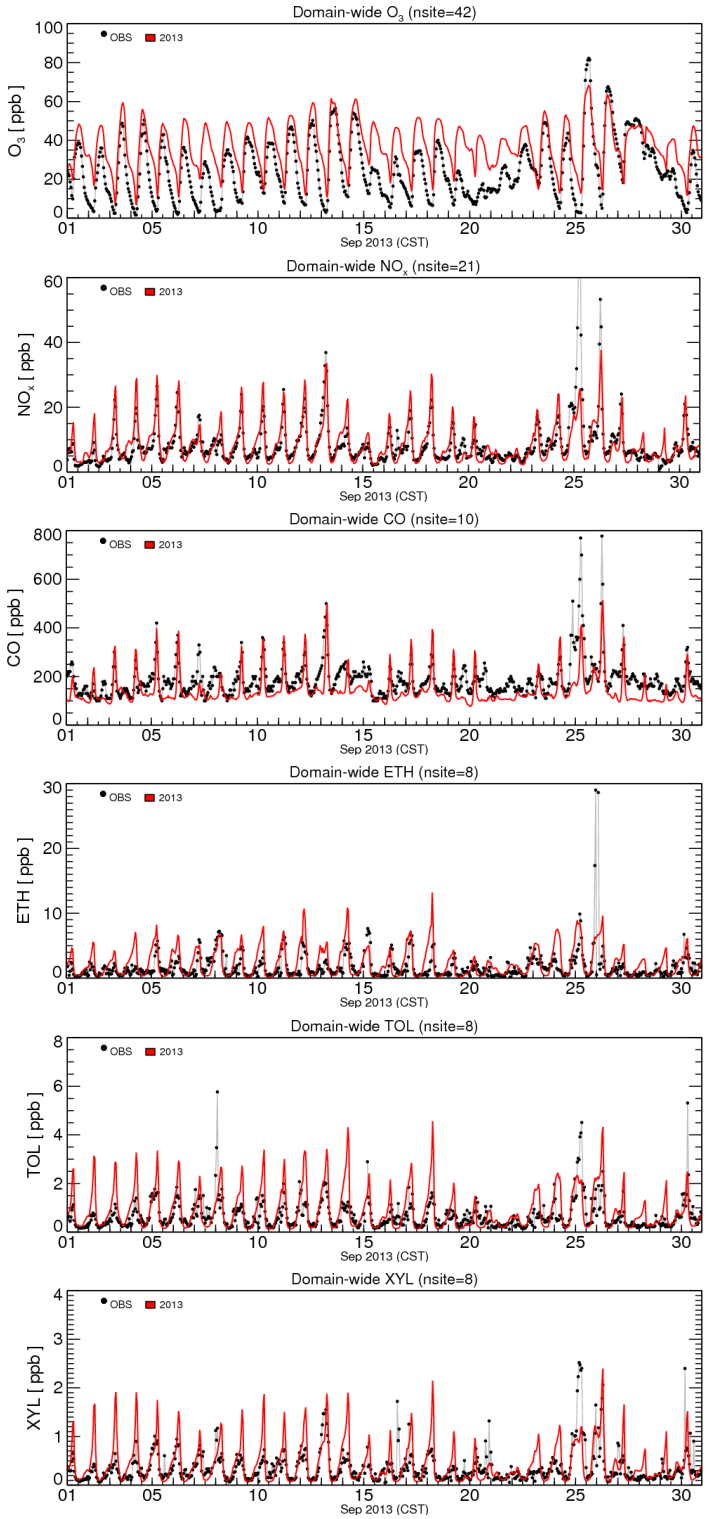

Fig. 5.3. Time series of domain-wide surface concentrations of O_3, NO_x, CO, ethylene, toluene, and xylenes between CAMS observations (OBS) and Base-year simulation (2013) during September 2013.

5.3. Results

5.3.1. Evaluation of the Base-year modeling

Domain-wide time series comparisons of surface O_3 and its precursors between Base-year model output and CAMS observations for September 2013 are presented in Fig. 5.3. The results are also similar to the 4 km simulation of Li et al. (2016) and Pan et al. (2015; 2017a; 2017b).

5.3.2. Freight traffic emissions changes in the future scenarios

Fig. 5.4 plots the total RPD and RPV emissions averaged over the 8-county area for each simulation scenario during September. These numbers included emissions from both gasoline and diesel vehicles. The results indicate that for the RPD sector, NO_x emissions in UC case increased due to the growth of mileage travel in the year 2040, comparing to 2013. The emissions in the INT and BC cases demonstrated moderate and large reductions, respectively. The ZDF case represents the approximate amount of emissions from gasoline due to no diesel emissions. For the RPV sector, the changes between 2013 and future-year cases were marginal. This could be attributed to the fact that diesel freight traffic usually travel long distance without stopping, producing significantly fewer emissions from start exhaust than gasoline vehicles. So the emissions from gasoline are the major component of the RPV sector. Similar comparisons were noticed for VOC and $PM_{2.5}$ emissions. Table 5.2 lists the emissions in 2013 case and the fraction changes in 2040 for NO_x, $PM_{2.5}$, and VOCs including few important air toxic species. If no controls are applied, the fraction increase is large in UC case for some species in the RPD sector;

while a substantial decrease in emissions can be achieved if best control is applied. These species are NO_x (19.9%, -36.9%), PM_{10} (16.8%, -31.1%), $PM_{2.5}$ (31.5%, -58.3%), and hazardous air pollutants such as formaldehyde (25.9%, -47.9%), acetaldehyde (19.8%, -36.7%), acrolein (32.8%, -60.7%), and Naphthalene (24.0%, -44.4%). The values in parentheses represent factional changes of each species emissions for the UC and BC cases respectively.

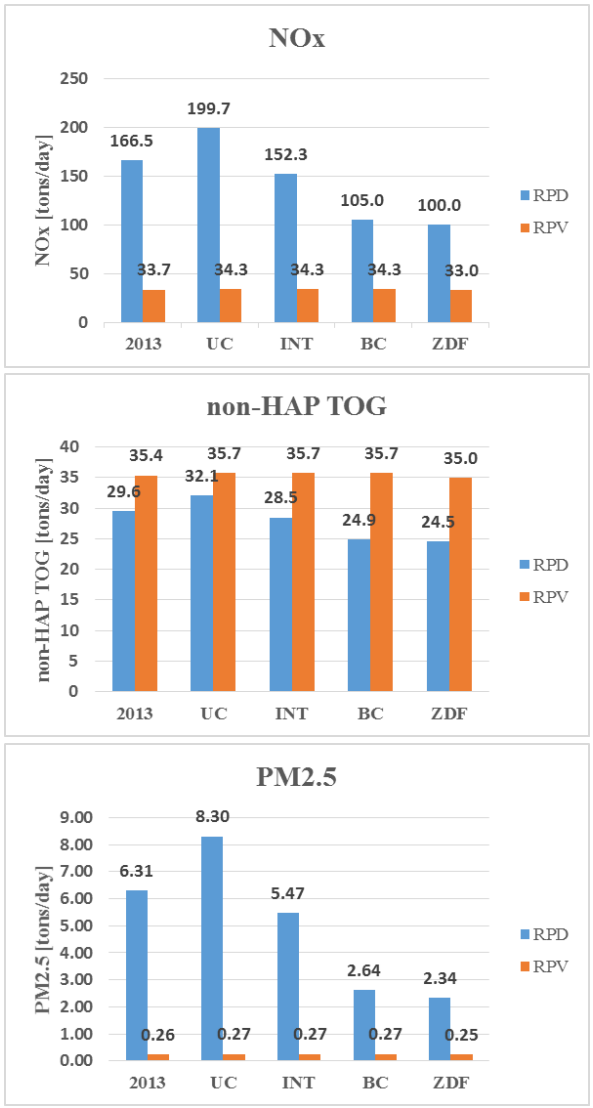

Fig. 5.4. The averaged 8-county total RPD and RPV mobile emissions [Unit: tons/day] in each simulation scenario during the simulation period.

Table 5.2. The averaged 8-county total RPD and RPV mobile emissions in the Base-year case and changes in the future scenarios.

Species	Rate-per-distance					Rate-per-vehicle		
	2013	Differences to 2013 [%]				2013	Differences to 2013 [%]	
	[tons/day]	UC	INT	BC	ZDF	[tons/day]	UC/INT/BC	ZDF
CO	912.71	1.9	-0.8	-3.5	-3.7	304.48	1.3	-1.3
NO_x	166.45	19.9	-8.5	-36.9	-39.9	33.66	1.9	-1.9
NH_3	5.48	1.8	-0.7	-3.3	-3.5	0.00	0.0	0.0
SO_2	1.65	3.5	-1.5	-6.5	-7.0	0.03	1.4	-1.4
PM_{10}	16.40	16.8	-7.1	-31.1	-33.6	0.29	3.4	-3.4
$PM_{2.5}$	6.31	31.5	-13.4	-58.3	-63.0	0.26	3.5	-3.5
non-HAP TOG	29.56	8.5	-3.6	-15.7	-17.0	35.37	1.0	-1.0
Benzene	1.03	2.2	-0.9	-4.1	-4.4	1.38	0.2	-0.2
Formaldehyde	0.90	25.9	-11.0	-47.9	-51.8	0.55	5.9	-5.9
Acetaldehyde	0.52	19.8	-8.4	-36.7	-39.7	0.55	2.6	-2.6
Acrolein	0.06	32.8	-14.0	-60.7	-65.7	0.03	7.9	-7.9
Butadiene, 1,3-	0.15	5.2	-2.2	-9.6	-10.4	0.28	0.4	-0.4
Naphthalene	0.11	24.0	-10.2	-44.4	-48.0	0.08	4.6	-4.6
N_2O	0.86	1.2	-0.5	-2.2	-2.3	2.33	0.1	-0.1
CO_2	90886.74	7.5	-3.2	-13.8	-14.9	1731.30	3.1	-3.1
CH_4	1.58	6.7	-2.8	-12.3	-13.3	1.38	1.0	-1.0

Table 5.3. The description of the VOC species in the CB05 chemical mechanism.

Species Code	**Species description**
ALD2	Acetaldehyde
ALDX	Propionaldehyde and higher aldehydes
CH4	Methane
ETH	Ethylene
ETHA	Ethane
ETOH	Ethanol
FORM	Formaldehyde
IOLE	Internal olefin carbon bond (R-C=C-R)
ISOP	Isoprene
MEOH	Methanol
OLE	Terminal olefin carbon bond (R-C=C)
PAR	Paraffin carbon bond (C-C)
TERP	Terpenes
TOL	Toluene and other monoalkyl aromatics
UNK	Unknown compounds
UNR	Unreactive compounds
XYL	Xylene and other polyalkyl aromatics

5.3.3. Spatial distributions of pollutants concentrations and projected future changes

5.3.3.1. Ozone and its precursors

Table 5.3 lists the description of VOC species in the CB05 chemical mechanism, and Fig. 5.5 depicts the averaged VOCs speciation from the RPD and RPV mobile emissions in Base-year case. The major highly reactive VOCs are ethylene (ETH, 5.1%), toluene (TOL, 2.6%), and xylenes (XYL, 2.9%).

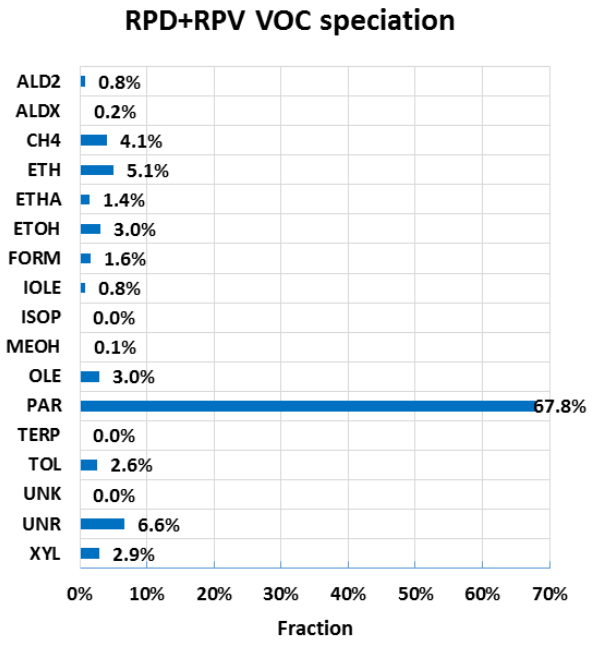

Fig. 5.5. The averaged VOCs speciation (mole fraction) from the RPD+RPV mobile emissions in Base-year Case.

Fig. 5.6 plots the spatial distributions of Base-year surface O_3 and its precursors. The maximum daily average 8-h (MDA8) O_3 hotspots are located northwest of the urban area, under the impact of the Gulf/Bay breezes originating from the southeast. High NO_x and CO concentrations are located over the urban area, home to high motor vehicle emissions. Elevated ethylene concentrations are predicted over the industrial regions, while

toluene and xylenes concentrations are high over both industrial regions and urban road networks. Formaldehyde hotspots coincide with areas with emission sources from non-point oil and gas productions. Isoprene and terpenes concentrations are high over the northern part of the domain, home to significant biogenic emissions due to large forest cover.

Fig. 5.7 exhibits the spatial differences between each future-year scenario and Base-year case. As explained in a previous paragraph, the UC case reported increased emissions while the INT and BC cases predicted moderate and significant emissions reductions, respectively. The trends in NO_x concentrations are similar to those in emissions. The difference in simulated concentrations is mostly localized along the major highways. The magnitudes of change in NO_x concentrations are up to 5 ppb. Interestingly, the change in O_3 concentrations is different between urban and outflow areas. For instance, considering the Base-year and UC cases, O_3 decreases with an increase in NO_x over the NO_x-saturated urban area; while in the NO_x-limited outflow area, O_3 increases with an increase in NO_x. Due to the nonlinearity of O_3 chemistry, the NO_x increase in the UC case causes the urban area to become more NO_x-saturated, resulting in increased titration of O_3. Conversely, in the BC case, the NO_x reductions can bring up O_3 concentrations along major highways in the urban area; while the vast downwind outflow regions are predicted to benefit from the substantial emissions reductions. The distributions of the change in ethylene concentrations in future-year cases are similar to those in NO_x concentrations. The large simulated difference in isoprene concentrations is located in the northern area. The lower isoprene

concentrations in the UC case could be attributed to more indirect reactions with the enhanced NO_x emissions and concentrations (Diao et al., 2016b).

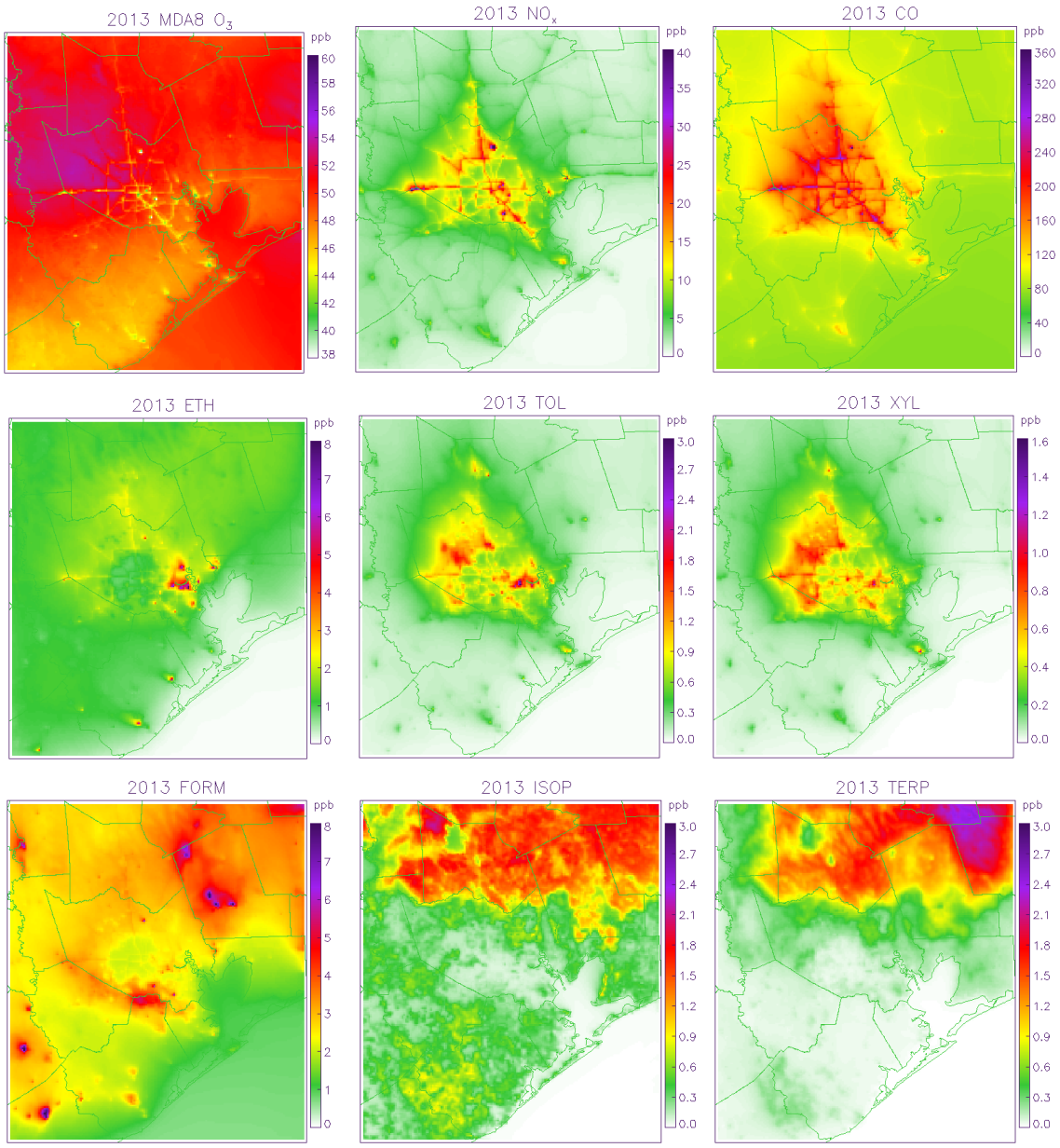

Fig. 5.6. Spatial distributions of Base-year surface concentrations of monthly average MDA8 O_3, NO_x, CO, ethylene, toluene, xylenes, formaldehyde, isoprene, and terpenes during September 2013. The actual maps are in 176 km × 200 km.

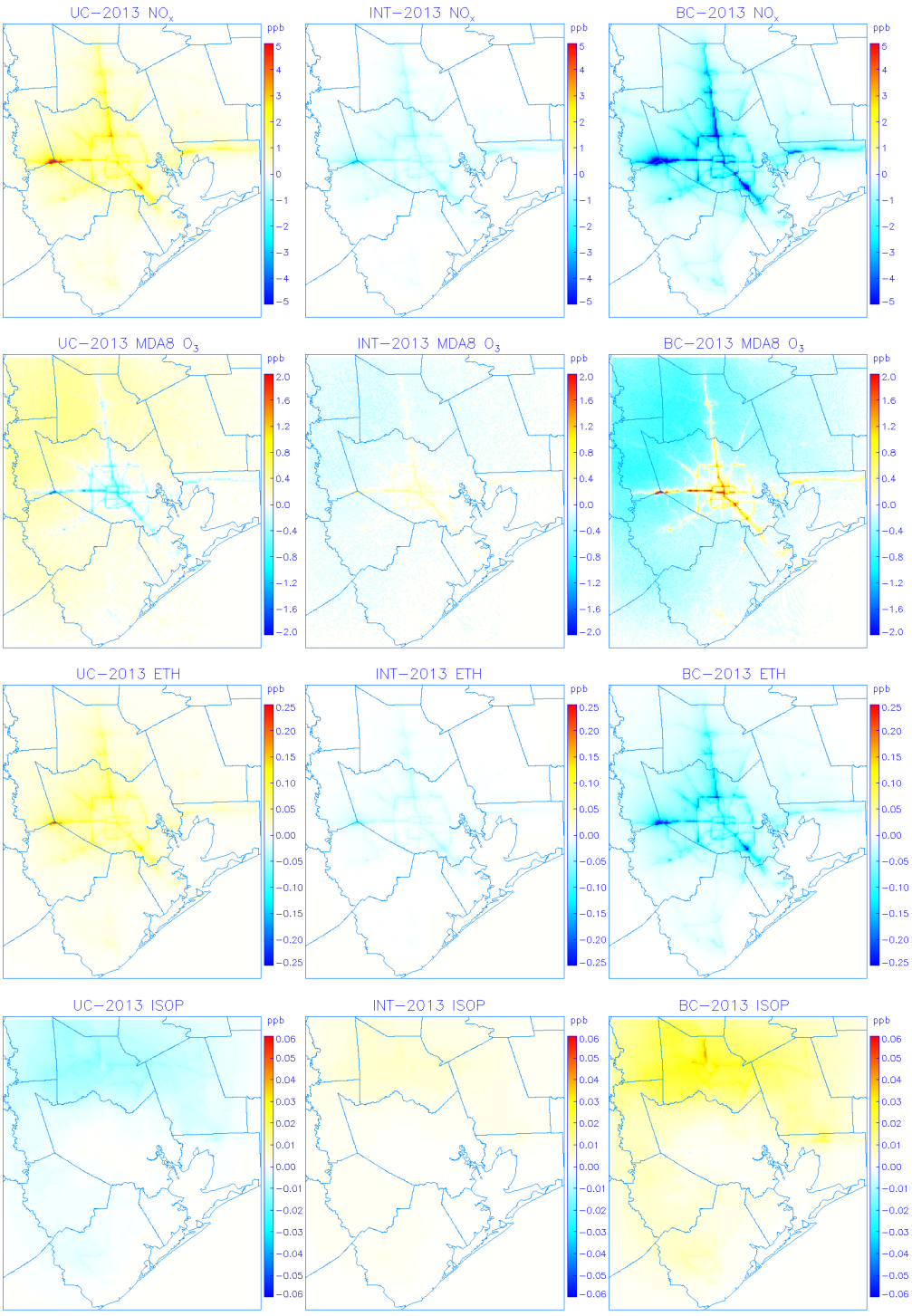

Fig. 5.7. The spatial difference of ground-level MDA8 O_3, and monthly average NO_x, ethylene, and isoprene during September 2013 between different simulations: UC-2013; INT-2013; BC-2013. The actual maps are in 176 km × 200 km.

5.3.3.2. $PM_{2.5}$ and speciated $PM_{2.5}$

Table 5.4 lists the primary $PM_{2.5}$ species as represented in the SMOKE and CMAQ models. Fig. 5.8 displays the domain-wide CMAQ-simulated concentrations of ground-level $PM_{2.5}$ species. The sum of inorganic aerosols (sulfate, nitrate, and ammonium) accounts for 20.8%; with sulfate being predominant one (15.9%). The sum of primary organic carbon (POC), secondary organic carbon (SOC), elemental carbon (EC), and primary non-carbon mass (APNCOM) take up 17.9%. Aerosol water accounts for 29.6%, which is the biggest component as water usually attaches on the surface of particles. Sodium (Na^+), chloride (Cl^-), and trace metals (Fe, Al, Si, Ti, Ca^{2+}, Mg^{2+}, K^+, Mn) are generally relatively small in each and combination of them occupy 10.8%. And remaining un-speciated fine PM is 21%.

Table 5.4. The description of speciated $PM_{2.5}$ in the SMOKE and CMAQ models.

SMOKE species	CMAQ species	Species description
PSO4	ASO4	Sulfate
PNO3	ANO3	Nitrate
PNH4	ANH4	Ammonium
POC	POC	Primary organic carbon
	SOC	Secondary organic carbon
PEC	EC	Elemental carbon
PNCOM	APNCOM	Primary non-carbon organic mass
PH2O	AH2O	Water
PFE	AFEJ	Iron
PAL	AALJ	Aluminum
PSI	ASIJ	Silica
PTI	ATIJ	Titanium
PCA	ACAJ	Calcium
PMG	AMGJ	Magnesium
PK	AKJ	Potassium
PMN	AMNJ	Manganese

PNA	ANAJ	Sodium
PCL	ACLIJ	Chloride
PMOTHR	AOTHRJ	other species

Notation: In 2nd column, the SOC calculation is based on Carlton et al., 2010.

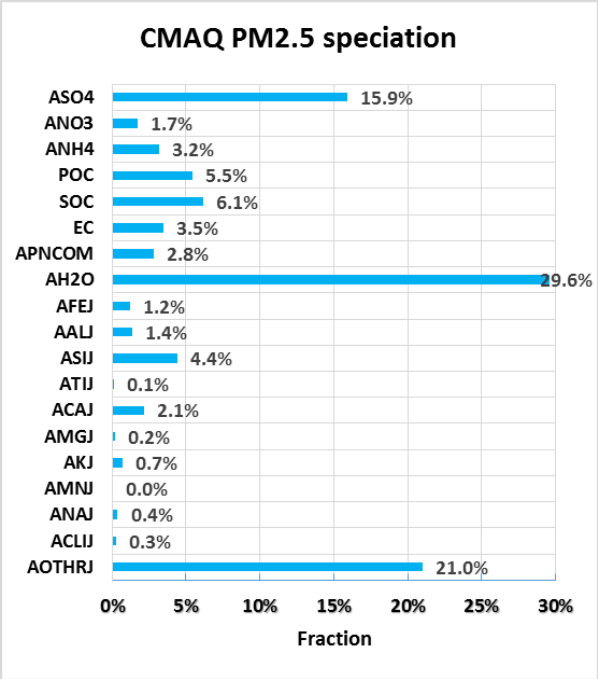

Fig. 5.8. The domain-wide CMAQ simulated $PM_{2.5}$ speciation (mass fraction) in the model surface layer.

Fig. 5.9 shows the spatial distributions of Base-year surface $PM_{2.5}$ and speciated $PM_{2.5}$ concentrations. The total $PM_{2.5}$ concentrations in most regions are below 20 μg m^{-3}, except in several industrial locations. High concentrations of POC, APNCOM, and EC clearly reveal the major highways and industrial point sources. SOC include secondary products from both anthropogenic and biogenic sources. Elevated sulfate and ammonium concentrations are predicted near industrial sources. Shimadera et al. (2014) suggested that nitrate can be affected by NH_3 concentrations and the formation of NH_4NO_3. Water hotspots are matched with high concentrations of ammonium, nitrate and SOC (Hodzic et al., 2014), as they are very soluble in water.

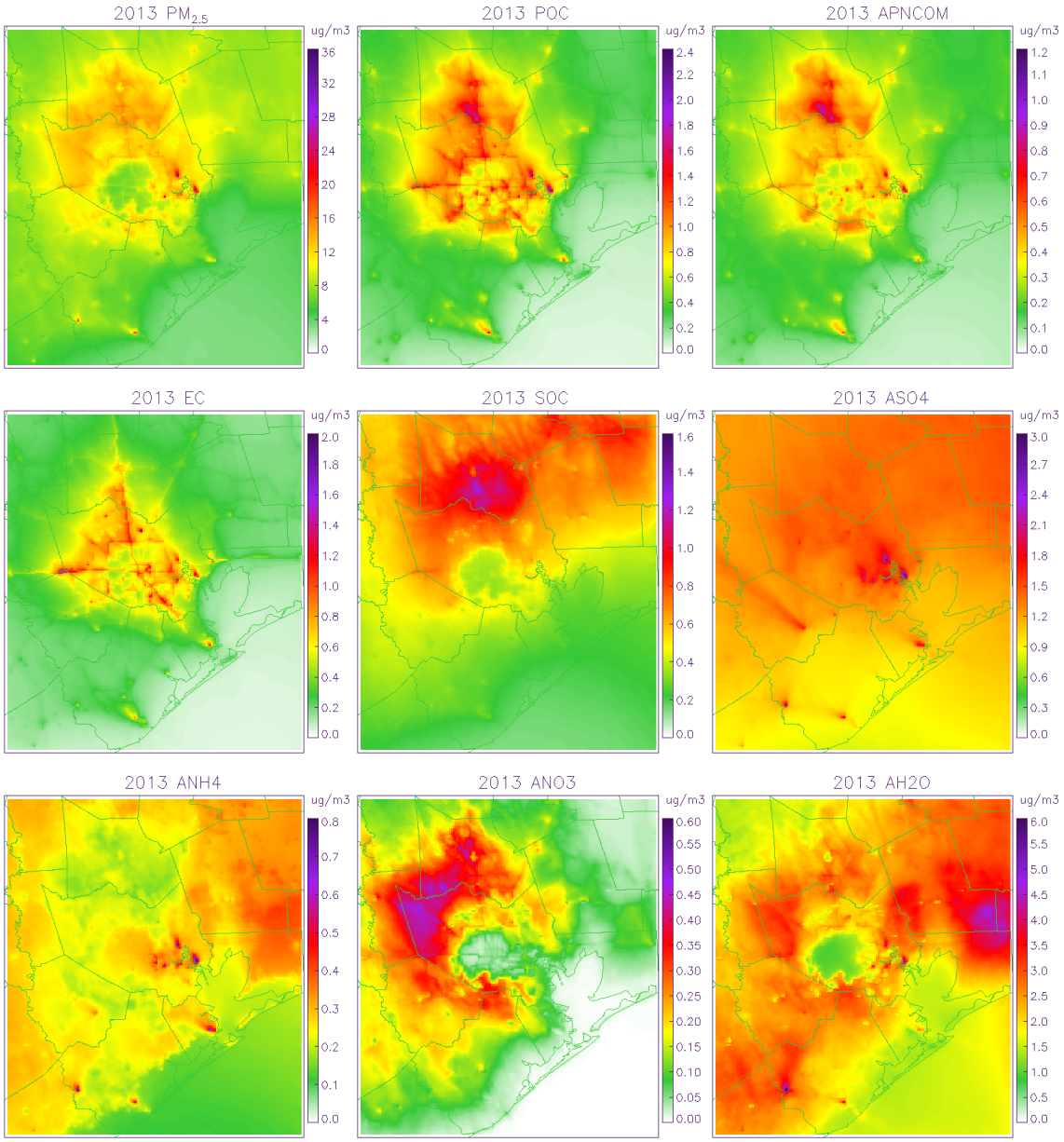

Fig. 5.9. Spatial distributions of Base-year surface concentrations of monthly average $PM_{2.5}$ and speciated $PM_{2.5}$ during September 2013. The actual maps are in 176 km × 200 km.

Since diesel mobile emissions are changed in the future-year cases, it is important to consider what the major species comprise mobile emissions and have higher corresponding changes. Table 5.5 depicts the mass fraction and diesel fraction of each $PM_{2.5}$ component in the RPD mobile emissions. The two biggest components are elemental

carbon (42.3%) and primary organic carbon (29.1%). Species with higher diesel fraction means they will have a relatively large change in the future-year cases. These species are EC (89%), POC (55%), primary non-carbon mass (50%), and sulfate (52%).

Table 5.5. The mass fraction and diesel fraction of each $PM_{2.5}$ component in the RPD mobile emissions.

Species	2013		Differences to 2013
	[g/day]	Mass Fraction	ZDF
PEC	2423279	42.32%	-89%
POC	1665856	29.09%	-55%
PMOTHR	594298	10.38%	-21%
PNCOM	379542	6.63%	-50%
PFE	145279	2.54%	-16%
PSO4	139608	2.44%	-52%
PMG	117028	2.04%	-13%
PSI	108734	1.90%	-23%
PNH4	47499	0.83%	-46%
PCA	45915	0.80%	-49%
PNO3	16179	0.28%	-69%
PCL	12697	0.22%	-64%
PH2O	10260	0.18%	-13%
PAL	8110	0.14%	-47%
PTI	4699	0.08%	-22%
PNA	3363	0.06%	-77%
PK	2318	0.04%	-53%
PMN	1359	0.02%	-14%

Fig. 5.10 plots the spatial differences between future years and base case for $PM_{2.5}$ and major speciated components. The trends in $PM_{2.5}$ concentrations follow the emissions, with an increase in UC case and moderate and large reductions in INT and BC cases, respectively. The magnitudes of changes in total $PM_{2.5}$ concentrations are up to 1 μg m^{-3}. The changes in elemental carbon are up to 0.4 μg m^{-3}. The changes in sulfate are along highway links even as the sulfate hotspots are near industrial sources. The difference in aerosol water concentrations coincided with the high water concentrations.

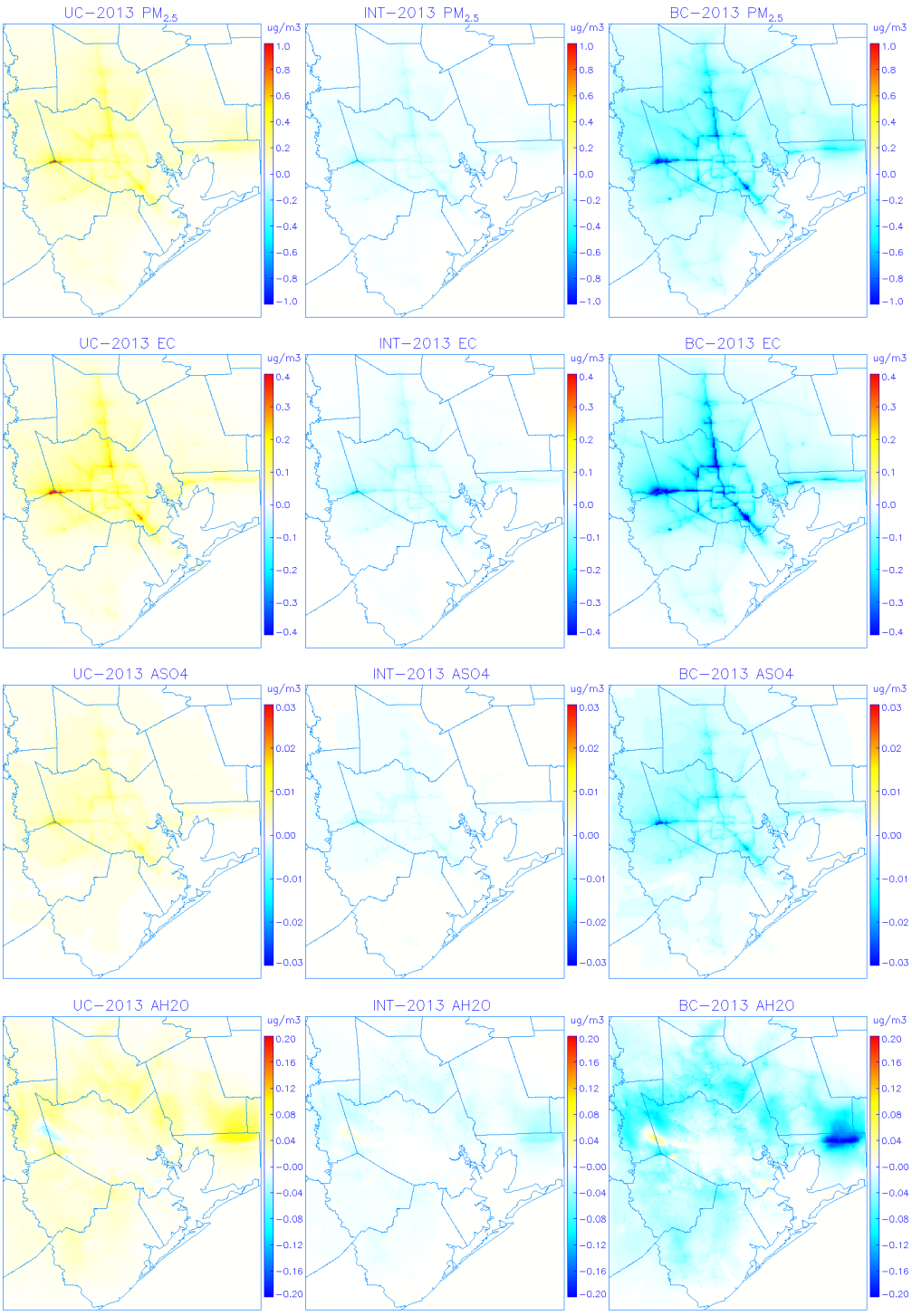

Fig. 5.10. The spatial difference of surface concentrations of monthly average $PM_{2.5}$, EC, ASO4, and AH2O during September 2013 between different simulations: UC-2013; INT-2013; BC-2013. The actual maps are in 176 km × 200 km.

5.4. Summary

In this study, we developed future projections for trucking emissions and evaluated various emissions scenarios related to varying levels of emission control. Each emissions scenario was used in a WRF-SMOKE-CMAQ air quality modeling system utilizing a spatial resolution of 1 km to estimate its impacts on regional O_3 and $PM_{2.5}$.

Current year evaluations showed reasonable modeling performance. If no future emissions control are applied (or if the fleet is not replaced with cleaner technology vehicles), the projected increases are large in UC case for some species in the RPD sector; while a substantial decrease in emissions can be achieved if best control is applied. These species are NO_x (19.9%, -36.9%), PM_{10} (16.8%, -31.1%), $PM_{2.5}$ (31.5%, -58.3%), and hazardous air pollutants such as formaldehyde (25.9%, -47.9%), acetaldehyde (19.8%, -36.7%), acrolein (32.8%, -60.7%), and Naphthalene (24.0%, -44.4%); where the values in parentheses represent percentage changes of each species emissions for the UC and BC cases, respectively.

The changes in concentrations of major O_3 precursors (e.g., NO_x and ethylene) in future-year cases closely followed the emissions. The simulated differences were mostly located along major highways. The MDA8 O_3 has different changing features between urban and outflow regions, with a change of up to ~2 ppb; the vast downwind outflow regions will benefit from the substantial emissions reductions causing reduced O_3. The $PM_{2.5}$ and speciated $PM_{2.5}$ concentrations followed the change of emissions, and showed predicted changes of up to ~1 μg m^{-3}. The results indicate that to maintain the current air

quality conditions, we need to apply highest emission reductions to at least 50% of the freight traffic.

Chapter 6. Conclusion

A WRF-SMOKE-CMAQ air quality modeling system was used to investigate the sensitivity of surface O_3 simulation due to precursor's emissions, meteorology, and grid resolution. The simulation period is September 2013, coincident with the NASA DISCOVER-AQ Texas campaign.

For the first task of this dissertation, a base WRF run (BASE) and a WRF run initialized with NOAA GOES satellite sea surface temperature (SST) (SENS) were performed to clarify the impact of high-resolution SST on simulated surface O_3 over the Greater Houston area during the high O_3 episode on 25th September 2013. The SENS case showed reduced land-sea thermal contrast during early morning hours due to 1-2˚C lower SST over water bodies. The lowered SST reduced the model wind speed and slowed the dilution rate. These changes led to a simulated downwind O_3 change of ~5 ppb near the area over land with peak simulated afternoon O_3. However, the SENS case still under-predicted surface O_3 in urban and industrial areas. Episodic flare emissions, dry sunny postfrontal stagnated conditions, and land-bay/sea breeze transitions could be the potential causes. To investigate the additional sources of error, three sensitivity simulations were performed for the high ozone period. These involved adjusted emissions, adjusted wind fields, and combined adjusted emissions and winds. These scenarios were superimposed on the updated SST (SENS) case. Adjusting NO_x and VOC emissions using simulated/observed ratios improved correlation and index of agreement (IOA) for NO_x from 0.48 and 0.55 to 0.81 and 0.88 respectively, but still reported spatial misalignment of

observed afternoon O_3 hotspots. Adjusting wind fields to represent morning weak westerly winds and afternoon converging zone significantly mitigated under-estimation of the observed O_3 peaks. For example, simulations with adjusted wind fields and adjusted (emissions + wind fields) reduced under-estimation of the peak magnitude of 100 ppb from 50 ppb to 7 and 9 ppb. Additionally, these sensitivity cases captured the timing and location of the observed O_3 hotspots. The simulation case with both adjusted emissions and wind fields reported the best statistics for NO_x (correlation: 0.84; IOA: 0.90) and O_3 (correlation: 0.87; IOA: 0.92). These comparisons suggest that emissions and wind fields are important in determining the magnitude of high peaks, and wind direction is more critical in determining their timing and location. Particularly, improving the model capability to reproduce small-scale meteorological conditions favoring O_3 production, such as stagnation and wind reversal, is crucial for accurate placement of locations of peak O_3 and its precursors.

For the second task, the impact of horizontal spatial resolution on simulated NO_x and O_3 were investigated. We employed an approach recommended by the United States Environmental Protection Agency to allocate county-based emissions to model grid cells in 1 km and 4 km horizontal grid resolutions. The CMAQ Integrated Process Rate analyses showed substantial difference in emissions contributions between 1 and 4 km grids but similar NO_x and O_3 concentrations over urban and industrial locations. For example, the peak NO_x emissions at an industrial and urban site differed by a factor of 20 for the 1 km and 8 for the 4 km grid, but simulated NO_x concentrations changed only by a factor of 1.2 in both cases. Hence, due to the interplay of the atmospheric processes, we cannot expect

a similar level of reduction of the gas-phase air pollutants as the reduction of emissions. Both simulations reproduced the variability of NASA P-3B aircraft measurements of NO_y and O_3 in the lower atmosphere (from 90 m to 4.5 km). Both simulations provided similar reasonable predictions at surface, while 1 km case depicted more detailed features of emissions and concentrations in heavily polluted areas, such as highways, airports, and industrial regions, which are useful in understanding the major causes of O_3 pollution in such regions, and to quantify transport of O_3 to populated communities in urban areas. The Integrated Reaction Rate analyses indicated a distinctive difference of chemistry processes between the model surface layer and upper layers, implying that correcting the meteorological conditions at the surface may not help to enhance the O_3 predictions. The model-observation O_3 bias in our studies (e.g., large over-prediction during the nighttime or along Gulf of Mexico coastline), were due to uncertainties in meteorology, chemistry or other processes. Horizontal grid resolution is unlikely the major contributor to these biases.

As indicated by the 2013 H-GAC Regional Goods Movement Plan, the population of the Houston Area is projected to grow by 50% in 2040, which could potentially result in an increased trucking and other freight activity to meet the needs of the growing population. The third task of this dissertation developed future projections for trucking emissions, and evaluated various emissions scenarios related to varying levels of emission control. These emissions scenarios include: (1) a current-year case; (2) a "business as usual" case, where the trucking fleet in 2040 will have the same emission factors as in 2011; (3) an "intermediate emissions" case, where reasonable fractions for fleet turnover are assumed; (4) a "best control" case, where all trucks in 2040 are fitted with the control

technologies resulting in the highest reduction in emissions; (5) a "zeroing diesel freight" case, where trucks from diesel fuel are turned to zero. Each emissions scenario was used in a fine resolution (1 km) WRF-SMOKE-CMAQ air quality modeling system to estimate its impacts on regional ozone and $PM_{2.5}$. Results indicated that the MDA8 O_3 has different changing features between urban and outflow regions, with a change of up to ~2 ppb; the vast downwind outflow regions will benefit from the substantial emissions reductions. $PM_{2.5}$ and speciated $PM_{2.5}$ concentrations generally followed the change of emissions, with $PM_{2.5}$ concentrations depicting a decrease of up to ~1 μg m^{-3}. The results indicate highest emission reductions are needed to be applied to at least 50% of the freight traffic to maintain the current air quality standards.

References

Abbot, D. S., Palmer, P. I., Martin, R. V., Chance, K. V., Jacob, D. J., Guenther, A., 2003. Seasonal and interannual variability of North American isoprene emissions as determined by formaldehyde column measurements from space, Geophysical Research Letters, 30, 17, 1886.

Adelman, Z., 2015. Emissions modeling platform spatial surrogate documentation, prepared for Rich Mason, U.S. EPA OAQPS, UNC-IE, July 1, 2015.

Arunachalam, S., Holland, A., Do, B., Abraczinskas, M., 2006. A quantitative assessment of the influence of grid resolution on predictions of future-year air quality in North Carolina, USA. Atmos. Environ., 40, 5010-5026.

Banta, R.M., Senff, C.J., Nielsen-Gammon, J., Darby, L.S., Ryerson, T.B., Alvarez, R.J., Sandberg, S.R., Williams, E.J., Trainer, M., 2005. A bad air day in Houston. Bull. Amer. Meteor. Soc. 86, 657-669.

Banta, R. M., Senff, C. J., Alvarez, R. J., Langford, A. O., Parrish, D. D., Trainer, M. K., Darby, L. S., Hardesty, R. M., Lambeth, B., Neuman, J. A., Angevine,W. M., Nielsen-Gammon, J., Sandberg, S. P., and White, A. B., 2011. Dependence of daily peak O_3 concentrations near Houston, Texas on environmental factors: Wind speed, temperature, and boundary-layer depth. Atmos. Environ., 45, 162–173.

Byun, D. and J. K. S. Ching, 1999. Science Algorithms of the EPA Models-3 Community Multiscale Air Quality (CMAQ) Model System, Chapter 16: Process Analysis. EPA/600/R-99/030, March 1999.

Byun, D., Kim, S., Czader, B., Nowak, D., Stetson, S., Estes, M., 2005. Estimation of biogenic emissions with satellite-derived land use and land cover data for air quality modeling of Houston-Galveston ozone nonattainment area. J. Environ. Manage., 75, 285-301.

Byun, D., Kim, S., Cheng, F., Kim, H., & Ngan, F., 2007. Improved Modeling Inputs: Land Use and Sea Surface Temperature. Texas Comm. on Environ. Quality, Final Report, August 31, 2007, available at https://www.tceq.texas.gov/airquality/airmod/project/pj_report_met.html.

Byun, D. W., Kim S.-T., and Kim S.-B., 2007. Evaluation of air quality models for the simulation of a high ozone episode in the Houston metropolitan area, Atmos. Environ., 41, 837–853.

Byun, D. and Schere, K. L., 2006. Review of the Governing Equations, Computational Algorithms, and Other Components of the Models-3 Community Multiscale Air Quality (CMAQ) Modeling System, Appl. Mech. Rev., 59, 51–77.

Carlton, A. G., Bhave, P. V., Napelenok, S. L., Edney, E. O., Sarwar, G., Pinder, R. W., Pouliot, G. A., Houyoux, M., 2010. Model representation of secondary organic aerosol in CMAQv4.7. Environ. Sci. Technol., 44, 8553-8560.

Carter, W. P. L., 1994. Development of ozone reactivity scales for volatile organic compounds. J. Air and Waste Manage. Assoc., 44 (1994), 881–899.

CATF, 2010. The toll from coal: An updated assessment of death and disease from America's dirtiest energy source. http://www.catf.us/resources/publications/view/138

Cheng, F.-Y., and Byun, D. W., 2008. Application of high resolution land use and land cover data for atmospheric modeling in the Houston–Galveston metropolitan area, Part I: Meteorological simulation results. Atmos. Environ., 42, 7795–7811.

Cheng, F.-Y., Kim, S., Byun, D. W., 2008. Application of high resolution land use and land cover data for atmospheric modeling in the Houston–Galveston metropolitan area: Part II Air quality simulation results. Atmos. Environ., 42, 4853–4869.

Choi, Y., 2014. The impact of satellite-adjusted NO_x emissions on simulated NO_x and O_3 discrepancies in the urban and outflow areas of the Pacific and Lower Middle US. Atmos. Chem. Phys., 14, 675–690.

Choi, Y., Jeon, W., Roy, A., Souri, A., Diao, L., Pan, S., Eslami, E., 2016. CMAQ modeling archive for exceptional events analyses. Texas Comm. on Environ. Quality, Final Report, August 2016, https://www.tceq.texas.gov/airquality/airmod/project/pj_report_pm.html.

Choi, Y., Kim, H., Tong, D., and Lee, P., 2012. Summertime weekly cycles of observed and modeled NO_x and O_3 concentrations as a function of satellite-derived ozone production sensitivity and land use types over the Continental United States, Atmos. Chem. Phys., 12, 6291-6307.

Choi, Y., Osterman, G., Eldering, A., Wang, Y., and Edgerton, E., 2010. Understanding the contributions of anthropogenic and biogenic sources to CO enhancements and outflow observed over North America and the western Atlantic Ocean by TES and MOPITT, Atmos. Environ., doi:10.1016/j.atmosenv.2010.01.029.

Cohan, D. S., Hu, Y., Russell, A. G., 2006. Dependence of ozone sensitivity analysis on grid resolution. Atmos. Environ., 40, 126-135.

Couzo E., Jeffries H. E., Vizuete W., 2013. Houston's rapid ozone increases: Preconditions and geographic origins, Environ. Chem., 10, 260-268.

Couzo E., Olatosi A., Jeffries H. E., Vizuete W., 2012. Assessment of a Regulatory Model Performance Relative to Large Spatial Inhomogeneity in Observed Ozone in Houston, TX, J. Air and Waste Manag. Assoc., 62, 696-706.

Crawford, J. H., Dickerson, R. R., Hains, J. C., 2014. DISCOVER-AQ: Observations and early results, Environ. Manage., September 2014, 8-15.

Czader, B. H., Byun, D. W., Kim, S.-T., and Carter, W. P. L., 2008. A study of VOC reactivity in the Houston-Galveston air mixture utilizing an extended version of SAPRC-99 chemical mechanism, Atmos. Environ., 42, 5733–5742.

Czader, B. H., Choi, Y., Li, X., Alvera, S., and Lefer, B., 2015. Impact of updated traffic emissions on HONO mixing ratios simulated for urban site in Houston, Texas, Atmos. Chem. Phys., 15, 1253–1263.

Czader, B. H., Li, X., Rappenglück, B., 2013. CMAQ modeling and analysis of radicals, radical precursors, and chemical transformations. J. Geophys. Res. Atmos., 118, 11376-11387. doi:10.1002/jgrd.50807.

Czader, B. H. and Rappenglück, B., 2015. Modeling of 1, 3- butadiene in urban and industrial areas, Atmos. Environ., 102, 30-42.

Czader, B. H., Rappenglück, B., Percell, P., Byun, D., Ngan, F., and Kim, S., 2012. Modeling nitrous acid and its impact on ozone and hydroxyl radical during the Texas Air Quality Study 2006, Atmos. Chem. Phys., 12, 6,939–6,951.

Darby, L. S., 2005. Cluster analysis of surface winds in Houston, Texas, and the impact of wind patterns on ozone, J. Appl. Meteor., 44, 1788– 1806.

Daum, P.H., Kleinman, L.I., Springston, S.R., Nunnermacker, L.J., Lee, Y.-N., Weinstein-Lloyd, J., Zheng, J., Berkowitz, C.M., 2003. A comparative study of O_3 formation in the Houston urban and industrial plumes during the 2000 Texas Air Quality Study. J. Geophys. Res., 108, D23, 4715.

Diao, L., Roy, A., Czader, B., Pan, S., Jeon, W., Souri, A., Choi, Y., 2016a. Modeling the effect of relative humidity on nitrous acid formation in the Houston area, Atmos. Environ., 131, 78-82.

Diao, L., Choi, Y., Czader, B., Li, X., Pan, S., Roy, A., Souri, A., Estes, M., Jeon, W., 2016b. Discrepancies between modeled and observed nocturnal isoprene in a urban environment and the possible causes: A case study in Houston, Atmos. Res., 181, 257-264.

Fountoukis, C., Koraj, Dh., Denier van der Gon, H.A.C., Charalampidis, P.E., Pilinis, C., Pandis, S.N., 2013. Impact of grid resolution on the predicted fine PM by a regional 3-D chemical transport model. Atmos. Environ., 68, 24-32.

Haman, C. L., Couzo, E., Flynn, J. H., Vizuete, W., Heffron, B., Lefer, B. L., 2014. Relationship between boundary layer heights and growth rates with ground-level ozone in Houston, Texas, J. Geophys. Res.-Atmos., 119, 6230–6245.

Hodzic, A., Aumont, B., Knote, C., Lee-Taylor, J., Madronich, S., Tyndall, G., 2014. Volatility dependence of Henry's law constants of condensable organics: Application to estimate depositional loss of secondary organic aerosols. Geophysical Research Letters, 4795-4804.

Houyoux, M., Vukovich, J., Brandmeyer, J., 2000. Sparse Matrix Kernel Emissions Modeling System: SMOKE User Manual. MCNC-North Carolina Supercomputing Center. http://www.cmascenter.org/.

Jang, J. C., Jeffries, H. E., Byun, D., Pleim, J. E., 1995a. Sensitivity of ozone to model grid resolution-I. Application of high-resolution regional acid deposition model. Atmos. Environ., 29 (21), 3085-3100.

Jang, J. C., Jeffries, H. E., Tonnesen, S., 1995b. Sensitivity of ozone to model grid resolution-II. Detailed process analysis for ozone chemistry. Atmos. Environ., 29 (21), 3101-3114.

Jeffries H. E. and Tonnesen S., 1994. A comparison of two photochemical reaction mechanisms using mass balance and process analysis. Atmos. Environ., 28(18), 2991-3003.

Jeon,W.-B., Lee, S.-H., Lee, H.-W., Kim, H.-G., 2012. Process analysis of the impact of atmospheric recirculation on consecutive high-O_3 episodes over the Seoul Metropolitan Area in the Korean Peninsula. Atmos. Environ., 63, 213-222.

Jeon,W.-B., Lee, S.-H., Lee, H., Park, C., Kim, D.-H, Park, S-Y, 2014. A study on high ozone formation mechanism associated with change of NO_x/VOCs ratio at a rural area in the Korean Peninsula. Atmos. Environ., 89, 10-21.

Jeon, W.-B., Choi, Y., Lee, H. W., Lee, S.-H., Yoo, J.-W., Park, J., Lee, H.-J., 2015. A quantitative analysis of grid nudging effect on each process of $PM_{2.5}$ production in the Korean Peninsula. Atmos. Environ., 122, 763-774.

Kim, H., Ngan, F., Lee, P., Tong, D., 2013. Development of IDL-based geospatial data processing framework for meteorology and air quality modeling. Retrieved from http://aqrp.ceer.utexas.edu/projectinfoFY12_13%5C12-TN2%5C12-TN2Final Report.pdf.

Langford, A. O., S. C. Tucker, C. J. Senff, R. M. Banta, W. A. Brewer, R. J. Alvarez II, R. M. Hardesty, B. M. Lerner, and E. J. Williams, 2010, Convective venting and surface ozone in Houston during TexAQS 2006. J. Geophys. Res., 115, D16305.

Li, G., Zhang, R., Fan, J., and Tie, X., 2007. Impacts of biogenic emissions on photochemical ozone production in Houston, Texas. J. Geophys. Res., 112, D10309.

Li, N., Chen, J.-P., Tsai, I-C., He, Q., Chi, S.-Y., Lin, Y.-C., Fu, T.-M., 2016. Potential impacts of electric vehicles on air quality in Taiwan. Sci. of the Total Environ., 566-567, 919-928.

Li, L., Chen, C. H., Huang, C., Huang, H. Y., Zhang, G. F., Wang J., Wang H. L., Lou, S. R., Qiao, L. P., Zhou, M., Chen, M. H., Chen, Y. R., Streets, D. G., Fu J. S., Jang C. J., 2012. Process analysis of regional ozone formation over the Yangtze River Delta, China using the Community Multi-scale Air Quality modeling system. Atmos. Chem. Phys., 12, 10971-10987.

Li, X., Choi, Y., Czader, B., Roy, A., Kim, H., Lefer, B., Pan, S., 2016. The impact of observation nudging on simulated meteorology and ozone concentrations during DISCOVER-AQ 2013 Texas campaign. Atmos. Chem. Phys., 16, 3127-3144.

Loughner, C. P., Follette-Cook, M. B., Fried, A., Pickering, K., Gilliam, R., Mackay, J., 2015. The role of bay breezes on a high surface ozone episode during the Houston, Texas DISCOVER-AQ field campaign, 7th International Workshop on Air Quality Forecasting Research, September 3, 2015, available at http://www.arl.noaa.gov/IWAQFR_Presentations_2015.php.

Mesinger F. et al, NORTH AMERICAN REGIONAL REANALYSIS: A long-term, consistent, high-resolution climate dataset for the North American domain, as a major improvement upon the earlier global reanalysis datasets in both resolution and accuracy, submitted to BAMS 2004. Available at: http://www.esrl.noaa.gov/psd/.

Murphy C. F., and Allen D. T., 2005. Hydrocarbon emissions from industrial release events in the Houston-Galveston area and their impact on ozone formation. Atmos. Environ. 39, 3785-3798.

Nam, J., Kimura, Y., Vizuete,W., Murphy, C., Allen, D.T., 2006. Modeling the impact of emission events on ozone formation in Houston, Texas. Atmos. Environ. 40, 5329-5341.

NASA, 2013. http://www-air.larc.nasa.gov/missions/discover-aq/discover-aq.html.

Ngan, F., and Byun, D. W., 2011. Classification of weather patterns and associated trajectory analysis of high ozone episodes in Houston during the 2005/2006 TexAQS-II. J. Appl. Meteorol. Climatol., 50, 485–499.

Ngan, F., Byun, D., Kim, H., Lee, D., Rappenglück, B., Pour-Biazar, A., 2012. Performance assessment of retrospective meteorological inputs for use in air quality modeling during TexAQS 2006. Atmos. Environ., 54, 86–96.

Ngan, F., Kim, H., Lee, P., Al-Wali, K., Dornblaser, B., 2013. A study of nocturnal surface wind speed overprediction by the WRF-ARW model in Southeastern Texas. J. Appl. Meteorol. Climatol., 52, 2638-2653.

Nopmongcol, U., Grant, J., Knipping, E., Alexander, M., Schurhoff, R., Young, D., Jung, J., Shah, T., Yarwood, G., 2017. Air quality impacts of electrifying vehicles and equipment across the United States. Environ. Sci. Technol., 51, 2830-2837.

Nopmongcol, U., Liu, Z., Johnson, J., Rassmusen, D., Wentland, A., Yarwood, G., 2015. Three-dimensional performance comparison of CAMx and CMAQ using the 2013 DISCOVER-AQ field study data base. Texas Comm. on Environ. Quality, FY15-52, Final Report, August 2015, available at https://www.tceq.texas.gov/airquality/airmod/project/pj_report_pm.html.

Olaguer, E. P., Rappenglueck B., Lefer B., Stutz J., Dibb J., Griffin R., Brune B., Shauck M., Buhrg M., Jeffries H., Vizuete W., Pinto J., 2009. Deciphering the role of radical

sources during the second Texas air quality study. J. Air and Waste Manage. Assoc., 59, 1258–1277.

Pan, S., Choi, Y., Roy, A., Li, X., Jeon, W., Souri, A. H., 2015. Modeling the uncertainty of several VOC and its impact on simulated VOC and ozone in Houston, Texas. Atmos. Environ. 120, 404-416.

Pan, S., Choi, Y., Jeon, W., Roy, A., Westenbarger, D. A., Kim, H. C., 2017a. Impact of high-resolution sea surface temperature, emission spikes and wind on simulated surface ozone in Houston, Texas during a high ozone episode. Atmos. Environ., 152, 362-376.

Pan, S., Choi, Y., Roy, A., Jeon, W., 2017b. Allocating emissions to 4 km and 1 km horizontal spatial resolutions and its impact on simulated NO_x and O_3 in Houston, TX. Atmos. Environ., 164, 398-415.

Parrish, D.D., Allen, D.T., Bates, T.S., Estes, M., Fehsenfeld, F.C., Feingold, G., Ferrare, R., Hardesty, R.M., Meagher, J.F., Nielsen-Gammon, J.W., Pierce, R.B., Ryerson, T.B., Seinfeld, J.H., Williams, E.J., 2009. Overview of the second Texas air quality study (TexAQS-II) and the Gulf of Mexico atmospheric composition and climate study (GoMACCS). J. Geophys. Res. 114, D00F13.

Pouliot, G. and Pierce, T., 2009. Integration of the Model of Emissions of Gases and Aerosols from Nature (MEGAN) into the CMAQ Modeling System, Available at: https://www.epa.gov/air-emissions-modeling/biogenic-emission-inventory-system-beis

Pour-Biazar, A., McNider, R. T., Roselle, S. J., Suggs, R., Jedlovec, G., Byun, D. W., Kim S., Lin, C. J., Ho, T. C., Haines, S., Dornblaser, B., Cameron, R., 2007. Correcting photolysis rates on the basis of satellite observed clouds. J. Geophys. Res, 112, D10302.

Rappenglück, B., Perna, R., Zhong, S., and Morris G. A., 2008. An analysis of the vertical structure of the atmosphere and upper-level meteorology and their impact on surface ozone levels in Houston, Texas. J. Geophys. Res., 113, D17315.

Roy, A. A., Wagstrom, K. M., Adams, P. J., Pandis, S. N., Robinson, A. L., 2011. Quantification of the effects of molecular marker oxidation on source apportionment estimates for motor vehicles. Atmospheric Environment, 45, 3132-3140.

Roy, A. A., Adams, P. J., Robinson, A. L., 2014. Air pollutant emissions from the development, production, and processing of Marcellus Shale nature gas. J. of the Air and Waste Manage. Assoc., 64:1, 19-37.

Ryerson, T. B., Trainer, M., Angevine, W.M., Brock, C.A., Dissly, R.W., Fehsenfeld, F.C., Frost, G.J., Goldan, P.D., Holloway, J.S., Hubler, G., Jakoubek, R.O., Kuster, W.C., Neuman, J.A., Nicks Jr, D.K., Parrish, D.D., Roberts, J.M., Sueper, D.T., Atlas, E.L., Donnelly, S.G., Flocke, F., Fried, A., Potter, W.T., Schauffler, S., Stroud, V., Weinheimer, A.J., Wert, B.P., Wiedinmyer, C., Alvarez, R.J., Banta, R.M., Darby, L.S., Senff, C.J., 2003. Effect of petrochemical industrial emissions of reactive alkenes and NO_x on tropospheric ozone formation in Houston, Texas. J. Geophys. Res., 108(D8), 4249.

Shimadera, H., Hayami, H., Chatani, S., Morino, Y., Mori, Y., Morikawa, T., Yamaji, K., Ohara, T., 2014. Sensitivity analyses of factors influencing CMAQ performance for fine particulate nitrate. J. Air and Waste Manage. Assoc., 64:4, 374-387.

Skamarock, W. C., and Klemp, J. B., 2008. A time-split non-hydrostatic atmospheric model for weather research and forecasting applications, J. Comput. Phys., 227, 3465-3485.

Souri, A., Choi, Y., Jeon, W., Li, X., Pan, S., Diao, L., Westenbarger, D., 2016. Constraining NO_x Emissions using Satellite NO_2 Measurements during 2013 DISCOVER-AQ Texas Campaign. Atmos. Environ., 131, 371-381.

Tan, J., Zhang, Y., Ma, W., Yu, Q., Wang, J., Chen, L., 2015. Impact of spatial resolution on air quality simulation: A case study in a highly industrialized area in Shanghai, China. Atmospheric Pollution Research, 6, 322-333.

U.S. Census Bureau, 2012. Annual Estimates of the Population of Metropolitan and Micropolitan Statistical Areas: April 1, 2010 to July 1, 2011 (CBSA-EST2011-01), edit by U. S. Census Bureau.

U.S. EPA, 2015a. Technical support document: preparation of emissions inventories for the version 6.2, 2011 emissions modeling platform, August, 2015.

U.S. EPA, 2015b. 2011 National Emissions Inventory, version 2, technical support document, August, 2015. p. 306-307.

U.S. EPA Green Book, 2016. 8-Hr Ozone (2008) Nonattainment State/Area/County Report, as of June 6, 2016. http://www.epa.gov/airquality/greenbook/hncs.html#TEXAS.

Valari, M., Menut, L., 2008. Does an increase in air quality models' resolution bring surface ozone concentrations closer to reality? J. Atmos. Ocean. Tech., 25, 1955-1968.

Vizuete, W., Kim, B.-U., Jeffries, H., Kimura, Y., Allen, D. T., Kioumourzoglou, M.-A., Biton, L., Henderson, B., 2008. Modeling ozone formation from industrial emission events in Houston, Texas. Atmos. Environ. 42, 7641-7650.

Vizuete W., Jeffries H., Tesche T. W., Olaguer., E. P., Couzo E., 2011. Issues with Ozone Attainment Methodology for Houston, TX. J. Air and Waste Manage. Assoc., 61, 3, 238-253.

Webster, M., Nam, J., Kimura, Y., Jeffries, H., Vizuete, W., Allen, D.T., 2007. The effect of variability in industrial emissions on ozone formation in Houston, Texas. Atmos. Environ. 41, 9580-9593.

Willmott, C. J., 1981. On the validation of models. Phys. Geogr., 2, 184–194.

Yarwood, G., Rao, S., Yocke, M., Whitten, G.Z., 2005. Updates to the Carbon Bond chemical mechanism: CB05. Final Report to the US EPA, RT-0400675, December 8, 2005. http://www.camx.com/publ/pdfs/CB05_Final_Report_120805.pdf.